Design of Amphiphilic Anti-Caking Systems for Solid Particles

Dissertation

Zur Erlangung des akademischen Grades

Doktor-Ingenieur (Dr. -Ing.)

vorgelegt dem

Zentrum für Ingenieurwissenschaften

der Martin-Luther-Universität Halle-Wittenberg

als organisatorische Grundeinheit für Forschung und Lehre im Range einer

Fakultät

(§75 Abs. 1 HAG LSA, §19 Abs. 1 Grundordnung)

von Herrn M. Sc. Hangsheng Li

geb. am 18.10.1981 in Shanghai (China)

Gutachter:

1. Prof. Dr. Jörg Kressler
2. Prof. Dr. Roland Weidisch

Halle (Saale), den 2-9-2009

Dedicated to My Wife

Acknowledgement

First of all, I am deeply indebted to my supervisor Prof. Dr. Jörg Kressler for offering me the opportunity to do research in his group, giving me valuable discussions, correcting carefully my manuscripts for publications and encouraging me to go ahead within my thesis.

I want to thank the company – SKW Piesteritz and the Aninstitut – Agrochemisches Institut Piesteritz e.V. for providing the financial support of this work. I want to thank Prof. Dr. Niclas, Dr. Radics and Dr. Reinhardt for their valuable suggestions and discussion.

I want to thank Dr. Karsten Busse for his valuable discussion for evaluation of experimental data and correction of my manuscript. I want to thank Dr. Zofia Funke for experimental support. I want to thank Dr. Henning Kausche, Samuel Kyeremateng and Dirk Pfefferkorn for helping me to do experiments. Finally, I want to thank Sascha Reuter for his help of correcting my German speaking and writing, discussions of experimental data and staying in the same office during the period of my Ph.D. work.

Publications

Hangsheng Li, Robert Sachsenhofer, Wolfgang H. Binder, Thomas Henze, Thomas Thurn-Albrecht, Karsten Busse and Jörg Kressler, **Hierarchical Organization of Poly(ethylene oxide)-*block*-poly(isobutylene) and Hydrophobically Modified Fe$_2$O$_3$ Nanoparticles at the Air/Water Interface and on Solid Supports**, *Langmuir*, **2009**, *25*, 8320-8329.

Hangsheng Li, Dirk Pfefferkorn, Wolfgang H. Binder and Jörg Kressler, **Phospholipid Langmuir Film as Template for *in situ* Silica Nanoparticle Formation at the Air/Water Interface**, *Langmuir*, **2009**, *25*, 13328-13331.

Luke Theogarajan, Hangsheng Li, Karsten Busse, Salil Desai, Jörg Kressler and Carmen Scholz, **Self Assembly of ABA Triblock Copolymers Based on Functionalized Poly(dimethylsiloxane) and Poly(methyl oxazoline)**, *Polym. Int.*, accepted.

Hangsheng Li, Dirk Pfefferkorn, Andreas Kerth, Alfred Blume, Wolfgang H. Binder and Jörg Kressler, **Silica Nanoparticle Formation on Langmuir films of Amphiphiles,** *Polym. Prepr.***,** accepted.

Contents

Abbreviations and Symbols

PVA	Poly(vinyl alcohol)
PVP	Poly(vinyl pyrrolidone)
P1	PVA1
P2	PVA2
P3	PVA3
P98	Technical PVA1
P01	Technical PVA2
P03	Technical PVA3
P80	Technical PVA4
P81	Technical PVA5
P115	Technical PVA6
P116	Technical PVA7
P37	Technical PVA8
PA98	Technical PVA98
PA99	Technical PVA99
F8	Technical surfactant1
F9	Technical surfactant2
B3	Brij 35
T2	Tween 20
T4	Tween 40
T6	Tween 60
T8	Tween 80
PE6	Pluronic PE 6100
PE8	Pluronic PE 8100
NI	Nitrification inhibitor
PS	PVA-Surfactant
PSN	PVA-Surfactant-Nitrification inhibitor
VSN	PVP-Surfactant-Nitrification inhibitor
PVSN	PVA-PVP-Surfactant-Nitrification inhibitor
CAC	Critical aggregation concentration
CMC	Critical micelle concentration
CRH	Critical relative humidity
DPS	Double particle system

MPS	Multi-particle system
ESEM	Environmental scanning electron microscopy
HD	Hydrolysis degree
T	Temperature
R	Gas constant
S_y	Solubility
$P_{(s)}H_2O$	Vapor pressure of a saturated urea solution
P_w^s	Saturation partial pressure
F_c	Capillary adhesive force
γ	Surface tension
L	Wetted length
F	Force
θ	Contact angle
r	Radius of meniscus
h_t	Thickness of coating
k_p	Proportionality constant
U	Withdrawal speed
ρ	Density
ρ_0	Reference density
η	Viscosity
g	Gravity constant
ΔG_m^{θ}	Standard free energy
ΔH	Enthalpy of fusion
$\Delta H_{100\%}$	Enthalpy of fusion of perfect PVA
ppm	Parts per million
M_d	Torque value
s	Rotor speed
R_{a0}	Radius of outer cylinder
R_i	Radius of cone
L_r	Rotor length
τ	Period of oscillation
τ_0	Reference period of oscillation
k_s	Spring constant
M_v	Vibrating mass
σ	Tensile force

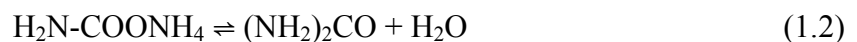|	
ε	Porosity
x_d	Particle diameter
F_H	Adhesive force
R_{ac}	Anti-caking rate
a	Weight of still caked granules
b	Weight of whole caked granules
π	Surface pressure
mmA	Mean molecular area
AFM	Atomic force microscopy
PEO	Poly(ethylene oxide)
PIB	Poly(isobutylene)
Fe_2O_3	Iron oxide
NP	Nanoparticles
LB	Langmuir-Blodgett
LBL	Layer-by-layer
PS	Polystyrene
CdS	Cadmium sulphide nanoparticles
FeNPEB	Iron oxide nanoparticles with PEO_{97}-*b*-PIB_{37}
GPC	Gel permeation chromatography
NMR	Nuclear magnetic resonance
DP	Degree of polymerization
PD	Polydispersity
IRRAS	Infrared reflection adsorption spectroscopy
T_g	Glass transition temperature
T_m	Melting temperature
TEOS	Tertraethyl orthosilicate
DPPC	1,2-dipalmitoyl-*sn*-glycero-3-phosphocholine
TMOS	Tertramethyl orthosilicate

Chapter 1

Introduction

1.1   Nitrogen fertilizer

Fertilizers are chemical compounds extensively applied for supplying various nutrients to plants and improving the chemical and physical properties of soil, thereby directly or indirectly enhancing plant growth, yield, and quality. They are usually applied either through the soil for the uptake by plant roots, or through leaves for the uptake by foliar feeding.[1] Fertilizers provide typically three major plant nutrients, including nitrogen, phosphorus, potassium and the secondary plant nutrients, calcium, sulphur and magnesium and sometimes trace elements with a role in plant nutrients, boron, chlorine, manganese, iron, zinc, copper and molybdenum.[1] Urea, the highest nitrogen content from all solid nitrogenous fertilizers in common use (46.7%), is one of the most widely applied products. It is industrially produced by the reaction of ammonia and carbon dioxide. The reaction is an equilibrium reaction, with incomplete conversion of the reactants. Two principal reactions take place during the formation of urea from ammonia and carbon dioxide.[2] The first reaction is exothermic:

$$2NH_3 + CO_2 \rightleftharpoons H_2N\text{-}COONH_4 \tag{1.1}$$

Whereas the second reaction is endothermic:

$$H_2N\text{-}COONH_4 \rightleftharpoons (NH_2)_2CO + H_2O \tag{1.2}$$

Solid urea is marketed as prills or granules. The advantages compared to powder are their impact strength, crushing strength and free-flow behavior, in particular, in product handling, storage and transportation. Urea is a hygroscopic material which absorbs water vapor from the environment. The solubility of urea in water is markedly affected by the storage temperature which can be estimated from Equation 1.3[3]

$$S_y = 636 + 26T - 0.27T^2 + 0.00604T^3 \tag{1.3}$$

where S_y is the solubility of urea and T is the temperature.

The solubility of urea in water at different temperatures is shown in Table 1.1.[3]

Table 1.1: Solubility of urea in water at different temperatures.

Temperature [°C]	Solubility (Urea [g] / Water [g])
20	1.08
30	1.34
40	1.56
50	2.05
60	2.54

As fertilizer, urea is usually spread at rates between 40 and 300 kg/ha, but actual spreading rates will vary according to farm types and regions.[1] During the summer, urea should be spread just before, or during the rain season to reduce possible losses from volatilization (processes wherein nitrogen is lost to the atmosphere as ammonia gas).[1] Because of the high nitrogen concentration in urea, it is very important to achieve a homogenous and continuous spread. The application equipment must be correctly calibrated and properly used.[1]
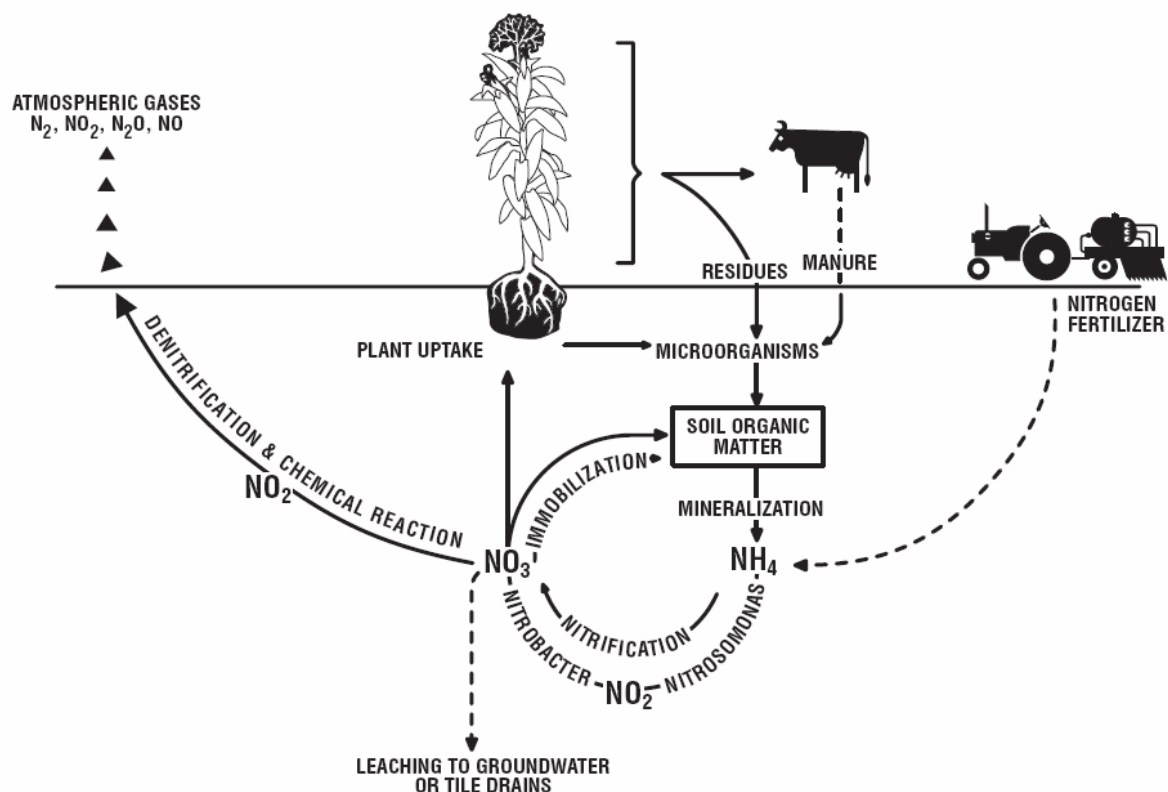

Figure 1.1: The nitrogen cycle in soils.[4]

During application of nitrogen fertilizer, ammonium ions (NH_4^+) in the soils, whether from decomposition of organic material or from the application of ammonia-containing mineral

fertilizers, are oxidized to nitrite (NO_2^-) by nitrosomonas bacteria and nitrate (NO_3^-) by nitrobacter bacteria in the process termed nitrification (Figure 1.1).[4] In fact, both nitrate and ammonium are normally the forms of nitrogen nutritious substances taken up by plants.[5,6] But nitrate is readily soluble in water and in the aqueous soil medium. Therefore, it is completely mobile in the soil, in contrast to ammonia, which is strongly adsorbed in soil colloids and base-exchange complexes. It was reported that nitrification rates are greatly reduced by cool soil temperature and low pH value.[7,8] Under unfavorable conditions, nitrate can be reduced to N_2 by denitrification, which can result in further considerable losses of fertilizer activity.[9] Therefore, nitrification inhibitors are extensively used to reduce significantly leaching losses of nitrate by stabilization of ammonia leading to a reduction of emissions of the environmentally relevant gases N_2O and NO.[10,11,12] Nitrification inhibitors are compounds that delay bacterial oxidation of the ammonium ion by depressing the activity of nitrosomonas bacteria in the soil over a certain period of time. Thus, they control leaching of nitrate by keeping nitrogen in the ammonium form longer, and preventing denitrification of nitrate.[13] Possible disadvantages include that fertilizers containing ammonia and a nitrification inhibitor may result in increased ammonia volatilization if they are not incorporated into the soil immediately after application. Depending on the type of nitrification inhibitor, the activity of soil bacteria may not only be interrupted for a certain time period, but the soil bacteria may actually be killed. This can be regarded an undesirable interference in a natural soil process.[9,14] Frequently used nitrification inhibitors are dicyandiamide and 1,2,4-triazole.[1] Triazole is very good soluble in aqueous systems. However, it sublimates even at room temperature, the enthalpy of triazole sublimation is approximately 80.5 ± 0.7 kJ/mol.[15]

1.2   Caking and anti-caking of fertilizer granules

One of the most troublesome properties of fertilizers (crystalline materials) is their tendency to bind together or to cake during storage. Caking of fertilizers is caused by the formation of contact points between granules. These contact points are divided into two types, adhesive contacts and phase contacts which include solid contacts and liquid contacts.[16]
Phase contacts, also termed salt bridges, are crystal bridges formed at the contact points between granules. This is the most troublesome problem of caking. Fertilizers, as hygroscopic substances, absorb water from the atmosphere when the partial pressure of water vapor in the atmosphere is greater than the vapor pressure exerted by a saturated aqueous solution of the pure substance at that temperature.[16] Theses kinds of solutions formed between the surfaces of fertilizer granules are termed liquid bridges or liquid contacts. If, later, the atmospheric

moisture content decreases resulting in a partial pressure below the vapor pressure of the saturated solution, the crystals dry out (re-crystallization behavior) and bind together. This re-crystallization process results not only in crystal bridges between fertilizer granules but also pores (hollow structures) are formed in the bridges.[17] Pores in the bridges enhance the caking problems due to small fluctuations in the atmospheric temperature and humidity which occur several times during one day. When the humidity increases, the re-dissolved solutions diffuse easily into the hollow structures. The following solidification of the liquid in the hollow structures makes the crystal bridges stronger and harder, the so-called hardening.[17]

Adhesive contact, also termed capillary adhesion, results from molecular attraction between the surfaces of granules. The forces of attraction, known as van der Waals forces, are considered to be relatively weak. This caking mainly takes place when fertilizer granules are exerted to pressure of other granules during storage in the bags or piles.[16] It is believed that during the storage the combination of both adhesive contacts and phase contacts happens simultaneously attributing to the caking of fertilizer.

Caking of fertilizers can be influenced by a number of factors, which are divided into internal factors, related to the physical-chemical constitution of the fertilizer, and external factors, related to the environmental conditions under which fertilizers are exposed and stored.[18] Among the internal factors, the initial moisture content of the fertilizers is the most important one. Generally, the initial water content decreases with increasing manufacture temperature. The hygroscopic properties of the fertilizer product can also influence the caking. Critical relative humidity (CRH) is used to characterize the hygroscopic substances. From the definition, above the point of CRH, the water absorption of substances from the surrounding air increases markedly. For example, the CRH of urea can be calculated by Equation 1.4[3,17]

$$CRH = \frac{P_{(s)}H_2O}{P_w^s} \tag{1.4}$$

where $P_{(s)}H_2O$ is the vapor pressure of a saturated urea solution and P_w^s is the saturation partial pressure.

The vapor pressure of a saturated urea solution can be calculated by Equation 1.5[3,17]

$$\ln P_{(s)}H_2O = 175.766 - 11552/T - 22.679\ln T \tag{1.5}$$

where T is the absolute temperature.

The vapor pressure and the CRH for the saturated urea solution are listed in Table 1.2.[17]

Table 1.2: Vapor pressure and CRH of a saturated urea solution at different temperatures.

Temperature [°C]	$P_{(s)}H_2O$ [Pa]	CRH [%]
25	2452	77.4
30	3186	75.1
35	4080	72.6
40	5153	69.9

The chemical composition has an effect on the caking tendency. The CRH is generally lowered when the material contains impurities or is mixed with other fertilizer salts. The size, shape and plasticity of particles are also very important. Normally, the products with a good spherical morphology and uniform in size and shape are less sensitive for caking.[19]

The external factors include the temperature to which the fertilizers are exposed, the humidity of surrounding atmosphere, the duration of storage and the acting pressure on the particles. The caking tendency decreases with lower temperature, lower humidity, shorter storage time and at lower acting pressures.[20,21]

During the storage of fertilizer granules, internal and external factors mutually influence the caking tendency. For example, with the water uptake of granules, their plasticity becomes lower, which makes them more sensitive to pressure resulting in an easier deformation. A similar situation can be observed for phase contacts and adhesive contacts which play combined a crucial role during the caking of granules.

The fertilizer industry has adopted various ways to prevent caking, including the conditions under which the fertilizer granules are produced and stored; improvement of manufacture equipments and the addition of anti-caking agents, etc. Thus, the fertilizers do not have a tendency to cake when various drying and cooling processes are used to obtain products with low moisture content. The control of storage conditions such as relative humidity, temperature, pile height, material for package and storage time are helpful to obtain free-flow products.[16] The general principle of these procedures is to decrease the water uptake of fertilizers by lowering temperatures and humidity.

Another very important caking prevention option is the application of anti-caking agents. An anti-caking agent is a material added to a fertilizer for promoting the maintenance of good physical conditions (free-flow ability) during storage and handling.[16] Depending on application methods, anti-caking agents can be divided into two types, coating agents and internal conditioners.[16,17,18,19,20] Coating agents are divided into two categories according to their physical and chemical properties, namely, surface active types and non-surface active types.[16] These anti-caking agents function by various mechanisms. Non-surface active type

agents, such as powder type agents, are normally inert powders, e.g. kaolin clays, diatomaceous earth and talc, which function as mechanical barriers between granules and serve to absorb, spread, and inactivate any solution phase that may occur on particle surfaces. [16,17,18,19,20] The application of dust-type agents also adjust the plasticity of fertilizers to a certain level where caking is less severe. Nowadays, the use of powder type agents is reduced since they can lead to a serious air pollution problem when applied extensively. Other non-surface active anti-caking agents of the oil type are mainly based on paraffin wax, synthetic polymers and different kinds of oil. The anti-caking mechanism is based on the formation of a hydrophobic layer on the surface of fertilizer granules, thus improving the water repellence. They can be used exclusively or in combination with an inert dust (powder agent). In recent decades, the most popularly and extensively used agents are surface active coating agents due to their low costs and high efficiency. The main constituents of surface active anti-caking agents are amphiphilic species (surfactant). Surfactants function by altering the interfacial tension between two immiscible phases. For solid-liquid interfaces, they reduce capillary adhesion between particles and they inhibit nucleation or modify crystal growth.[16] The relationship between surface tension and capillary adhesion is given by equation 1.6[22]

$$F_c = 2\gamma \cos\theta / r \qquad (1.6)$$

where F_c is the capillary adhesion, γ is the surface tension of the liquid bridge on the granule surface, r is the radius of the meniscus that is formed by two adjacent granules, and θ is the contact angle (see Figure 1.2).

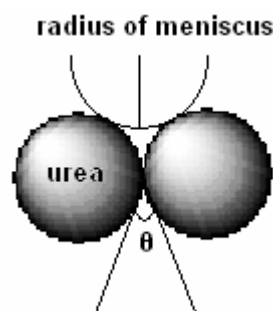Figure 1.2: Schematic representation of two caked granules.

Therefore, it can be concluded the smaller the surface tension of the liquid bridge on the granule surface, the smaller the capillary adhesion (i.e. less caking tendency). Thus, surfactants are used in coating solutions to lower the surface tensions. Although the surfactants play an important role on caking prevention by reducing the capillary adhesion

and the hygroscopic properties, the mechanical strength is not strong enough when they are used exclusively as an anti-caking agent on the granules. It is reported that the combination of a surfactant with a water soluble polymer in the coating solution improves significantly the anti-caking effect.[23,24] The water soluble polymer not only forms a complex with the surfactant for the solublization of micelles, but increases also the anti-abrasion property after the solution is coated and dried on the granule surface.

Different fertilizers require various types of coating agents. Anti-caking agents are selected according to the CRH of the fertilizer, the storage time and the application procedure of the fertilizers. For example, fertilizers based on ammonium sulphate and urea have a CRH value of 56.4 % at 30 °C. They are usually coated by paraffin wax for anti-caking. However, surface active coating agents are simultaneously applied on the urea granules.[25]

Surface active coating agents are usually solutions. Such properties as viscosity and density are related to the final thickness of the granule coating. A quantitative relationship is given in Equation 1.7[26]

$$h_t = k_p (\eta U / \rho g)^{1/2} \tag{1.7}$$

where h_t is the thickness of coating, U is the withdrawal rate, k_p is the proportionality constant, ρ and η are density and viscosity, respectively.

Surfactants which contain both hydrophilic and hydrophobic segments in one molecule are the main constituent of surface active anti-caking agents. The part of the molecule, which has an affinity for polar solvent, such as water, is considered to be hydrophilic. In contrast, the part of the molecule, which has affinity for non-polar solvents, such as hydrocarbons, is assumed to be hydrophobic. Molecules containing both types of components are also called as amphiphilic (see Figure 1.3). The primary classification of surfactants is made on the basis of the charge of the polar group. It is common practice to divide surfactants into four classes, anionics, cationics, non-ionics and zwitterionics. The former two are also named ionic surfactants. Salts of carboxylic acids and sulphuric acid esters are typical anionic surfactants. Cationic surfactants mainly include ammonium compounds with the general formula $R'N^+X^-$, where X^- is frequently a chloride anion and R represents an alkyl group.[27,28] The most common non-ionic surfactants are those based on ethylene oxide, referred to as ethoxylated surfactants.[29,30,31]
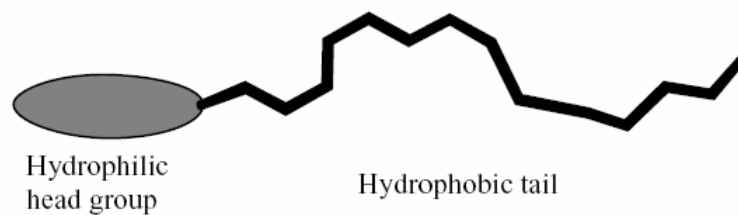
Figure 1.3: Schematic illustration of a surfactant.

One of the most characteristic features of surfactants is their tendency to adsorb at interfaces. When surfactants are added to water, the hydrocarbon chains interact weakly with water molecules, whereas the polar or hydrophilic groups interact strongly with water molecules via dipole or ion-dipole interactions. It is this strong interaction with the water molecules that renders the surfactants soluble in water. However, the cooperative action of dispersion forces and hydrogen bonding between the water molecules tends to squeeze the hydrocarbon chains out of water. The driving force for surfactant adsorption is the lowering of the free energy when they are located at the phase boundary of two immiscible phases. The interfacial free energy, referred to as surface or interfacial tension γ is given in mJ/m^2 or mN/m.[29,30] Adsorption of surfactant molecules at the interface lowers the interfacial tension and the higher the surfactant adsorption (i.e. the denser the layer) the larger the reduction of the interfacial tension. The degree of surfactant adsorption at the interface depends on the surfactant structure and the nature of the two phases which form the interface.[32,33]

Another fundamental property of surfactants is that unimers in solution tend to form aggregates, so-called micelles. Micelle formation or micellization can be viewed as an alternative mechanism to adsorption at interfaces for removing hydrophobic groups from contact with water, thereby reducing the free energy of the system. This process is governed by the concentration of free surfactant unimers in solution. It is important that surfactant molecules behave very different when present in micelles compared to their behavior as free unimers in solution. Only surfactant unimers contribute to surface or interfacial tension reduction and dynamic phenomena such as wetting and foaming.[32,33] The physical properties of surfactants differ from those of small or non-amphiphilic molecules in one major aspect, namely the abrupt changes in their properties above a critical concentration.[32,33] Figure 1.4 illustrates schematically the change of several physical properties (osmotic pressure, turbidity, solubilization, and surface tension) as a function of concentration for an ionic surfactant.[34] The concentration at which these association phenomena occur is known as the critical micelle concentration (CMC). Each surfactant species has a characteristic CMC at a given temperature and electrolyte concentration. The most common technique for measuring CMC

is the determination of the surface tension as a function of concentration. The surface tension decreases with increasing surfactant concentration until the CMC is reached. Then, the surface tension remains virtually constant with increasing surfactant concentration.
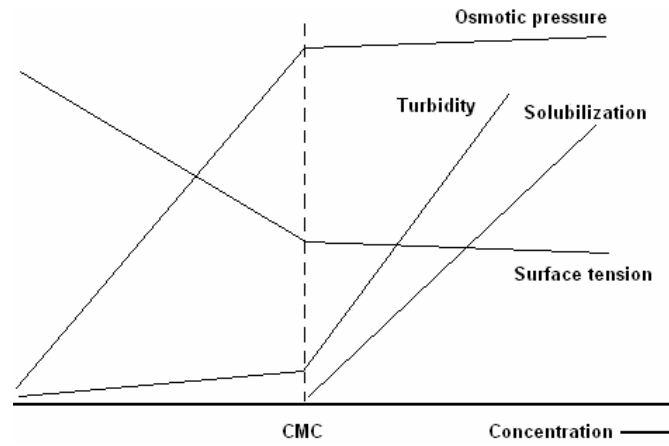

Figure 1.4: Dependence of several physico-chemical quantities on the surfactant concentration near to the critical micelle concentration.[34]

Micellization is a dynamic phenomenon in which n monomeric surfactant molecules associate to form a micelle S_n

$$nS \Leftrightarrow S_n \tag{1.8}$$

Above CMC, micelle formation is a dynamic equilibrium whereby the surfactant molecules are constantly leaving and entering from the solution and the micelles.[35] The laws of thermodynamics are applied to obtain the free energy, enthalpy and entropy of micellization. Two general approaches have been employed to deal with micelle formation (i) the phase separation model and (ii) the mass action model. For a non-ionic surfactant, the standard free energy of micellization per mol of monomer ΔG_m^0 is given by

$$\Delta G_m^{\theta} = RT \ln CMC \tag{1.9}$$

where R is the ideal gas constant and T is the temperature at which CMC is measured.

For an ionic surfactant, when most charges are associated with counter ions, the standard free energy can be modified[32,33]

$$\Delta G_m^{\theta} = 2RT \ln CMC \tag{1.10}$$

In aqueous solution, the surfactant self-assembly leads to different structures which can be obtained depending on the concentration.[36,37] Spherical micelles are characterized by a low numbers of surfactant molecules (critical packing parameter) and a strong spontaneous curvature. Surfactant bi-layers form lamellar liquid crystals having a hydrocarbon layer with a thickness of around 80% of the length of two extended alkyl chains.[34] Inverse micelles occur in non-polar solvents with a water core surrounded by the corona of non-polar head groups. The alkyl chains together with a non-polar solvent make up the continuous medium. Like 'normal' micelles, they can grow into cylinders.[38,39]

The solubility-temperature relationships between ionic surfactants and non-ionic surfactants are significantly different, even an opposite situation can be observed. The mechanism of dissolution of an ionic surfactant is the cleaving of the ionic bond between the polar group covalently bound to the long alkyl group and its counter ion. Many ionic surfactants show dramatic temperature-dependent solubility. The solubility may be very low at low temperatures and then increases by an order of magnitude in a relatively narrow temperature range. This phenomenon is generally denoted as Krafft phenomenon. The temperature for the onset of increasing solubility is known as the Krafft temperature.[40] In contrast, the mechanism of non-ionic surfactant solubility is based on the formation of hydrogen bonds between hydrophilic parts of the amphiphilic molecule (e.g. the ethoxylate group) and water (if the solvent is water). When the temperature is gradually increased for PEO based amphiphiles in water, the solution becomes cloudy due to dehydration of the PEO chain. The hydrogen bonds between the EO group and water are destroyed by increasing the temperature. The temperature at which this occurs is referred to as the cloud point. At a given alkyl chain length, cloud points increase with increasing EO chain length of the molecule.[32,33] The cloud point is also affected by the presence of electrolyte or organic compounds in the aqueous solution.[32,33]

For surface active anti-caking agents, water soluble polymers are used to solubilize micelles which lead to an increase of the surface activity of the surfactant. Poly(vinyl alcohol) (PVA) is most frequently used for this purpose. It is commercially produced exclusively by the hydrolysis of poly(vinyl acetate) since monomeric vinyl alcohol cannot be obtained due to its thermodynamic instability.[41] Thus, the physical properties of the poly(vinyl alcohol) are highly dependent upon those of the residual poly(vinyl acetate) monomeric units that remain in the PVA. The hydrolysis reaction is shown in the Figure 1.5.
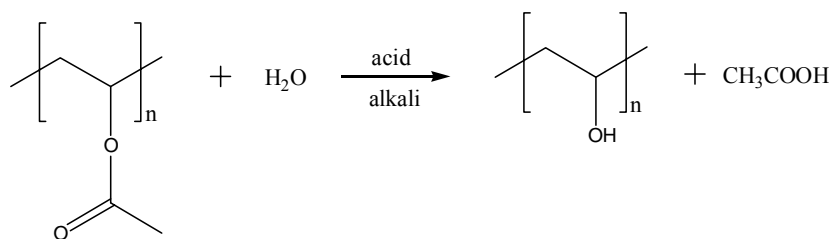
Figure 1.5: Hydrolysis of poly(vinyl acetate) to obtain poly(vinyl alcohol).

Poly(vinyl alcohol) is used mainly in aqueous solutions. Its solubility in water depends on its degree of polymerization and the degree of hydrolysis. The effect of the latter is especially significant. Many hydroxyl groups allow PVA to have a high affinity to water. However, the strong intra- and intermolecular hydrogen bonding between hydroxyl groups reduces the affinity of PVA to water. On the other hand, the residual acetate groups in partially hydrolysed PVA are essentially hydrophobic, and weaken the intra- and intermolecular hydrogen bonding of adjoining hydroxyl groups. The presence of an adequate amount of these acetate groups improves the water solubility.[42] The viscosity behavior of PVA solutions is different depending on their average molar mass, degree of hydrolysis and concentration.[43] Ŝtern and Prokopová reported that the viscosity of low molar mass PVA decreases very slightly in a freshly prepared solution with increasing shear rate and the flow behavior is nearly Newtonian.[44,45] PVA in bulk is a semi-crystalline substance. Many thermal properties of PVA, such as melting temperature and glass transition temperature, vary as a function of the degree of hydrolysis.[46,47,48,49,50,51,52]

Another water soluble polymer frequently used as an additive is poly(vinyl pyrrolidone) (PVP). PVP is made from the monomer N-vinyl pyrrolidone. The structure is shown in Figure 1.6.
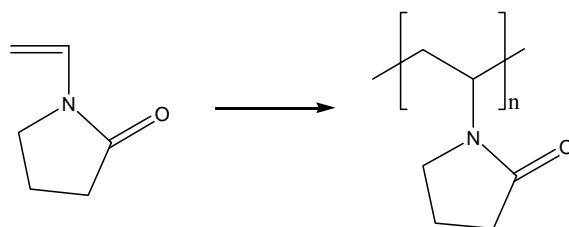
Figure 1.6: The structure of N-vinyl pyrrolidone and poly(vinyl pyrrolidone).

PVP is usually used in personal care products, such as shampoos and toothpastes, in paints, and adhesives that need to keep some moisture, such as postage stamps and envelopes. Numerous reports have described the application of PVP together with other polymers or surfactants.[53,54] El Gamal et al. have studied the properties of mixed aqueous solutions of urea

and PVP for pharmaceutical applications.[55] PVP is also used as a crystallization inhibitor because of its amorphous structure.[56]
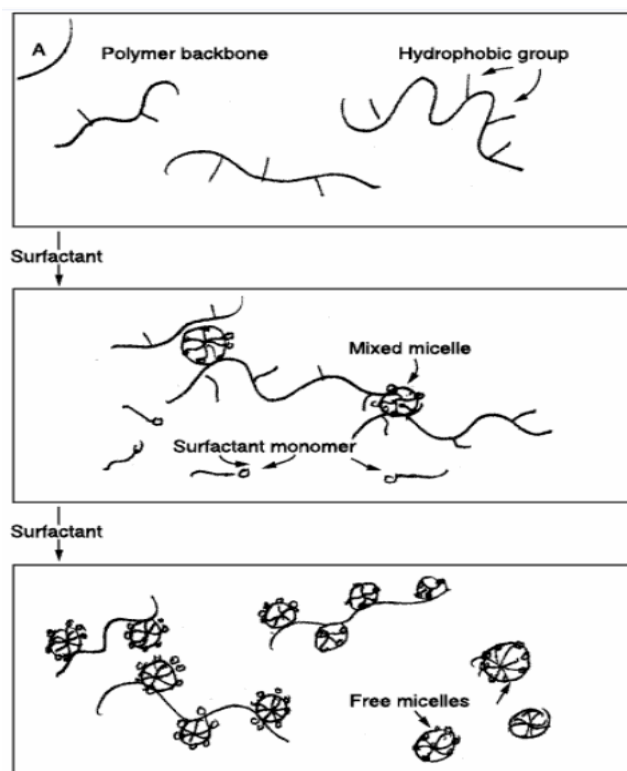

Figure 1.7: The schematic representation of interaction between polymers and surfactants.[32]

Mixtures of surfactants and polymers are very common for many industrial formulations.[57] In many systems, such as personal care and cosmetics, water soluble polymers are added to enhance the function of the system. The interaction between surfactants and polymers results frequently in synergistic effects, e.g. solubilization, enhancing the surface activity, stabilizing foam and emulsions, etc.[58,59] In a system of fixed polymer concentration and varying surfactant concentrations, two critical concentrations appear, denoted C_1 and C_2. C_1 represents the concentration at which first interactions between the surfactant and the polymer occur. This is sometimes termed the critical aggregation concentration (CAC). Because of this, there is no further increase in surface activity with increasing surfactant concentration and thus no lowering of surface tension. C_2 represents the concentration at which the polymer becomes saturated with surfactant.[33,34] Since C_1 is generally lower than CMC of the surfactant in the absence of polymer, adsorption or aggregation of surfactant on or with polymer is more favorable than normal micellization. As the polymer is satured with surfactant (above C_2), the surfactant unimer concentration and the activity start to increase again and there is a lowering of surface tension until CMC is reached. The driving force for polymer-surfactant interaction is the same as that for the process of micellization. As with micelles, the main driving force is

the reduction of hydrocarbon/water contacts of the alkyl chain of the dissolved surfactant. The interaction between ethoxylated surfactants and non-ionic polymers is weak, however, the interaction can be stronger between ionic surfactants and polymers.[60,61,62] The schematic representation of interaction between polymers and surfactants are shown in Figure 1.7.[32]

1.3   Iron oxide nanoparticles

Nanomaterials and nanoparticles are materials that have structural components smaller than 1 μm at least in one dimension. Nanoparticles have potentially dimensions as small as atomic and molecular length scales (~ 0.2 nm).[63] Nanostructured materials include both natural (e.g. viruses, bacteria and proteins) and man-made substances that have already existed for a long time. For man-made nanomaterials, the most advanced nanotechnological fabrication process is microelectronic fabrication where thin film coatings and lithography are used to create micro- and nanosized features for computer chips.[63] Classified by the dimensionality, nanomaterials can be divided into one-dimensional, two-dimensional and three-dimensional materials. Taking into consideration the shape of nanomaterials, they can be particles, wires, or nanotubes, etc. Composites of nanomaterials with other materials have been reported by various research groups.[64,65] These synthetic nanocomposites can be amorphous or crystalline for various fields of application.[66,67,68,69] There are two primary factors leading to the significantly different behavior of nanomaterials compared to that of the bulk materials (i) surface effects (causing continuous properties scaling due to the fraction of atoms at the surface) and (ii) quantum effects (showing discontinuous behavior due to quantum confinement effects in materials with delocalized electrons).[70] Compared to microparticles, nanoparticles have a very large surface area and a large particle number per unit mass. The atoms located at the surface have fewer neighbors than bulk atoms resulting in a lowered binding energy per atom with decreasing particle size.[70] Consequently, the melting point is reduced with particle radius resulting from the smaller binding energy per atom. This is quantitatively expressed in the Gibbs-Thomson equation.[70] Due to the quantum effects, nanoparticles have magnetic moments different from the respective bulk materials (e.g. in nanoparticles of gold, platinum or palladium).[71] Iron oxide nanoparticles possessing intrinsic magnetic properties have been extensively exploited for applications in sensors, magnetic storage media, catalyst,[72,73,74] and for biomaterials in pharmaceutical fields.[75] Due to their very small size, usually from 50 – 100 nm,[76] nanoparticles can penetrate physiological barriers and transport within the circulatory systems of a biological host.[63] Numerous reports have already described synthesis and characterization of iron oxide nanoparticles,[77] e.g. the

use of block copolymers as templates for preparation of nanoparticles.[78,79] The classification of nanoparticles is mainly based on their dimensionality, morphology, composition, uniformity and agglomeration.[63]

1.4   Aggregation-prevention of iron oxide nanoparticles

The aggregation of nanoparticles is a very common phenomenon observed during the storage or even immediately after the manufacture. Nanoparticles surrounded by a diffuse layer (electrical cloud) are similar to an ion situated in the center of an ionic cloud. Therefore, the aggregation of nanoparticles can be considered as a two step mechanism, (i) the transition step and (ii) the binding step (activated complex) which is a pair of two interacting particles with a common electrical cloud.[80] A quantitative description of the mechanism of nanoparticle aggregation is summarized by Kallay et al.[80] They follow the Brønsted concept which is based on the Transition State theory using the activity coefficients (see equation 1. 11, Debye-Hückel law).[81,82]

$$r_a = k_a [X^{zx}][Y^{zy}] \qquad (1.11)$$

where r_a is the rate of aggregation and k_a is the rate coefficient of aggregation, z denotes the charge number. In terms of the Brønsted concept, firstly, the two nanoparticles undergo a reversible formation of the transition state with the charge number being equal to the sum of the charges of the interacting species.[80] The second step is the slow transition state XY^{zx+zy} binding step (1.12).[80]

$$X^{zx} + Y^{zy} \leftrightarrow XY^{zx+zy} \rightarrow XY^{zxy} \qquad (1.12)$$
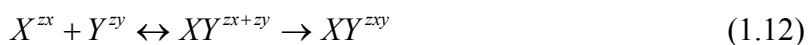
therefore, the overall rate of reaction is proportional to the concentration of the transition state (see equation 1.13).

$$r_a = k_a^{'} [XY^{zx+zy}] \qquad (1.13)$$

where $k_a^{'}$ is the rate coefficient of the second process.[80]

This kind of the binding is caused by the overlapping of the electrical interfacial layer, i.e. the dipolar interaction between two particles.[83] The free energy of nanoparticles aggregation has

been discussed by Spagnoli et al. based on simulations.[84] In an agglomerated state of nanoparticles, they may behave as the bulk materials depending on the size of the agglomerate.[80] The specific and unique properties of the nanomaterials are lost. Most applications of nanomaterials require them to possess good chemical and physical stability and uniform size.

Nowadays, the most used and smartest method to avoid the aggregation of nanoparticles is to modify their surface with non-polar materials, frequently, long alkyl chain molecules or amphiphilic block copolymers.[85,86] The repulsion between nanoparticles is increased by the hydrophobic chains. The use of polymers or surfactants as ligands or stabilizing agents not only prevents the agglomeration of the nanoparticles for obtaining chemical and mechanical stabilities but also induces various functionalities caused by the polymeric shell such as biocompatibility and molecular recognition.[87,88,89]

Chapter 2

Investigation of anti-caking agents for fertilizer granules

2.1   Introduction

Solid fertilizers have the tendency to form lumps or agglomerates during storage and transportation. The caked fertilizers not only result in the loss of nutrition and energy due to the de-agglomeration process, but they face also serious problems during the fertilizer drill. A quality fertilizer should be as free flow, dust free, and non-hygroscopic as possible. In order to avoid or minimize the caking of fertilizers, in this study, surface-active anti-caking agents (solutions) are applied to be coated onto the granules surface. They consist of a water soluble polymer, a surfactant and a nitrification inhibitor (see Chapter 1.2).

In this chapter, the physical chemistry properties of various surfactants are investigated, such as the critical micelle concentration (CMC). And the influence of CMC values by hydrophilic-lipophilic balance (HLB) (HLB values are calculated using the molar mass of surfactants) are discussed.[30,32] The chemical composition of anti-caking solutions is described. Furthermore, some physical properties of anti-caking solutions, such as surface tensions, viscosities and densities are determined at different temperatures which are related to the anti-caking effect and the application in technical scales.

2.2   Experimental section

2.2.1   Materials

The surface active agents T2, T4, T6, T8, and B3 were purchased from Sigma Aldrich; PE6 and PE8 were provided by BASF. Physical properties of surfactants are summarized in Table 2.1.

Various poly(vinyl alcohol)s with different average molar masses and degrees of hydrolysis were applied in the anti-caking solutions. P1, P2, P3 and some technical PVAs for industry application listed as P98, P01, P03, P80, P81, P37, P15 and P16 were purchased from Sigma Aldrich and Fluka. Poly(vinyl pyrrolidone) was purchased from Sigma Aldrich.

Table 2.1: Physical properties of surfactants.

Surfactant	Nomenclature	Chemical formula	Molar mass [g/mol]	HLB	Density [g/cm³]
F8	Ceteareth-23	$C_{46}H_{93}O_{24}R$	2648	16	-
T2	Poly(oxyethlyene sorbitan monolaurate)	$C_{58}H_{114}O_{26}$	1228	16.7	1.095
T4	Poly(oxyethlyene sorbitan monopamitate)	$C_{62}H_{122}O_{26}$	1284	15.6	1.083
T6	Poly(oxyethylene sorbitan monostearate)	$C_{64}H_{126}O_{26}$	1312	14.9	1.044
T8	Poly(oxyethylene sorbitan monooleate)	$C_{64}H_{124}O_{26}$	1310	15	1.064
B3	Poly(oxyethylene lauryl ether)	$C_{58}H_{118}O_{24}$	1200	16.9	1.03
PE6	Poly(ethylene glycol-co-propylene oxide)	$H(OC_3H_6)_y(OC_2H_4)_xOH$	1962	3	1.02
PE8	Poly(ethylene glycol-co-propylene oxide)	$H(OC_3H_6)_y(OC_2H_4)_xOH$	2574	2	1.03
F9	Nonoxynol	$C_{34}H_{62}O_{10.5}$	639	13	1.06

All values are from the literature and safety data sheet: HLB values are from ref.[90,91].

Preparations of PVA-Surfactant (PS) solutions

For each sample, 17 g PVA, 1 g surfactant (or 2.2 g F8) and 82 g double distilled water (80.8 g double distilled water when 2.2 g F8 were used) were added into a glass bottle and sealed. The samples were placed in the oven at 95 °C for 4 h to dissolve the PVA. After 4 h, these sample solutions were taken out from the oven and mixed using a stir bar until they were homogenous.

Preparations of PVA-Surfactant-NI (PSN) solutions

The procedure was similar to the preparation of the PS solutions. 11.4 wt% PVA and 33 wt% NI were required in the sample solutions, i.e. 8.5 g PVA, 0.75 g surfactant, and 41 g double distilled water were added into the glass bottle and sealed. Sample solutions were placed in the oven at 95 °C for 4 h. After that, sample solutions were taken out from the oven and stirred until homogenous. When the temperature of solutions decreased to room temperature (approximately 20 – 25 °C), 24.375 g NI were added into solutions and stirred until they were totally dissolved.

Preparations of PVP-Surfactant-NI (VSN) solutions

The preparation procedures of VSN solutions were similar as PSN solutions. 11.4 wt% PVP and 33 wt% NI were required in the sample solution, i.e. 8.5 g PVP, 0.75 g surfactant, 24.375 g NI and 41 g double distilled water were added into the glass bottle and sealed. Sample solutions were stirred at the room temperature for ~ 30 min until homogenous.

2.2.2   CMC and surface tension measurements

Surface tensions of PS and PSN solutions were measured using a tensiometer DCAT11 (Dataphysics Instruments GmbH). The measurements were carried out using the Wilhelmy plate method, i.e. by placing the plate partly (3 mm) underneath the surface of the solution and recording the force with which the plate was pulled downward. The maximum tension acts on the balance at this instant. The surface tension of the solutions can be obtained by the following equation:

$$\gamma = \frac{F}{L \cdot \cos\theta} \tag{2.1}$$

where γ is the surface or interfacial tension, L is length of the wetting liquid on the plate, F is the force acting on the balance and θ is the contact angle. In this experiment, the contact angle is not measured, instead complete wetting ($\theta = 0$) is assumed. The CMC values of various surfactants in aqueous systems were determined with the aid of surface tension measurements.

2.2.3   Viscosity and density measurements

The viscosity measurements were carried out using a couette type Viscotester (VT550 Gebr. HAAKE GmbH). Viscosity is related to the shear stress and the shear rate. The sample to be measured was located in the measuring gap of the sensor system (cylinder system, see scheme 2.1). The rotor was rotated with rotor speed of s. The sample solution exerted a resistance to this rotational movement due to its viscosity. This was measured as a torque value M_d. The viscosity is given by:

$$\eta = \frac{f \cdot M_d}{M \cdot s} \tag{2.2}$$

$$f = \frac{0.01}{2\pi L_r R_i^2} \qquad (2.3)$$

$$M = \frac{\pi}{15} \frac{R_{a0}^2}{R_{a0}^2 - R_i^2} \qquad (2.4)$$

where η is the viscosity of the solution, s is the rotor speed, f and M are the constants defined by the apparatus, L_r is the rotor length, R_{a0} and R_i are the radius of the outer cylinder and cone, respectively.
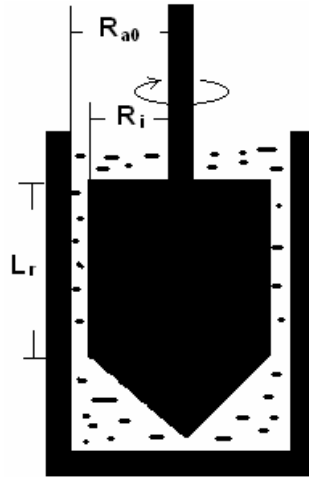
Scheme 2.1: Schematic representation of a couette geometry for rheometry.

The densities of the solutions were measured using oscillating U-tube method (DMA4500 Anton Paar GmbH). The vibrating U-tube density measurement method was based upon measuring the frequency of oscillation of a U-shape tube filled with the sample solution. The vibrating tube was likened to a vibrating mass spring. The frequency of the vibration corresponded to the spring constant and the vibrating mass (see equation 2.5). Density values were obtained from the period of oscillation of a tube containing the sample under investigation.

$$f = (1/2\pi)\sqrt{k_s / M_v} \qquad (2.5)$$

$$\rho - \rho_0 = k_s \cdot (\tau^2 - \tau_0^2) \qquad (2.6)$$

where k_s is the spring constant, M_v is the vibrating mass, ρ is density of the sample, ρ_0 is the reference density (air), τ is the period of oscillation with the sample solution and τ_0 is the period of oscillation of air in the U-tube.

2.3   Results and discussion

2.3.1   CMC measurements of surfactants in aqueous systems

Surface tension measurement over a wide range of concentration is one of the several methods used for the CMC determination of the low molar mass surfactant. CMC values of various surfactants in aqueous system are measured at three temperatures, i.e. 10, 25, and 40 °C, respectively. They can be determined by measuring the surface tension of the surfactants-water systems after increasing the surfactants concentration in water stepwise. CMC values of T2 and T8 measured at 40 °C are shown in Figure 2.1a and b.
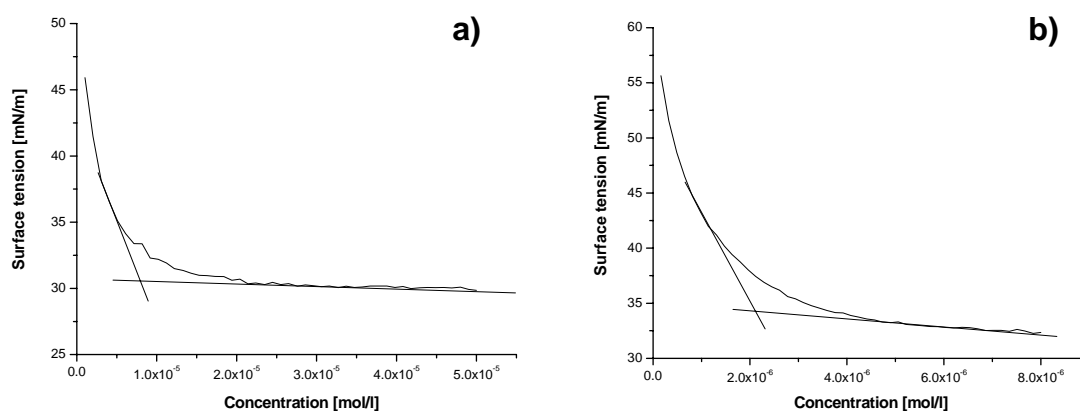

Figure 2.1: CMC values of T2 (a) and T8 (b) measured at 40 °C. The CMC values are indicated by cross points.

It can be seen that the surface tension decreases sharply with increasing surfactant concentration below CMC. At concentrations above CMC the surface tensions remain almost constant. The CMC value for T2 is 9.18×10^{-6} mol/L and for T8 is 2.12×10^{-6} mol/L at 40 °C. The surface tensions at CMC for T2 and for T8 are 30 mN/m and 34 mN/m, respectively. The detailed CMC results of various surfactants used in this study are shown in Table 2.2.

It is obvious that the CMC values of all surfactants decrease with increasing temperatures as the typical behavior for non-ionic surfactant.[92] CMC values of T series products (T2, T4, T6 and T8 have an identical hydrophilic part) reach values of the order of 10^{-6} mol/L. The main difference in the chemical structure (see Appendix) between T series surfactants is the hydrophobic block having various lengths of alkyl chains, e.g. T6 is the one with 17 carbon atoms of the alkyl chain, however T2 has only 11 carbon atoms of the alkyl chain. When measured at the same temperature, e.g. at 40 °C, the CMC value of T6 is smaller than that of

T2 indicating that the CMC values of the surfactants decreases with increasing alkyl chain length. It is caused by a stronger repellence between the longer alkyl chain and water. This is an agreement with the report by Israelachvili.[93] The similar phenomenon is observed for the surfactants B3 and F8. The CMC value of F8 is much smaller than that of B3 measured at the same temperature due to the longer alkyl chain of the hydrophobic part of F8. CMC values of both PE6 and PE8 are in the of the order of 10^{-7} mol/L at all three temperatures.

Table 2.2: CMC values of various surfactants measured at different temperatures.

Surfactants	CMC at 40°C [mol/L]	CMC at 25°C [mol/L]	CMC at 10°C [mol/L]
F8	3.06×10^{-07}	3.27×10^{-07}	3.88×10^{-07}
T2	9.18×10^{-06}	1.02×10^{-05}	1.12×10^{-05}
T4	5.51×10^{-06}	6.73×10^{-06}	7.96×10^{-06}
T6	4.08×10^{-06}	4.90×10^{-06}	5.71×10^{-06}
T8	2.12×10^{-06}	2.29×10^{-06}	2.45×10^{-06}
B3	1.71×10^{-05}	2.08×10^{-05}	2.33×10^{-05}
PE6	1.84×10^{-07}	2.04×10^{-07}	2.24×10^{-07}
PE8	7.35×10^{-07}	8.57×10^{-07}	9.18×10^{-07}
F9	5.71×10^{-06}	6.12×10^{-06}	6.94×10^{-06}

As discussed above, different CMC values can be obtained when measured at different temperatures. Therefore, the measurements of the temperature dependence of the CMC values of surfactants are used to obtain thermodynamic parameters of micellization.[94] In accordance with the mass action model, the standard free energy of micelle formation per mole of monomer, ΔG_m^θ, is given by Equation 1.9. The modified version is given by Equation 2.4[32]

$$\ln CMC = \frac{\Delta G_m^\theta}{RT} \qquad (2.6)$$

where CMC is the mole fraction of the surfactant in aqueous solution at CMC. Thus, lnCMC is a linear function when plotted over 1/T. Three different CMC values of surfactants are obtained for three different temperatures (see Table 2.2). Therefore, representative plots of lnCMC versus the inverse temperature are presented in Figure 2.2.
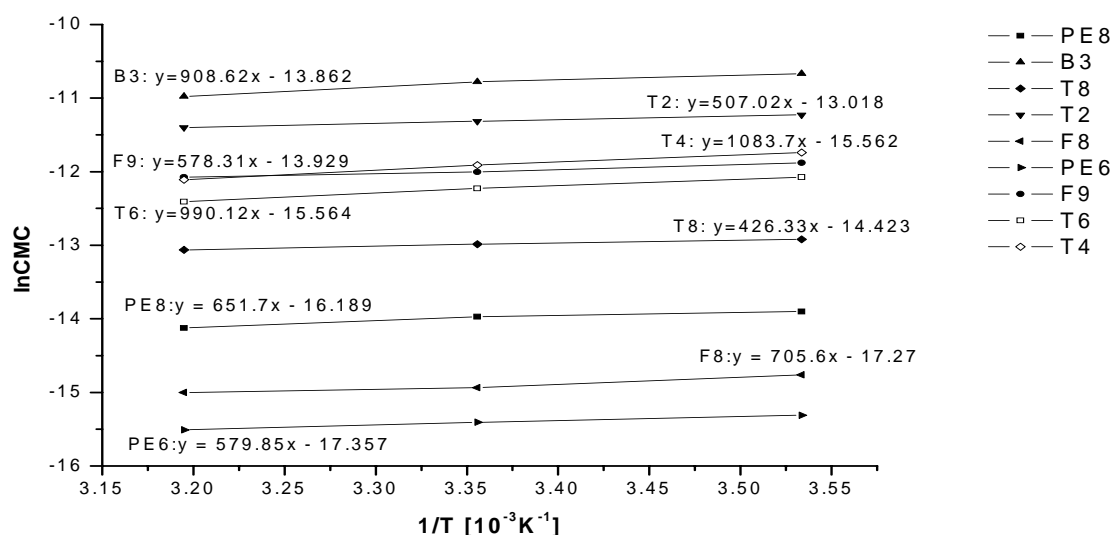
Figure 2.2: Plots of the lnCMC versus inverse of temperature.

Assuming lnCMC as Y and 1/T as X, it is possible to obtain the thermodynamic parameters by fitting to the linear equation. The slope of curves is then $\Delta G_m^\theta/R$. From all the linear equations in Fig. 2.2, T8 has the lowest slope, i.e. $\Delta G_m^\theta/R$ = 426 K. It indicates that it has the similar free energy of micellization for all temperatures and the most stable surface active effect at different temperatures. In other words, the smallest temperature dependence of CMC of T8 results in the most stable surface activity performance in summer and winter time when T8 is applied in anti-caking solutions. T2 and F9 are the next two surfactants with the smallest slopes, $\Delta G_m^\theta/R$ is equal to 507 and 578 K, respectively. In contrast, the CMC of T4 and T6 depend strongly on temperature due to their largest slope values obtained by the linear fits.

2.3.2 Surface tensions of PS, PSN and VSN solutions

The surface tensions of PS, PSN and VSN solutions (anti-caking solutions) are measured by the Wilhelmy plate method at 10 °C, 25 °C and 40 °C. Figure 2.3a and b show surface tensions of PS solutions when different PVA samples (e.g. P1, P2 and P3) are used in the solutions. It can be observed that the surface tensions of PS solutions are quite similar when different PVAs are used. A similar phenomenon is observed for PSN solutions, i.e. similar surface tensions are obtained at all temperatures when different PVAs and NI are used in solutions (see Figure 2.3c and d). Tadros et al. have already mentioned that uncharged polymers interact weakly with non-ionic surfactants.[95] Furthermore, above CMC, the surface

tension of 30 mN/m of T2 in aqueous solution is measured at the temperature of 40 °C (see Figure 2.1a). This value is similar as the surface tension the PVA-T2 solution (PVA was added in the T2 solution) at 40 °C (Figure 2.3 a) indicating a weak interaction between T2 and the PVA in the solution. However, when T8 mixed with PVA (Figure 2.3b), the measured surface tension of 30 mN/m is smaller than that of neat T8 in aqueous solution above the CMC at 40 °C (~ 34 mN/m see Figure 2.2). It can be assumed that a pronounced association between T8 and polymer took place due to a longer alkyl chain of hydrophobic block of T8.[95]
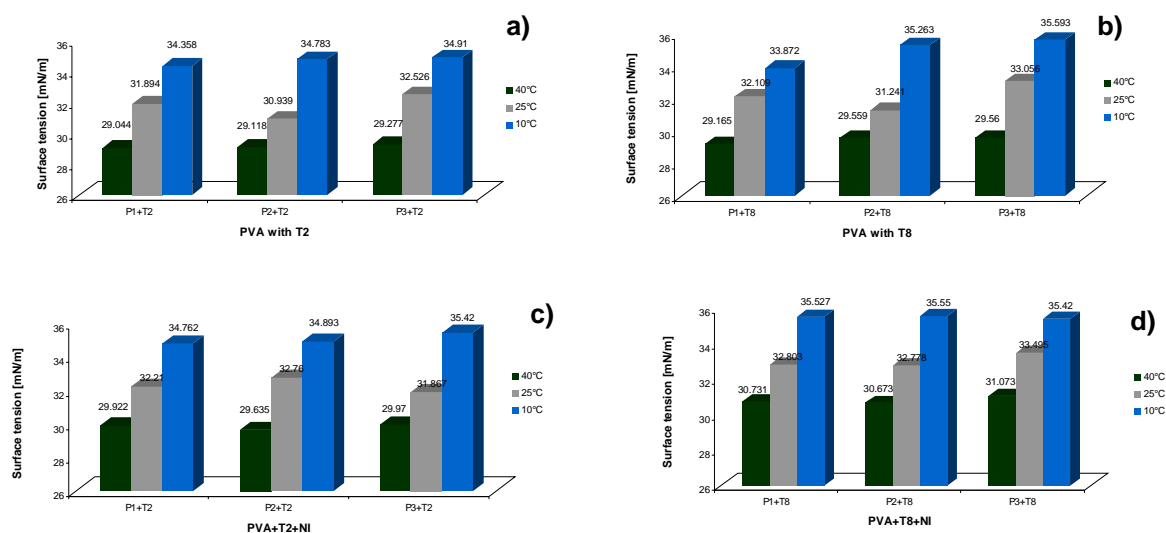

Figure 2.3: Surface tensions of PS and PSN solutions measured at 10, 25 and 40 °C. a) PVAs with T2, b) PVAs with T8, c) PVAs, T2 and NI, d) PVAs, T8 and NI.

The detailed data of P3-surfactant solutions are shown in Figure 2.4 (Surface tension values of P1-surfactant solutions and P2-surfactant solutions are not shown here since they have similar properties as P3-surfactant solutions). When T2, T8 and F9 are dissolved in water, they have the lowest similar surface tensions measured at three temperatures, i.e. 29 ± 0.8 mN/m at 40 °C; 32 ± 0.8 mN/m at 25 °C; 34 ± 0.7 mN/m at 10 °C. On the contrary, when F8 and B3 are used, the highest similar surface tensions are measured at all three temperatures (35 ± 0.7 mN/m at 40 °C, 38 ± 0.6 mN/m at 25 °C, 42 ± 1 mN/m at 10 °C). F8 aqueous solutions with two different concentrations (1 wt% or 2.2 wt%) were prepared. But their surface tension values are essentially the same at the measured temperature since their concentrations are already above CMC. Although surface tensions of T4 and T6 solutions at 25 °C and 40 °C have similar values as T2 and T8, however, their values at 10 °C are much higher than the respective T2 and T8 values. The significant change of surface tensions of T4 and T6 at different temperatures corresponds to their large values of ΔG_m^{θ}/R (see Figure 2.2),

i.e. surface active effects of T4 and T6 are strongly temperature dependence.
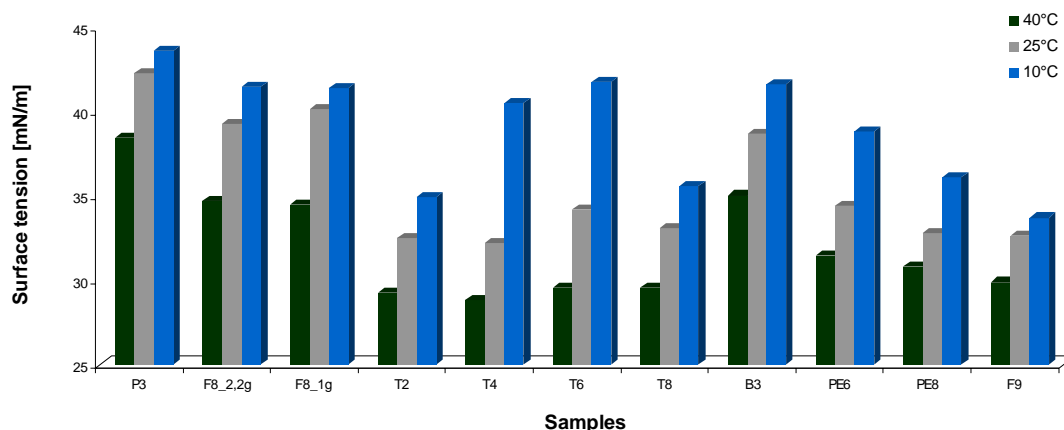

Figure 2.4: Surface tensions of P3-surfactant aqueous solutions measured at 10 °C, 25 °C and 40 °C.
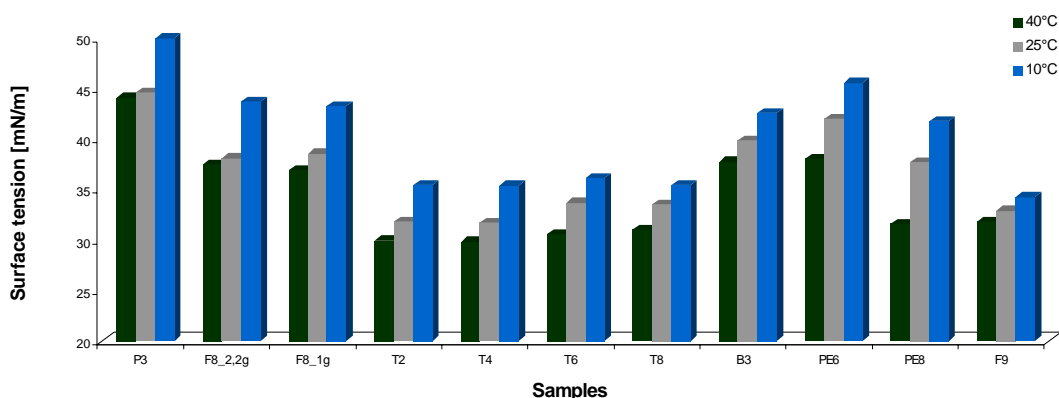

Figure 2.5: Surface tensions of P3-surfactant solutions in the presence of NI measured at 10, 25, 40 °C.

The surface tensions of P3-surfactant-NI solutions are shown in Figure 2.5 (surface tensions of P1-surfactant-NI solutions and P2-surfactant-NI solutions are not discussed here because similar phenomena are observed). When NI is added to the solutions, the solution systems (PSN solutions) become more complicated since both the amphiphilic molecules and the water soluble polymer influence the surface tension. Samples with surfactants T2, T8 and F9 have similar surface tensions as PS solutions (29 ± 0.8 mN/m at 40 °C; 32 ± 0.8 mN/m at 25 °C; 34 ± 0.7 mN/m at 10 °C) indicating a very slight influence of NI on the surface tensions of their solutions. But for the solutions with F8, B3, PE6 and PE8, the surface tensions show an increase of approximately 3 mN/m at each measured temperature. The addition of a polar

substance, e.g. NI, makes ethoxylate surfactants more diffuse into the water subphase leading to an increase of the surface tension.[96]

It is meaningful to study the variation of surface tension when organic substances i.e. NI, are added. Generally, the surface tension of pure water is ~ 72 mN/m at 25 °C. It is observed that there is a decrease of surface tension of ~ 5 mN/m when 33 wt% NI is dissolved in water without other additives. It is well known that organic compounds can weaken the surface tension of water and inorganic salts can increase the surface tension of water due to the hydration of ions.[36] Compared with PS solutions (the sample solutions without NI), PVA-T2-NI solution, PVA-T8-NI solution and PVA-F9-NI solution, their surface tensions have no dramatic changes at all three temperatures under investigation. The surface tensions are of the order of 29 mN/m at 40 °C, 32 mN/m at 25 °C, and 35 mN/m at 10 °C. Nevertheless, when F8, B3 are used in the solutions, the surface tensions increase approximately 2 mN/m at each temperature in comparisons of solutions in the absence of NI. For PE8, there is a 4 mN/m increase when NI is used in solutions. In particular, the surface tension of the PVA-PE6-NI solution increases 6 mN/m at all measured temperatures. The increase of surface tension is caused by the addition of a polar organic substance of NI. NI is much easier to form hydrogen bonds with water than the surfactants. When hydrogen bonds are formed, the so called dehydration happens, i.e. the hydrogen bond between hydrophilic group of surfactant and water is broken. Consequently, the surfactant tends to form micelles and lower the surface activity of the surfactant.[95,96] Therefore, the surfactants that are strongly influenced by organic compounds should be avoided to be used in anti-caking solutions. A comparison between surface tension data of PS and PSN solutions is listed in Table 2.3.

Table 2.3: Comparison of surface tensions between PS and PSN solutions.

Comparison of γ	Surfactant	γ_PVA-Surfactant solution [mN/m]			γ_PVA-Surfactant-NI solution [mN/m]		
Similar surface tension system	T2	40 °C: 29.28	25 °C: 32.52	10 °C: 34.91	40 °C: 29.97	25 °C: 31.86	10 °C: 35.42
	T8	40 °C: 29.56	25 °C: 33.05	10 °C: 35.59	40 °C: 31.07	25 °C: 33.49	10 °C: 35.42
	F9	40 °C: 29.88	25 °C: 32.67	10 °C: 33.71	40 °C: 31.85	25 °C: 32.9	10 °C: 34.25
Increasing surface tension system	PVA	40 °C: 38.48	25 °C: 42.26	10 °C: 43.62	40 °C: 44.12	25 °C: 44.62	10 °C: 50.97
	F8	40 °C: 34.48	25 °C: 39.27	10 °C: 41.51	40 °C: 36.93	25 °C: 38.56	10 °C: 43.26
	B3	40 °C: 35.04	25 °C: 38.69	10 °C: 41.62	40 °C: 37.77	25 °C: 39.88	10 °C: 42.58
	PE8	40 °C: 30.78	25 °C: 32.81	10 °C: 35.08	40 °C: 31.57	25 °C: 37.71	10 °C: 41.08
	PE6	40 °C: 31.48	25 °C: 34.43	10 °C: 38.84	40 °C: 38.05	25 °C: 41.99	10 °C: 45.57

Surface tensions of VSN (PVP-Surfactant-NI) solutions are shown in Figure 2.6. When T8,

T2 and F9 are used in the solutions, the smallest surface tension values can be obtained, i.e. 30 ± 0.8 mN/m at 40 °C, 32 ± 0.7 mN/m at 25 °C and 35 ± 0.8 mN/m at 10 °C. Although PVP is used in these anti-caking solutions, similar surface tensions compared to the PVA containing solutions are observed indicating that these polymers have minor effects on the aggregation with surfactants.
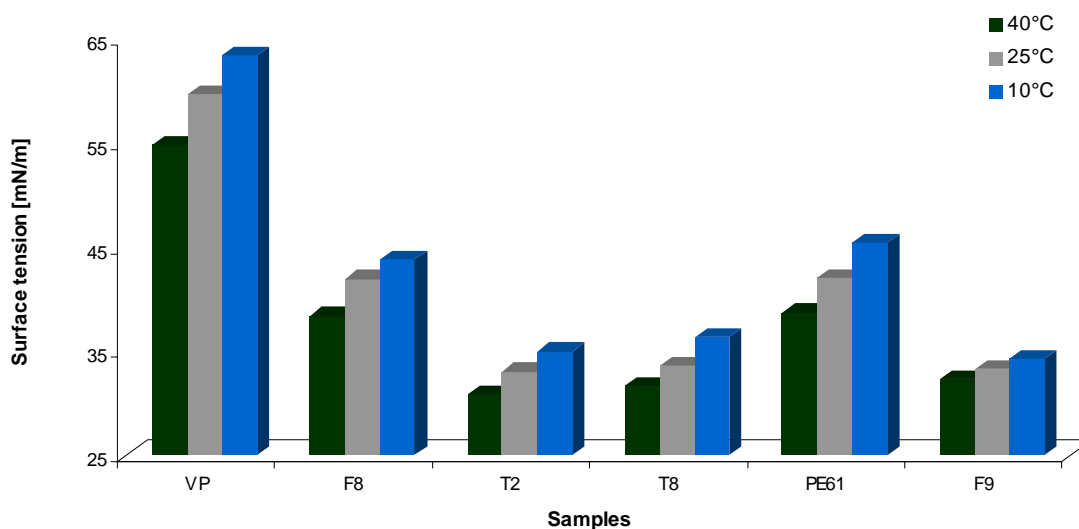

Figure 2.6: Surface tensions of VSN (PVP-Surfactant-NI) solutions measured at 10, 25, and 40 °C, respectively.

2.3.3 Viscosities and densities of PS and PSN solutions

The viscosities and densities of PS and PSN solutions are measured at 25 °C and 40 °C. The detailed data of PS solutions (P3 used in solutions) are shown in Figure 2.7. The viscosities of all samples are approximately 165 mPas at 25 °C and 100 mPas at 40 °C, respectively. Although viscosities of various pure surfactants are quite different, only 1 wt% concentration of surfactants in solutions does not influence the viscosity values of the PS solutions significantly. When 2.2 wt% F8 is used in the P3-surfactant solution (the second two columns in Figure 2.7), the viscosity is larger compared to the other samples indicating that the viscosity increases with increasing surfactant concentration.
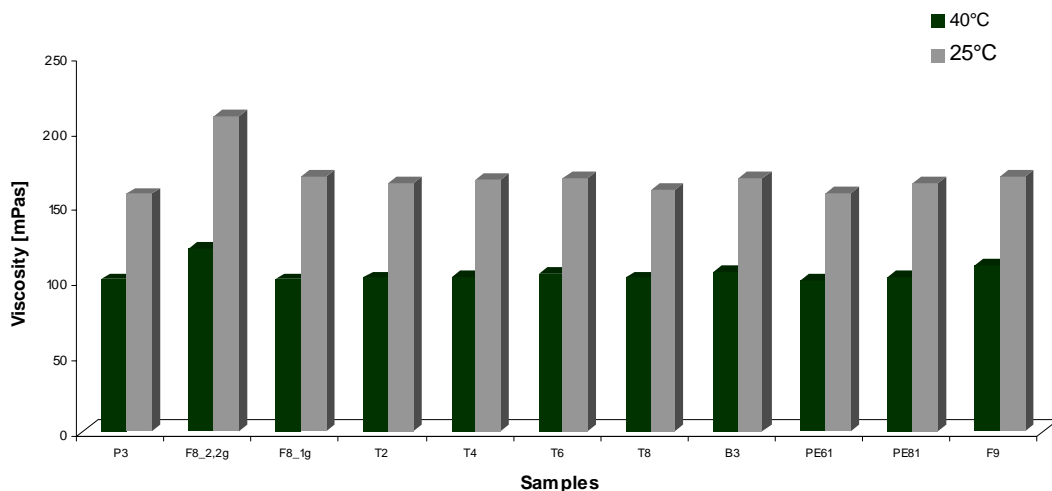
Figure 2.7: Viscosities of P3-Surfactant solutions measured at 25 and 40 °C.

When NI is added in the PVA-surfactant solutions, the viscosities of all solutions decrease and reach 90 mPas at 25 °C and 55 mPas at 40 °C. The dissolution of NI in the PVA solutions destroys the hydrogen bonds between PVA and water, thus lowering the viscosity. This phenomenon has already been observed by Zourab.[97] Furthermore, it can be observed that various surfactants do not influence the viscosity values of these solutions since only 1 wt% of surfactants are used in the solutions. Numerous reports of Griffiths et al. have discussed the influence of the concentration of surfactants on the rheological properties of the solution systems.[98,99,100] The values are shown in Figure 2.8.
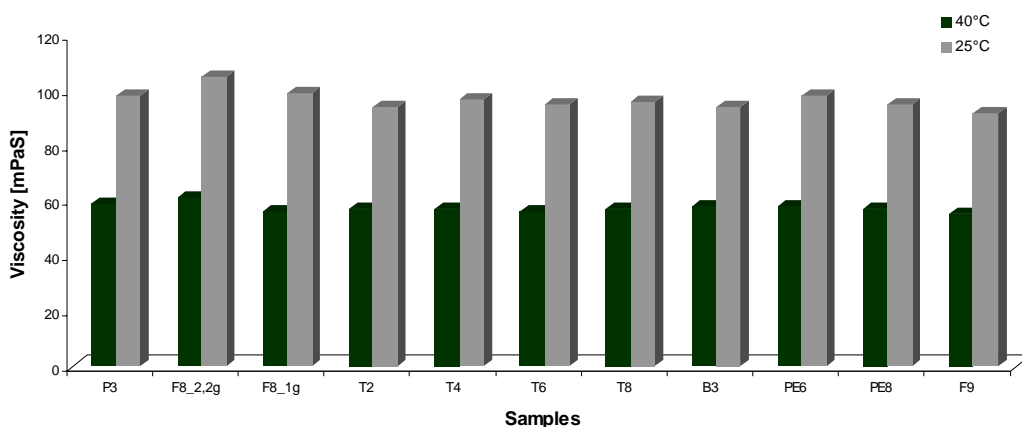

Figure 2.8: Viscosities of P3-Surfactant-NI solutions measured at 25 and 40 °C.

Normally, the viscosity behavior of polymer solutions is that of typical non-Newtonian fluids, i.e. the viscosity of the solution changes with increasing shear rates. However, all PS and PSN solutions show almost Newtonian behavior in this study. The viscosity values do not change

27

with increasing shear rates during experiments. For instance, the viscosity as a function of frequency plot of the P3-T2-NI solution is shown in Figure 2.9.
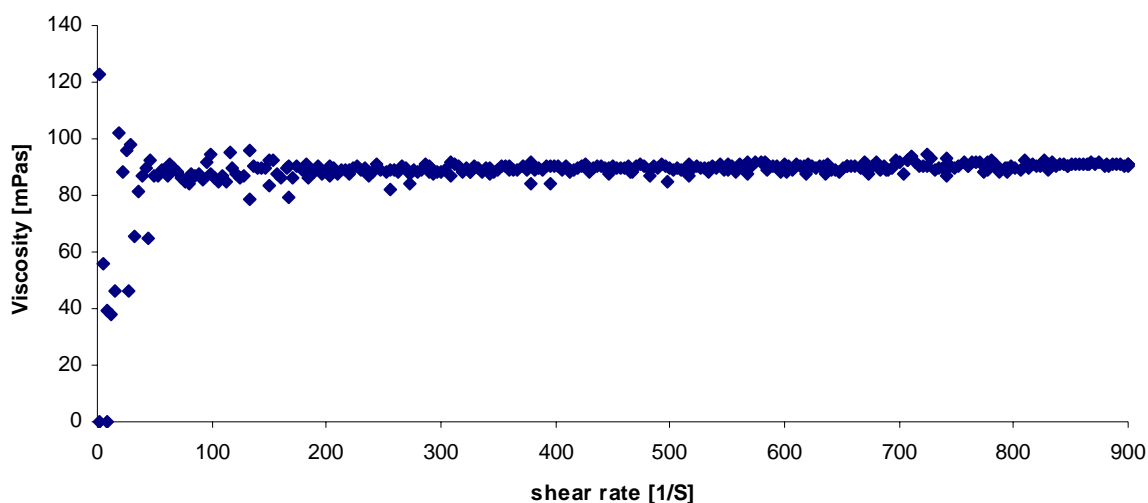

Figure 2.9: Viscosity of P3-T2-NI solution as a function of shear rate measured at 25°C.

When the shear rate increased, the viscosity of the P3-T2-NI solution keeps constant value at ~90 mPas. This phenomenon can be observed for all other PS and PSN solutions, i.e. they have Newtonian behavior. In general, for the PVA solution, this behavior depends on the degree of polymerization (molar mass), concentration of the solution and storage time.[45] The entanglement molar mass of PVA is around 3750 g/mol.[101] This value is smaller than the molar mass of the PVA used in solutions (~8000-10000 g/mol). Thus, entangled PVA chains are in the solutions. But Ŝtern has reported a Newtonian behavior of a PVA solution when the molar mass of PVA is around 10000 g/mol in a freshly prepared solution.[45] After several days of storage, some super-molecular structures can form, the so called physical aging.[44] Meanwhile, the particle size becomes larger which may result in non-Newtonian behavior of the solution system.

Densities of PS and PSN solutions are measured at 25 °C and 40 °C. Figure 2.10 shows the densities of PS solutions. The densities of PS solutions are approximately 1.034 g/cm^3 at 40 °C and 1.04 g/cm^3 at 25 °C. With increasing temperature, the densities decrease due to the expansion of liquid volume having the same mass. Although densities of pure surfactants are different, only 1 wt% concentration of surfactants does not influence densities of PS solutions strongly.

When NI is added in PVA-surfactant solutions, the densities of all solutions increase and reach 1.104 g/cm^3 at 25 °C and 1.092 g/cm^3 at 40 °C. The similar phenomenon can be

observed that various surfactants do not influence the density values of these solutions since only 1 wt% of surfactants is added. The density values are summarized in Figure 2.11.
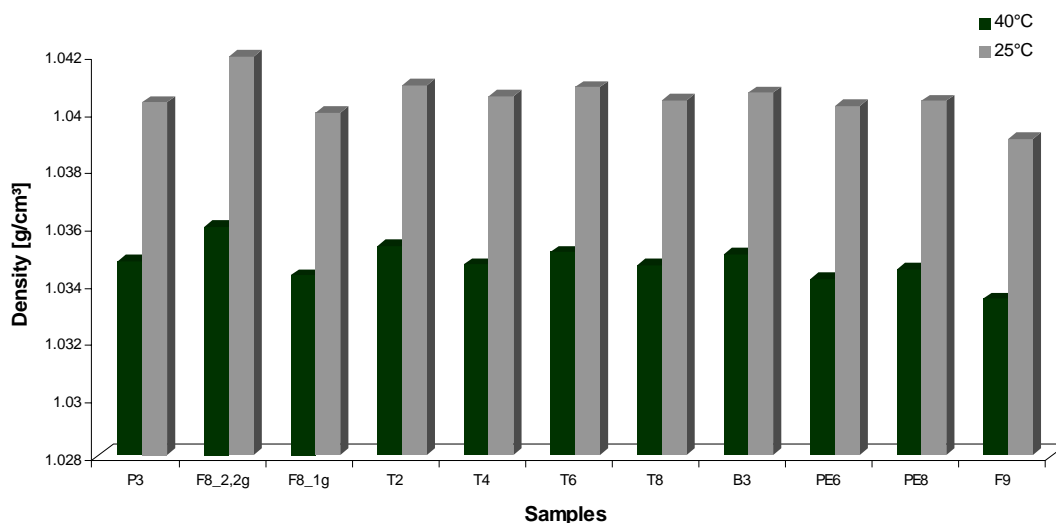
Figure 2.10: Densities of P3-Surfactant solutions measured at 25 and 40 °C.
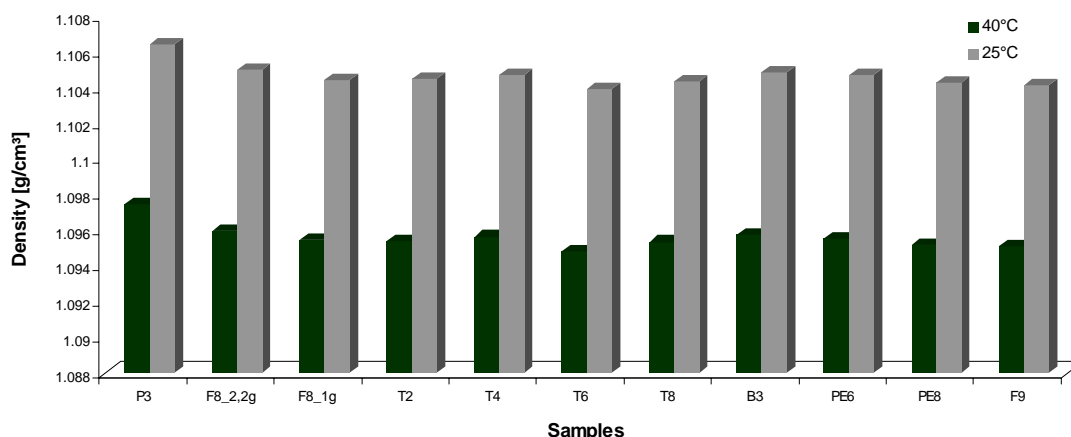
Figure 2.11: Densities of P3-Surfactant-NI solutions measured at 25 and 40 °C.

2.4   Conclusions

Poly(vinyl alcohol) and surfactant, two main constituents in surface active anti-caking agents, are characterized by various methods. CMC values of surfactants are measured at 10, 25 and 40 °C with the aid of surface tension measurements using the Wilhelmy plate method. PE6, PE8, and F8 have the CMC values in the range of 10^{-7} mol/l. T series product and F9 have the CMC values in the range of 10^{-6} mol/l. CMC values of T series products show that the CMC decreases with increasing the number of carbon atoms of the alkyl chain when the surfactant

has the same hydrophilic group due to a stronger repulsion between the hydrophobic block of the surfactant and water. The temperature-dependent CMC values of surfactants are used to obtain their thermodynamic properties. The CMC values of T8 have the smallest change as a function of temperature, i.e. its surface activity is most stable at various temperatures. The surface tensions of PS and PSN solutions are measured at 10, 25 and 40 °C using the Wilhelmy plate method. The solutions with T2 or T8 have the lowest values of ~ 29 mN/m at 40 °C, 32 mN/m at 25 °C, 35 mN/m at 10 °C although NI is added to the solutions. In the F8, B3, PE6 and PE8 containing solutions, surface tensions increase when NI is added to the solutions. This is caused by the fact that hydrogen bonds are formed between NI and water leading to dehydration of hydrophilic block of the surfactant and water. The micelle formation is preferred and the surface activity of surfactants is reduced. Viscosities of PS and PSN solutions are measured at 25 and 40 °C. Although the viscosities of various pure surfactants are different, only 1 wt% concentration of surfactants in solutions does not influence the viscosity values of PS and PSN solutions significantly. Furthermore, Newtonian behavior of the anti-caking solutions can be observed due to the application of low molar mass PVA in the solution. This behavior is different from common polymer solutions or melts. Similarly, densities of PS and PST solutions are measured also at 25 and 40 °C. Various surfactants in the solutions do not influence the density values of PS and PST solutions significantly.

Chapter 3

Investigation of fertilizer granules coated with anti-caking agents

3.1   Introduction

The main mechanism of fertilizer particles caking is the so called salt bridge formation.[16] A popular and low-cost method to prevent the caking of fertilizer particles is the application of anti-caking agents. The effects of anti-caking agents can be tested after they are coated on the fertilizer surface. Generally, the test process is mainly divided into two steps. Firstly, fertilizer granules, powders or prills, which are already coated with anti-caking agents, are allowed to be caked under defined conditions in special equipment. Various apparatuses are used in order to study the agglomeration process of the coated fertilizers, e.g. double particle system,[102] multi-particle system,[103] etc. The influencing external factors, e.g. temperature, humidity, load on the fertilizers and storage time are adjusted to cake coated fertilizers.[16] Secondly, after the caking of fertilizers, the effect of anti-caking agents is determined by detecting the maximum force or load which can destroy the lump. Normally, various mechanical tests are carried out, such as tensile tests,[17,104,104] compression tests,[105,106,107] and centrifuge tests.[108] By comparing the destroy loads for de-caking by the tensile test or mass of still caked granules after free falling lump test followed by the calculation of anti-caking ratio, the anti-caking effect of the agents could be known.

In this chapter, the coating process of fertilizer granules was described. Coated granules are stored in the double particle system and the multi-particle system under different conditions, e.g. temperature, humidity, loads etc. Karl Fischer titration (KFT) is carried out to measure the water content of uncoated and coated granules. The modified mechanical tests in lab scale, i.e. tensile test and free falling lump test are designed to detect the effects of anti-caking agents. Caked granules are visualized by light microscopy and scanning electron microscopy. The caking phenomenon between granules caked and the metal plate (the production line in industry) is discussed. All anti-caking agents used are described in the chapter 2.

3.2   Experimental section

3.2.1   Materials

Preparations of PVA-PVP-Surfactant-NI (PVSN) solutions

Besides the PS, PSN and VSN anti-caking solutions, PVA-PVP-Surfactant-NI (PVSN) solutions were also prepared. Different mass ratios of PVA and PVP were prepared in solutions, including ratios of PVA to PVP of 50:50, 60:40, 70:30 and 80:20. The detailed compositions are listed in Table 3.1. At first, PVA and 0.75 g surfactant were added to double distilled water and they were placed in an oven at 95 °C for 4 h. Then, the solutions were taken out from the oven and mixed using a stir bar until the solution was homogenous. When the temperature of the solutions decreased to the room temperature, PVP and 24.375 g NI were added to solutions and stirred until complete dissolution. The PVA used in PVSN solutions is P98.

Table 3.1: Compositions of PVA-PVP-Surfactant-NI solutions.

PVA : PVP	PVA [g]	PVP [g]	Surfactant [g]	NI [g]	Water [g]
50 : 50	4.25	4.25	0.75	24.375	41
60 : 40	5.1	3.4	0.75	24.375	41
70 : 30	5.95	2.55	0.75	24.375	41
80 : 20	6.8	1.7	0.75	24.375	41

3.2.2 Coating experiment

The coating processes were done by 4 steps. At first, 100 g fertilizer granules were put into a glass bottle and the bottle was sealed and shaken for 5 min using a shake machine (Heidolph REAX 2) for obtaining free-flow of every granules. Secondly, the bottle was opened and placed in the drying oven at 45 °C for 3 h to evaporate the water content in the granules which was absorbed during the storage. Thirdly, after a bottle of granules was taken out from the drying oven, 0.3 g anti-caking solution was added to fertilizer granules and sealed the bottle. Immediately after, the bottle was shaken with the shake machine for 5 min again in order to obtain the homogenous coating of anti-caking solution on the surface of every granule. At last, the bottle was opened and placed in the drying oven at 40 °C for 2 h to evaporate water content of the agents. At this moment, the whole coating procedures were finished. The coated granules were stored in the glass bottle for initial water content measurements and mechanical tests, etc.

3.2.3 Karl Fischer titration

The water contents of fertilizer granules before and after coating were measured using Karl Fischer titration (Mettler DL35). The titration is based on the oxidation of sulphur dioxide by

iodine in the presence of water. Methanol is the most commonly used solvent. The Karl Fischer titration (KFT) can be described by two following reactions:

$$CH_3OH + SO_2 + RN \rightarrow [RNH]SO_3CH_3 \qquad (3.1)$$

$$H_2O + I_2 + [RNH]SO_3CH_3 + RN \rightarrow [RNH]SO_4CH_3 + 2[RNH]I \qquad (3.2)$$

RN designates the base used.

The Karl Fischer reaction can only take place in a certain pH range between 5 and 7. In this pH range, the reaction remains constant.[109] If the pH drops too low, end point attainment becomes sluggish or and end point will not be reached at all. If the pH is too high, side reactions occur making the titration non-stoichiometric. In this study, 2 g granules were required at every measurement and the solvent was methanol.

3.2.4 Caking experiment

After fertilizer granules were coated by different anti-caking agents, they were stored in the double particle system and multi-particle system (Figure 3.1a and b). For double-particle system (DPS), two granules were stored in the glass tube and pressured by a load. The required load can be calculated by the adapted equation of Rumpf:[110]

$$\sigma = \frac{1-\varepsilon}{\varepsilon} \cdot \frac{F_H}{x_d^{\,2}} \qquad (3.3)$$

where F_H is adhesive force, x_d is particle diameter, ε is porosity and σ is the tensile strength in the bulk.

In order to obtain the caked granules, DPS was stored under two different conditions. In the first case, it was placed in the climate chamber for 3 days. For partial dissolution of the surface of granules to form the liquid bridges, the temperature and relative humidity were controlled at 25 °C and 85%, respectively. In addition, 50 g load was applied on the double-granule (see Figure 3.1a). After 3 days of storage in the climate chamber, the relative humidity was changed to 30 % for another 2 days for the drying of the liquid bridges allowing them to re-crystallize for the formation of the salt bridge. The temperature in the climate chamber was still kept constant at 25 °C during the drying. In another case, firstly, DPS was stored under more unfriendly conditions of 40 °C and 75 % relative humidity for 3 days to

obtain a more extensive dissolution of the surface of granules. The load was kept at 50 g. After storage for 3 days, the temperature and relative humidity were changed to 25 °C and 30 % for 2 days to form harder salt bridges due to re-crystallization.
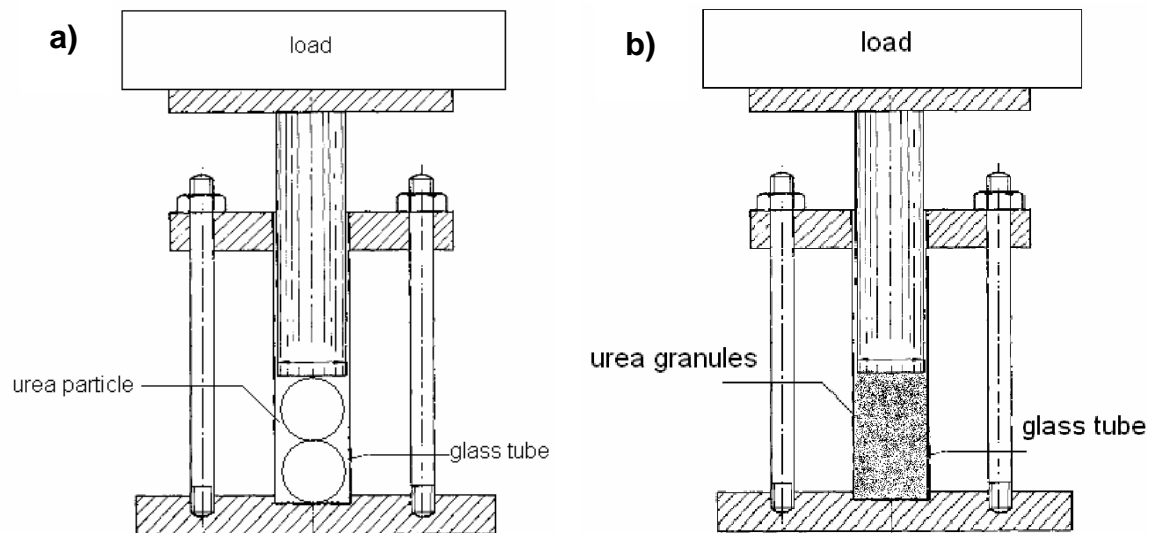

Figure 3.1: Double particle system (a) and Multi-particle system (b).

For the multi-particle system (MPS), 4 g fertilizer granules were stored in the glass tube and exerted to a load of 1 kg. The storage condition was similar to the DPS system; two different cases were addressed. For the first case, the MPS was placed in the climate chamber for 3 days at a temperature and relative humidity of 25 °C and 85%, respectively. In addition, 1 kg load was applied on 4 g granules. After the storage of 3 days in climate chamber, the relative humidity was changed to 30 % for another 2 days for drying and the formation of crystal bridges between granules. The temperature in the climate chamber was kept at 25 °C. For a second case, MPS was stored at 40 °C and 75 % relative humidity for 3 days under the load of 1 kg. The caked lumps of granules with harder salt bridges were obtained after an additional storage at 25 °C and 30 % relative humidity for another 2 days.

3.2.5   Mechanical tests for caked fertilizer granules

Fertilizer granules were caked after they were stored in the climatic chamber with DPS and MPS. The modified mechanical tests, tensile test and free falling lump test were carried out on the caked granules to investigate anti-caking effects of coating solutions. To DPS in this study, two caked fertilizer granules were measured by tensile tests to determine the maximum destroying loads for de-caking caked granules (breaking the crystal bridge formed during the caking experiments). The experimental procedures and setup are shown in Figure 3.2a-c.

At first, two caked granules were caught by two clamps, one of which was connected with a small container (blue bowl) for holding the lead balls (Figure 3.2a). And then, the lead balls were added into the blue container step by step (Figure 3.2b). When enough lead balls were put into the holder, the caked granules were broken (Figure 3.2c). The mass of these lead balls was weighted as the maximum destroying loads.
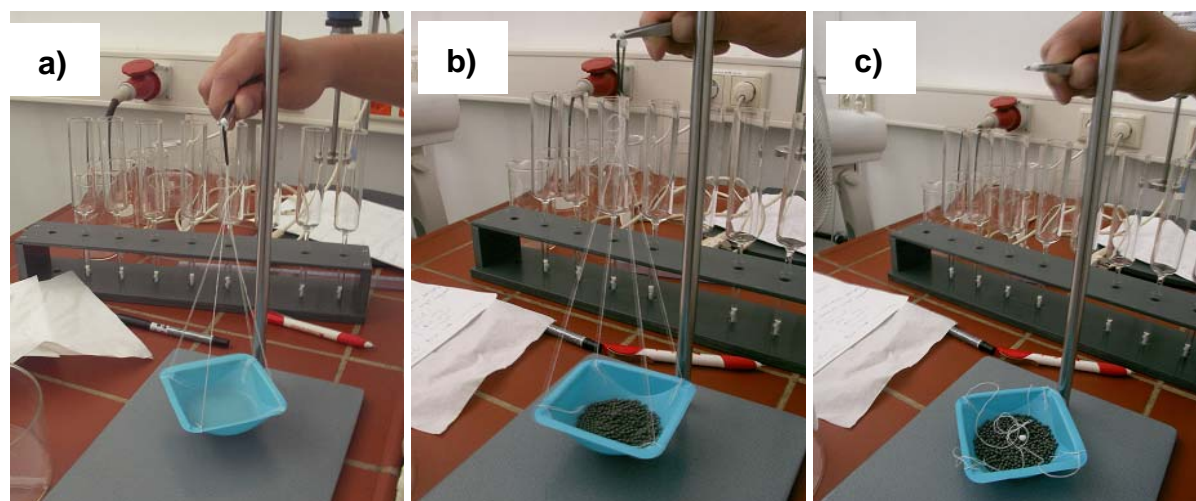
Figure 3.2: The procedures of modified tensile tests for caked granules from DPS.

When the granules were caked by MPS, the free falling lump tests were carried out on the multi-granules species to measure the anti-caking efficiency. The designed free falling lump test is an indirect test to measure the caking of fertilizers in the lab scale. The processes are described as follows. Caked granules (4 g) were free fallen from 1 m height (Figure 3.3a). After the granules fell, the still caked granules (Figure 3.3b) were collected and weighted. Hereby, only single granules were considered to be un-caked. The anti-caking efficiency can be calculated by Equation 3.4.

$$R_{ac} = (b-a)/b \times 100\% \tag{3.4}$$

where, R_{ac} is anti-caking ratio, b is weight of whole caked samples, a is weight of still caked granules after falling.

Figure 3.3: Free falling tests (a) and granules after free falling (b).

3.2.6 Microscopy

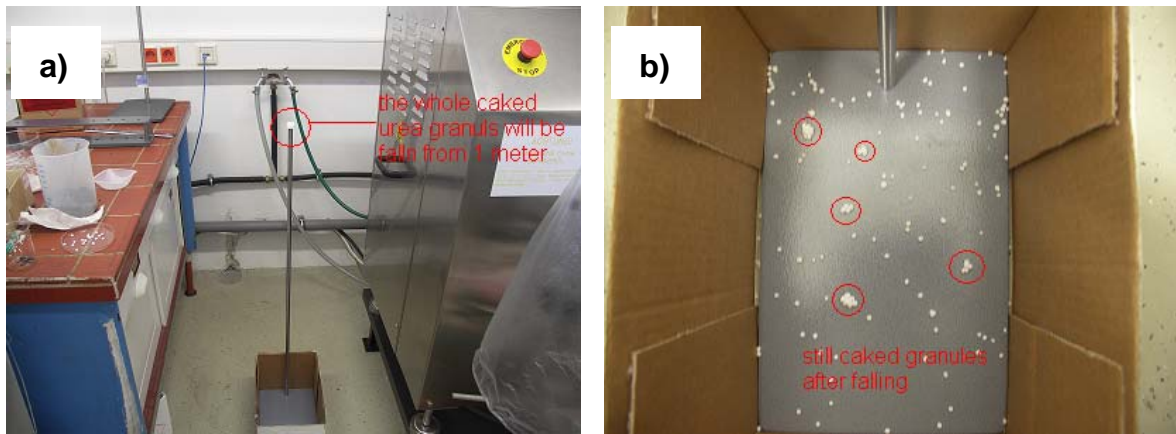A Zeiss Axioplan2 light microscope equipped with Zeiss AxioCam MRC (camera) was used to observe the fertilizer granules before and after caking experiments. The granules were prepared as described in chapter 3.2.4. The salt bridges of these granules before and after tensile tests were also observed by a Philips XL30 Environmental Scanning Electron Microscopy (ESEM) using an acceleration voltage of 10 kV.

3.2.7 Mechanical tests for anti-caking agents coated metal plate

During the manufacture of fertilizer granules, they not only agglomerate, but caked on the waterline production line. This kind of caking comes from the re-crystallization of fertilizers and the adhesion of PVA solutions on the production line. A modified tensile test using Instron 4464 tensile-meter was carried out on the adhesions between two anti-caking solutions coated metal plates. The metal plate is the same material as production line. The experimental procedure is described below. At first, the specimens were prepared by cutting the metal plates into a 'T' shape (Figure 3.4a). Secondly, the coating solutions were placed homogenously on the metal plates (the coating region on the metal plates has a size of 36 mm width times 25 mm length). They were stored in the drying oven at 45 °C for 3 days. This storage temperature is the same as that of granules after coating of anti-caking solutions. It allows the evaporation of water and the formation of a thin film between metal plates. After drying (Figure 3.4b), the tensile tests were used to measure the separation loads (adhesion) for separating the solution coated plates after drying.
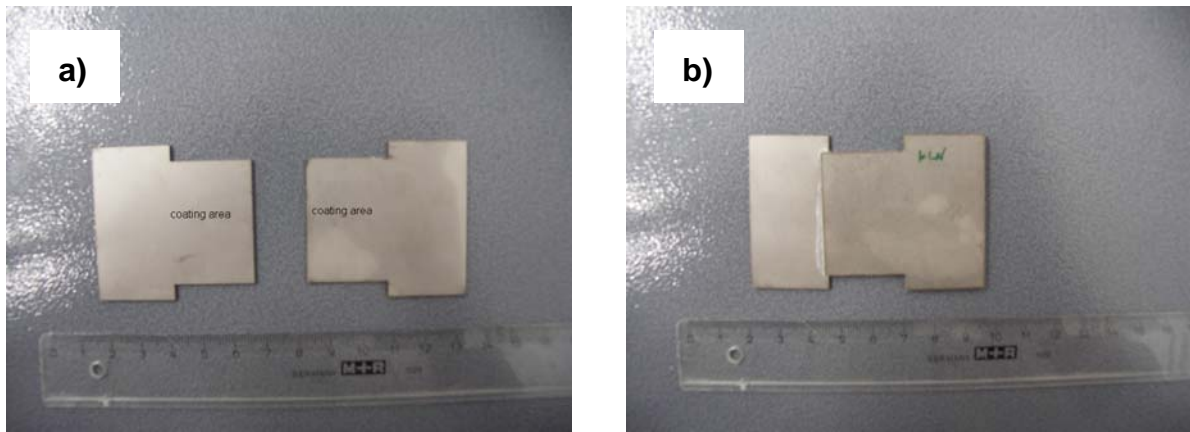
Figure 3.4: "T" shape metal plate (a) and metal plates after coating and drying (b).

When metal plates (after coating and drying) were installed in the clamps of tensile machine, two caked metal plates were separated (destroyed) before tests (Figure 3.5a and b) due to the tensile force of caked plates was so strong, compared with their very low bending force. When the plates were installed in the clamps of tensile machine, the unfixed clamps created an unwanted bending force on plates and separated them.
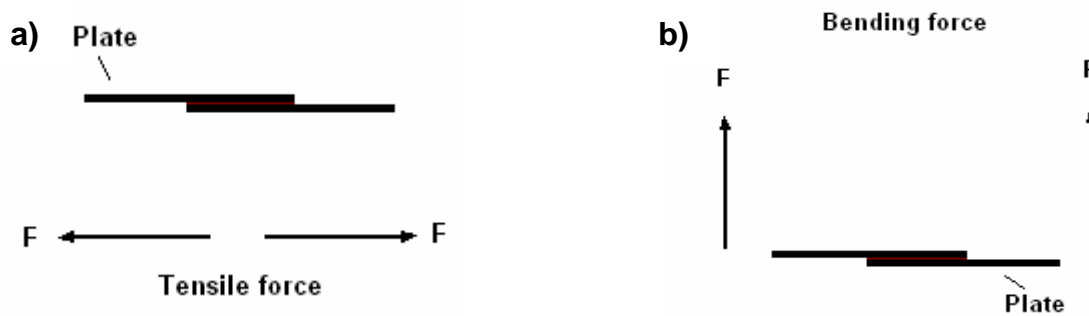
Figure 3.5: Tensile force on plates (a) and bending force on plates (b).

Therefore, tensile tests of caked plates were optimized by making a hole through the uncoated area of the metal plate. After coating and drying of the plates, the caked sample plates were connected with another uncoated plate by a strand (See Figure 3.6a). Hence, when this sample was installed in the clamps of the tensile machine, the bending force between caked plates was avoided (see Figure 3.6b).
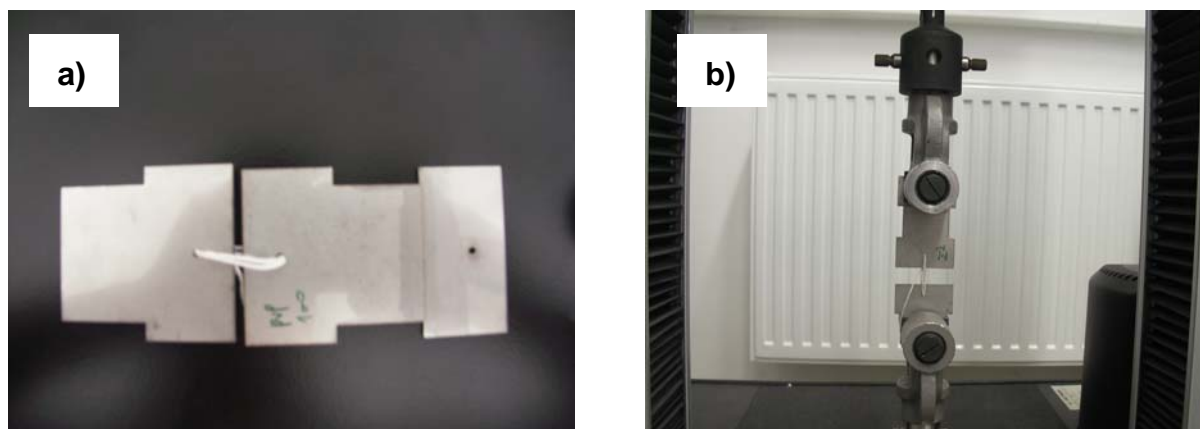
Figure 3.6: Plates were connected by a strand (a) and plates were caught by clamps in the tensile machine (b).

3.3 Results and discussion

3.3.1 Water content measurements

KFT is used to measure the water contents of granules during entire process of coating experiments. Before coating, the water content of 2 g uncoated urea granules is measured at room temperature and the value of 898 ± 25 ppm is obtained. Then, uncoated granules are shaken for 5 min and dried for 3 h in the oven at 45 °C, the water content of dried uncoated granules is measured at room temperature about 787 ± 15 ppm. There is approximately a 110 ppm decrease compared with granules before drying. Finally, granules are coated with different anti-caking solutions (e.g. PVA-F8-NI, P3-T2-NI, P3-T8-NI and P3-PE6-NI etc.). After drying at 40 °C for 2 h, these granules are stored in the glass bottle for 2 days at the room temperature. KFT is applied again to measure the water content of coated granules. Values are listed in the Table 3.2.

Table 3.2: Water contents of granules coated with anti-caking agents.

Coating solution	PVA-F8-NI	P3-T2-NI	P3-T8-NI	P3-PE6-NI
Water content [ppm]	934 ± 10	841 ± 9	837 ± 25	885 ± 15

From Table 3.2, the water content of granules coated with F8-anti-caking solution is obtained approximately 934 ppm. However, it is obvious that the granules coated with T2- or T8-anti-caking solution have lower initial water contents (~ 100 ppm decrease) due to they have smaller HLB values reflecting more hydrophobic properties. Furthermore, these lower initial water contents lead to less caking tendencies.[18]

3.3.2 Mechanical tests for caked granules

Fertilizer granules are coated with different anti-caking solutions and stored under different conditions in DPS and MPS (Figure 3.7a and b). Granules with diameters from 4 to 4.5 mm are chosen to be stored in the DPS and measured by tensile tests in order to minimize the experimental error of destroying loads.[17,18] For each anti-caking solution, 9 samples are measured to obtain an average value. From MPS, caked granules are measured by free falling lump tests to obtain the mass of still caked granules after falling follow by the calculation of the anti-caking ratio. For each anti-caking solution, an average value is obtained by measuring 5 samples.
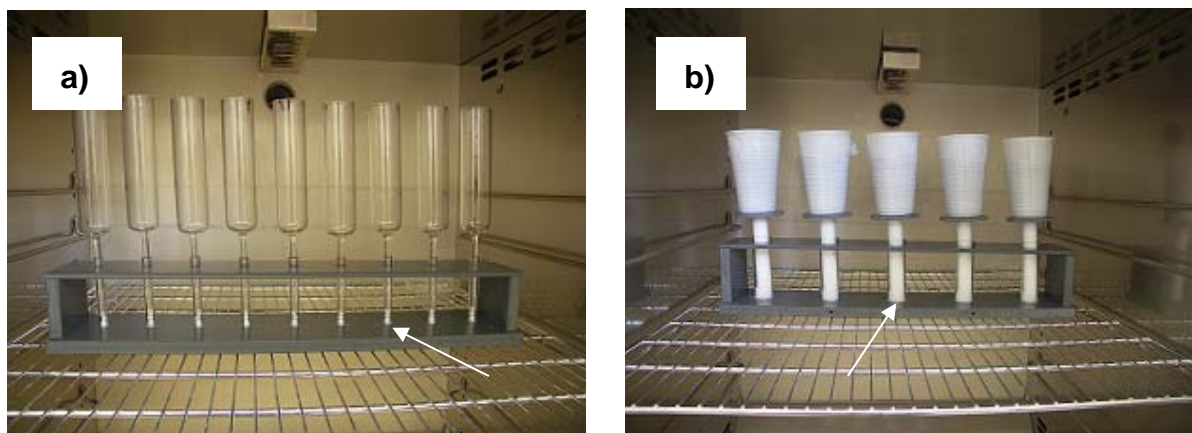
Figure 3.7: Double particle system (a), two granules are stored in the glass tube indicated by arrow and multi-particle system (b), 4 g granules are stored in the glass tube indicated by arrow.

Table 3.3 shows the results of tensile loads of caked double-granules coated with P3-Surfactant-NI solutions stored at 25 °C and 85 % relative humidity. It is obvious that the caked double-granules which are coated with P3-T8-NI have the smallest average destroying loads for de-caking reflecting the smallest caking tendency. Distributions of destroying loads are approximately 0.25 N. However, for granules coated with P3-F8-NI, the destroying load is markedly higher than samples where P3-T8-NI and P3-T2-NI are used, which is around 1.5 N. When double-granules are stored in the climate chamber at the relative humidity of 85 %, parts of granule surface are dissolved and the liquid bridges can be observed. Depending on the surface tension measurements at 25 °C, the values of P3-T8-NI and P3-T2-NI are approximately 5 mN/m smaller than that of P3-F8-NI. Thus, using equation 2.6, capillary adhesive force of P3-F8-NI anti-caking solution is ~ 10 mN larger than that of P3-T2-NI and P3-T8-NI leading to a harder salt bridge formation between granules during caking experiments.

Table 3.3: Maximum destroying loads after granules stored at 25 °C, 85% relative humidity for 3 days.

Granules coated with P3-F8-NI	Sample 1	Sample 2	Sample 3	Sample 4	Sample 5	Sample 6	Sample 7	Sample 8	Sample 9	Average value
Load of destroy the caked particles [g]	112.66	196.44	138.61	41.01	96.69	181.8	167.72	152.12	252.13	148 ± 57
Tensile force [N]	1.104	1.925	1.358	0.402	0.948	1.781	1.644	1.491	2.471	1,458 ± 0,567

Granules coated with P3-T2-NI	Sample 1	Sample 2	Sample 3	Sample 4	Sample 5	Sample 6	Sample 7	Sample 8	Sample 9	Average value
Load of destroy the caked particles [g]	50.25	54.33	60.99	17.67	23.68	63.37	21.68	14.91	2.66	34 ± 21
Tensile force [N]	0.492	0.532	0.597	0.173	0.232	0.621	0.212	0.146	0.026	0,336 ± 0,21

Granules coated with P3-T8-NI	Sample 1	Sample 2	Sample 3	Sample 4	Sample 5	Sample 6	Sample 7	Sample 8	Sample 9	Average value
Load of destroy the caked particles [g]	2.66	16.11	51.19	38.36	16.42	14.68	2.66	58.04	27.61	25 ± 18
Tensile force [N]	0.026	0.158	0.502	0.376	0.161	0.146	0.026	0.569	0.271	0,24 ± 0,18

Granules coated with P3-PE6-NI	Sample 1	Sample 2	Sample 3	Sample 4	Sample 5	Sample 6	Sample 7	Sample 8	Sample 9	Average value
Load of destroy the caked particles [g]	192.36	150.33	15.25	26.86	158.39	2.66	154.32	182.52	168.57	116 ± 73
Tensile force [N]	1.885	1.473	0.149	0.263	1.522	0.026	1.512	1.789	1.652	1,141 ± 0,717

Granules coated with P3-F9-NI	Sample 1	Sample 2	Sample 3	Sample 4	Sample 5	Sample 6	Sample 7	Sample 8	Sample 9	Average value
Load of destroy the caked particles [g]	103.12	32.35	133.09	72.73	27.29	2.66	95.85	13.75	137.44	69 ± 49
Tensile force [N]	1.011	0.317	1.304	0.713	0.267	0.026	0.94	0.135	1.35	0,673 ± 0,48

The destroying loads of granules coated with PSN solutions by tensile tests are listed in Table 3.4.

Table 3.4: Destroying loads of granules coated with various PSN after storage of 3 days at 25 °C, 85% relative humidity.

Samples	25 °C, 85 % humidity [g]	40°C, 75 % humidity [g]
P1-T8-NI	46 ± 54	155 ± 98
P1-T2-NI	93 ± 90	144 ± 68
P98-T8-NI	38 ± 38	114 ± 71
P98-T2-NI	36 ± 33	144 ± 63
P01-T8-NI	40 ± 50	161 ± 82
P01-T2-NI	75 ± 80	155 ± 75
P80-T8-NI	23 ± 27	122 ± 64
P80-T2-NI	28 ± 26	133 ± 45
P81-T8-NI	30 ± 48	158 ± 61
P81-T2-NI	38 ± 47	140 ± 37
P03-T8-NI	28 ± 37	131 ± 61
P03-T2-NI	31 ± 35	130 ± 58
P37-T8-NI	33 ± 28	118 ± 35
PA99-T8-NI	28 ± 27	55 ± 22
PA98-T8-NI	31 ± 21	67 ± 35
P115-T8-NI	33 ± 24	71 ± 25
P116-T8-NI	31 ± 38	138 ± 48
P129-T8-NI	36 ± 32	133 ± 36
P130-T8-NI	38 ± 42	110 ± 41
P131-T8-NI	35 ± 37	89 ± 43

As can be seen in Table 3.4, when coated granules are stored at 25 °C and 85 % relative humidity, the destroying load values of tensile tests are smaller compared to data obtained after storage at 40 °C and 75 % relative humidity. This is caused by the fact that the critical relative humidity of the granule significantly decreases with increase of temperature indicating the water-uptake of granules is much larger under the condition of the high temperature.[17] Thus, the caking is significantly influenced by different factors, such as the morphology of granule, the coating thickness and the size of granules. Values of destroying loads obtained under the condition of 25 °C and 85 % relative humidity show a large scattering, even though 9 samples are measured for each coating solution. But the tendency of caking of granules coated with various agents could be compared. However, after the worse storage condition, i.e. 40 °C and 75 % relative humidity, the anti-caking effects of solutions are easier to be compared because of the smaller scattering of average destroying loads values of tensile tests. Coating solutions of T8 and PVA with high hydrolysis degrees (HD have more optimum anti-caking abilities in term of destroying load values compared to PA99-T8-NI, PA98-T8-NI and P115-T8-NI. There could be two reasons for such an improvement of the anti-caking behavior. At first, high HD PVA is more difficult to be dissolved in water due to a large amount of inter- and intra-molecular hydrogen bonding of PVA macromolecules. Secondly, with the increase of hydrolysis degree, it might be easier for PVA to form the complex with surfactants leading to the synergistic effect.[111,30,32] The tendency of destroying load values of tensile tests with different hydrolysis degrees of PVA is shown in Figure 3.8. Coating solutions of PA98-T8-NI, P37-T8-NI, P80-T8-NI and P116-T8-NI are chosen for analyses. In these solutions, different hydrolysis degrees of PVA are used and the relationship between the destroying load of caked double-granules and the hydrolysis degree are studied. In brief, when the higher hydrolysis degree of PVA is used, a smaller destroying load can be measured. Furthermore, a decrease of destroying load fitting with a polynomial function can be observed within the increase of the hydrolysis degree of PVA used in the anti-caking solution.

The chart shows the equation:

$$y = -0.0858x^2 + 0.6414x + 0.1298$$
$$R^2 = 0.9386$$

With y-axis labeled "Destroying loads of PSN coated granules after tensile test [N]" ranging from 0 to 1.6, and x-axis labeled "Hydrolysis degree of PVA %" with values 98, 96, 88, 80.
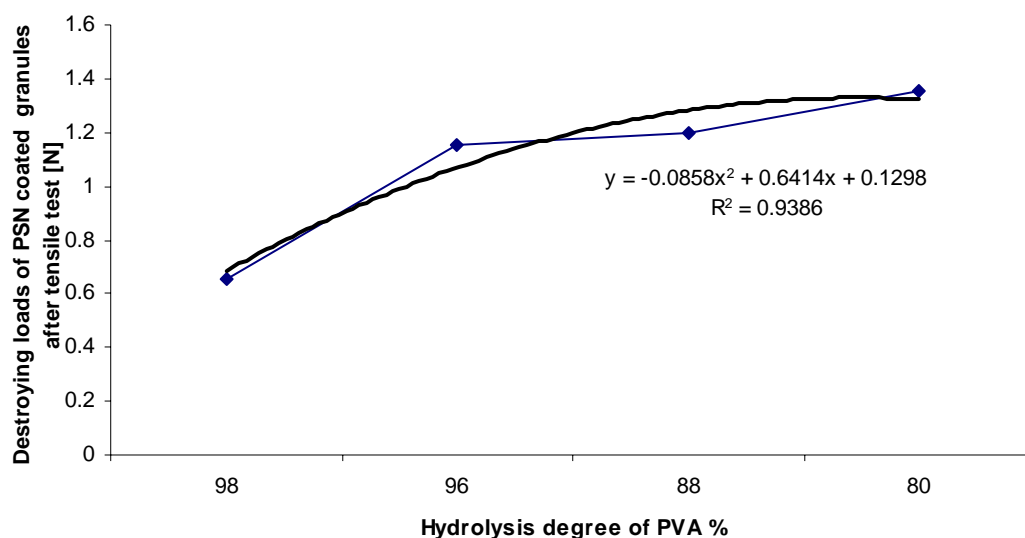
Figure 3.8: Destroying loads of caked double granules vs. hydrolysis degrees of PVA used in the anti-caking solution.

Fertilizer granules are also coated by VSN and PVSN solutions, which included another water soluble polymer of PVP. Preparations of VSN and PVSN solutions are already described in 3.2.1. These coated granules are subjected to the same conditions as PSN coated granules. Mechanical tests are done to measure anti-caking effects of these coating solutions. The destroying loads of VSN and PVSN coated granules measured by tensile tests are listed in Table 3.5.

Table 3.5: Destroying loads of various VSN and PVSN coated granules after storage of 3 days at two different temperatures and relative humidity.

Sample	25 °C, 85 % humidity [g]	40 °C, 75 % humidity [g]
P98-PVP-T8-NI (80:20)	23 ± 23	132 ± 72
P98-PVP-T8-NI (70:30)	41 ± 27	138 ± 38
P98-PVP-T8-NI (60:40)	51 ± 37	136 ± 51
P98-PVP-T8-NI (50:50)	50 ± 39	139 ± 31
PVP-T8-NI (0:100)	38 ± 32	127 ± 48

The destroying loads of PVSN coated granules are similar as PSN (P98) coated granules, i.e. PVP does not markedly change the values of destroying load indicating that PVP has weak interaction with the surfactant and PVA in the solution. Compared with all PSN coated granules, anti-caking effects of PVSN coated granules are moderate.

Figure 3.9 a and b show the side views of granules coated with F8- and T8-coating solutions stored in the MPS. Caked granules are formed in the 2 cm (diameter of bottom area) × 2 cm

(height) cylinder. After caked fertilizer granules are taken from the MPS, top and side view are shown in Figure 3.10 a and b.

Figure 3.9: Granules coated with F8-coating solution (a) and T8-coating solution (b) in MPS.

Figure 3.10: Top view of caked granules (a) and side view of caked granules from MPS (b).

It is obvious that granules coated with F8-coating solution have serious re-crystallization behavior. When granules are stored in the climatic chamber at the high humidity and temperature, many parts of granules are dissolved due to the higher capillary adhesive force between granules (more water contents are absorbed from the environment). But granules coated with T8-coating solution have a higher hydrophobic property leading to less water-uptake behavior thus weak re-crystallization behavior.

These caked granules were then used for the free fall test from 1 m height. After falling, still caked granules are collected (see Figure 3.11) and weighted to calculate the anti-caking ratio.

Figure 3.11: Still caked granules after falling from 1 m height (only single granule was

considered as un-caked).

Using Equation 3.4, the anti-caking ratios of granules coated with various anti-caking solutions and stored at 25 °C and 85 % relative humidity for 3 days are listed in Table 3.6. For each anti-caking solution, there are 5 samples of coated granules prepared and measured with the free falling lump tests. From Table 3.6 it can be seen that granules coated with T2- and T8-solutions do not show any caking after they are fallen from 1 m height. All granules found are single particles after the free falling lump test. To granules coated with F8-coating solution, after falling from 1 m height, 2 of whole five samples are un-caked, i.e. only single granules are observed and collected. For the other 3 samples, the anti-caking ratios (calculated using Equation3.4) were 55%, 71% and 69%, respectively. This is agreement with the formation of stronger salt bridge shown in Figure 3.9a indicating that many parts of the granules are dissolved during storage in climate chamber and hard solid bridges are formed. However, after the free falling lump test granules coated with the T8-solution are not caked (after they are stored at 25 °C and 85% relative humidity for 3 days in MPS) reflecting an anti-caking ratio of 100%. In order to obtain the optimum values of the anti-caking ratio, the condition of 40 °C and 75% relative humidity are used. Since the caking effects are strong under these conditions, it is easy to obtain detectable differences. The strength of the salt bridge shows comparable characteristics with increasing temperature. The results are listed in Table 3.7.

Table 3.6: Anti-caking rates of granules coated with various anti-caking solutions stored at 25 °C and 85 % relative humidity for 3 days.

Granules coated with PVA-F8-NI	Sample 1	Sample 2	Sample 3	Sample 4	Sample 5
still caked granules after falling	1,82g	1,16g	NC	NC	1,25g
anti-caking rate	55%	69%			71%

Granules coated with P3-T2-NI	Sample 1	Sample 2	Sample 3	Sample 4	Sample 5
still caked granules after caking	NC	NC	NC	NC	NC
anti-caking rate					

Granules coated with P3-T8-NI	Sample 1	Sample 2	Sample 3	Sample 4	Sample 5
still caked granules after falling	NC	NC	NC	NC	NC
anti-caking rate					

Granules coated with P3-PE6-NI	Sample 1	Sample 2	Sample 3	Sample 4	Sample 5
still caked granules after falling	NC	1,23g	0,55g	1,19g	1,01g
anti-caking rate		69%	86%	70%	75%

(NC means No Caked, i.e. only single granules are observed after free falling lump test from 1 m height)

Table 3.7: Anti-caking rates of PSN solution coated granules stored at 40 °C 75% relative humidity for 3 days.

Sample	Caked granules after falling [g]	Anti-caking rate
P80-T8-NI	0.988 ± 0.62	75 ± 15%
P81-T8-NI	1.368 ± 0.54	65 ± 13%
P98-T8-NI	0.884 ± 0.29	77 ± 7%
P03-T8-NI	1.07 ± 0.52	73 ± 13%
P01-T8-NI	1.086 ± 0.24	72 ± 6%
P37-T8-NI	1.008 ± 0.28	74 ± 7%
PA99-T8-NI	0.65 ± 0.25	83 ± 6%
PA98-T8-NI	0.66 ± 0.24	83 ± 6%
P115-T8-NI	0.68 ± 0.24	82 ± 6%
P116-T8-NI	1.08 ± 0.28	73 ± 7%
P129-T8-NI	1.07 ± 0.39	73 ± 9%
P130-T8-NI	0.85 ± 0.28	78 ± 7%
P131-T8-NI	0.76 ± 0.3	81 ± 7%

In the Table 3.7, anti-caking ratios of PSN coated granules stored at 40 °C and 75% relative humidity are listed. Each coating sample is measured 5 times in order to minimize the experimental error. The largest anti-caking ratios are obtained by the granules coated with PA99T8-NI, PA98T8-NI and P115-T8-NI, i.e. ~ 83%. On the contrast, the granules coated with P81-T8-NI have the lowest anti-caking ratio. These results also proved the values of the destroying loads obtained by tensile tests, i.e. different hydrolysis degrees of PVA used in the solutions influence the anti-caking effect due to their different solubility behavior in water.

The anti-caking ratios of PVSN coated granules are listed in Table 3.8. From free falling lump tests it can be concluded that the PVSN solutions do not show better anti-caking effects than the PSN solutions. They provided moderate anti-caking ratios of approximately 70 %. Furthermore, anti-caking effects are independent of the ratio between PVA and PVP which is in agreement with the result obtained by the tensile tests.

Table 3.8: Anti-caking rates of PVSN coated granules stored at 40 °C 75 % relative humidity for 3 days.

Sample	Caked granules after falling [g]	Anti-caking rate %
P98-PVP-T80-NI (80:20)	1.108 ± 0.22	72 ± 5
P98-PVP-T80-NI (70:30)	1.138 ± 0.85	65 ± 21
P98-PVP-T80-NI (60:40)	1.262 ± 0.37	68 ± 9
P98-PVP-T80-NI (50:50)	1.12 ± 0.32	72 ± 8
PVP-T80-NI (0:100)	1.15 ± 0.24	64 ± 6

3.3.3 Microscopy study

Light microscopy and ESEM are carried out in order to study the morphology of fertilizer

granules before and after coating experiments. After granules are coated by anti-caking solutions and dried in the oven, the anti-caking agents can be observed on the surface of the granules by ESEM. The surface of fracture area of granules after tensile tests is also observed using ESEM to compare the surfaces of granules coated with various anti-caking solutions. Light microscopy images of double granules coated with F8-and T8-anti-caking solutions are shown in Figure 3.12 a and b. These caked granules are stored at 25 °C and 85 % relative humidity for 3 days and another 2 days for drying at 25 °C and 30 % relative humidity. Solid bridges between the granules can be observed clearly. Granules coated with F8-anti-caking solution show a larger solid bridge, i.e. more than 1 mm in length. However, the solid bridge of granules coated with T8-anti-caking solution is much smaller. This is the reason why the destroying loads from tensile tests of double-granules are significantly different when T8-or F8-anti-caking solutions are used. Granules coated with T8-anti-caking solution have a smaller caking tendency because of the smaller crystal bridge formation between the granules.
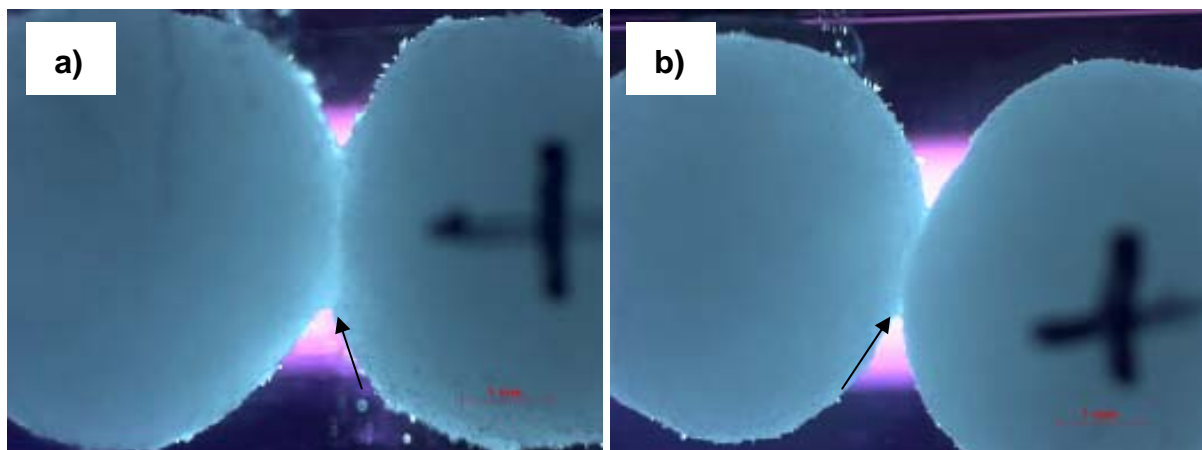
Figure 3.12: Light microscopy images of granules coated with F8-anti-caking solution (a) and T8-anti-caking solution (b).

The surface of the uncoated granules (pure urea granules) and caked granules after stored at 40 °C and 75 % relative humidity for 3 days in DPS are observed using ESEM, especially the surface of fracture area between double-granules (see arrows in Fig. 3.12 a and b) after tensile tests can be visualized. Surfaces of uncoated granules and the granules coated with PSN anti-caking solution are shown in Figure 3.13 a and b.
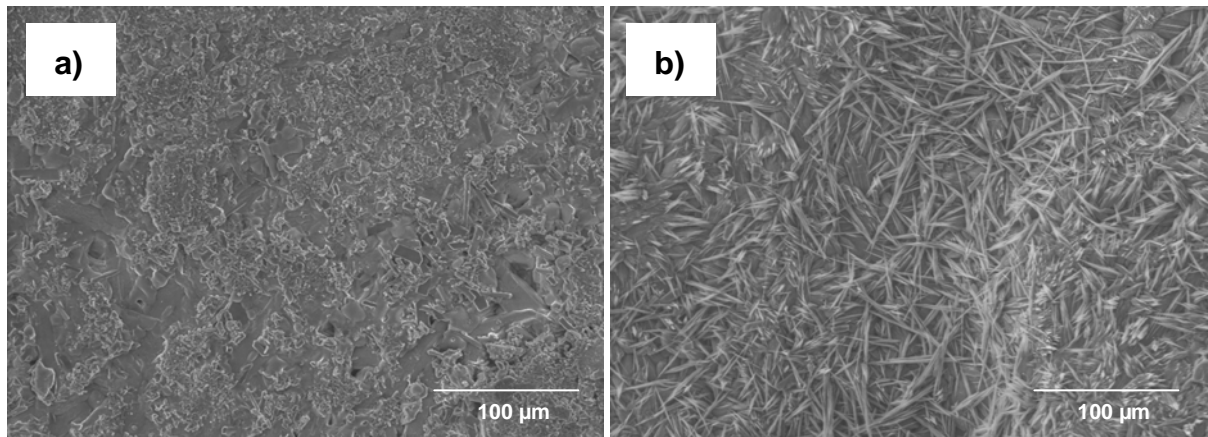
Figure 3.13: ESEM images of surface of uncoated urea granule (a) and granules coated with PST solution (b).

The surface of uncoated urea granules and coated granules are quite different. Many needle-like crystals can be observed on coated granules, which are formed by NI. Furthermore, these needle-like crystals are homogenously dispersed on the granule surface indicating that the coating of the solution is uniform, i.e. the anti-caking solution is homogeneously spread (wetted) on the basis granules during the coating process.

ESEM images of granules coated with F8- and T8-anti-caking solution after caking experiments and tensile tests are shown Figure 3.14 a to f.
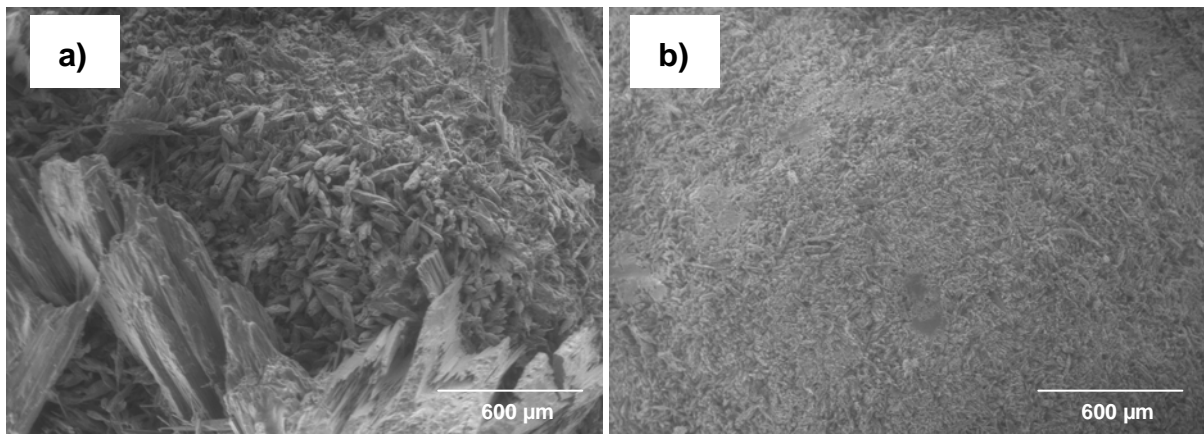
Figure 3.14: Surface of F8-anti-caking solution coated granules (a) and T8-anti-caking solution coated granules (b). Surface of fracture area of with F8-anti-caking solution coated granules after caking experiments and tensile tests (c) and its enlarged image (d). Surface of fracture area of with T8 anti-caking solution coated granules after caking experiments and tensile tests (e) and its enlarged image (f); the fracture area by tensile tests is indicated by arrows in the Figure.
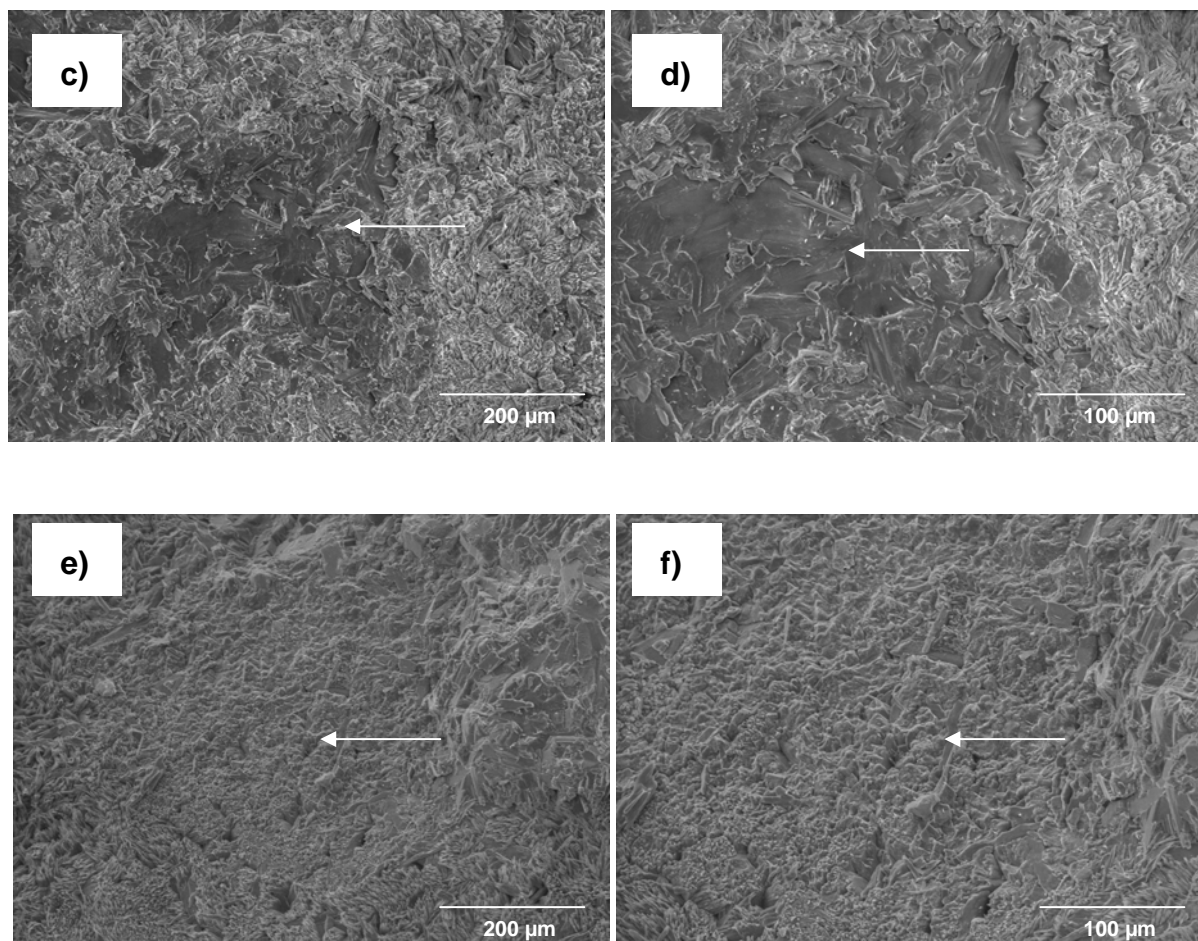
Figure 3.14 a and b show the surface of granules after caking experiments, i.e. stored at the 40 °C and 75 % relative humidity for 3 days and then dried at 25 °C and 30 % relative humidity for 2 days. On the surface of F8-anti-caking solution coated granules, there are not only small needle-like crystals but also large crystals formed by re-crystallization shown in the left part in Figure 3.14a. It can be observed that the size of these large crystals is approximately 1 mm × 1 mm. On the contrary, granules coated with T8-anti-caking solution after caking experiments only have the small needle-like crystals and a smoother surface can be seen. In fact, the size of the fracture area is reflected by the crystal bridge formed during the caking experiments (coated granules are stored at the 40 °C and 75 % relative humidity for 3 days and then dried at 25 °C and 30 % relative humidity for 2 days). The hardening phenomenon can be visualized by detecting the surface of the fracture area of the caked granules. From

Figure 3.14c, the surface of the fracture area of F8-anti-caking solution coated granules is very smooth. Depending on the caking mechanism,[16] the fertilizer dissolved and diffused to hole structures during the storage under the condition of high relative humidity leading to hardening of the caking areas after humidity decreased. A smoother surface of fracture area observed with F8-anti-caking solution coated granules reflects larger parts of granules dissolved at high relative humidity and large amount of solution transferred into pore structures. It is in agreement that a harder and stronger caking of F8-anti-caking solution coated granules is measured by tensile tests. However, the surface of fracture area of T8 solution coated granules is not smooth and some small pore structures can be observed in Figure 3.14 e and f reflecting that less part of the granules are dissolved and transferred into pores when stored at high humidity.

3.3.4 Tensile tests of anti-caking solution coated metal plates

The different PSN solutions are placed on the coating areas of metal plates, and then they are stored in the drying oven at ~ 45 °C for 3 days. Each PSN solution is placed on 5 metal plates for 5 times tensile test measurements in order to obtain the average value. The detailed coated metal plates separation values (separation loads) by tensile tests are listed in the Table 3.9. The largest separation loads by tensile tests are measured by metal plates coated with PVA-F8-NI and P116-T8-NI, i.e. approximately 12 ± 1.2 N; however the separation loads of metal plates coated with P98-T8-NI by tensile test is only 3.7 ± 0.49 N, which is approximately one third of F8-anti-caking solution coated samples. Hereby, caking between PSN solutions coated granules and production line is due to the re-crystallization of fertilizers during the production and adhesive behavior of PVA solution after drying. The separation loads of PSN solution coated metal plates are more or less related to adhesions of PVA solutions after they are dried. Usually, adhesions of dried PVA solutions depend on the hydrolysis degree (HD).[42] Adhesion of dried PVA solutions to smooth surfaces (metal foil and glass) improves with the lower degrees of hydrolysis.[42] The re-crystallization behavior of granules has been discussed in previous part. Therefore, the effects of PVA with different HDs are discussed here. The data in Table 3.9 show that smaller separation loads are measured when a higher hydrolysis degree PVA is used in the solutions and coated on the metal plates, e.g. PA99, PA98, and P98. Coating solutions of PA98-T8-NI, P37-T8-NI, P80-T8-NI and P116-T8-NI are chosen to analyze the relationship between the hydrolysis degree of PVA and the separation loads of solution coated plates. In Figure 3.15, the plot of tensile strength as a function of the hydrolysis degree of PVA is shown indicating an exponential relation, i.e. the separation loads

increase about exponentially with increasing degree of hydrolysis of PVA.

Table 3.9: Separation loads of PSN coated metal plates after stored at 45 °C for 3 days by the tensile tests.

Solutions coated on the metal plate	Separation loads [N]
PVA-F8-NI	11.44 ± 1.2
P98-T8-NI	3.7 ± 0.49
P37-T8-NI	4.3 ± 0.4
P80-T8-NI	7.68 ± 0.5
P81-T8-NI	5.44 ± 1.07
P01-T8-NI	7.66 ± 0.23
P03-T8-NI	8.63 ± 1.43
PA99-T8-NI	4.62 ± 0.56
PA98-T8-NI	4.9 ± 1.2
P115-T8-NI	4.14 ± 1.22
P116-T8-NI	12.08 ± 0.58
P129-T8-NI	10.14 ± 0.8
P130-T8-NI	6.66 ± 0.56
P131-T8-NI	5.58 ± 0.71
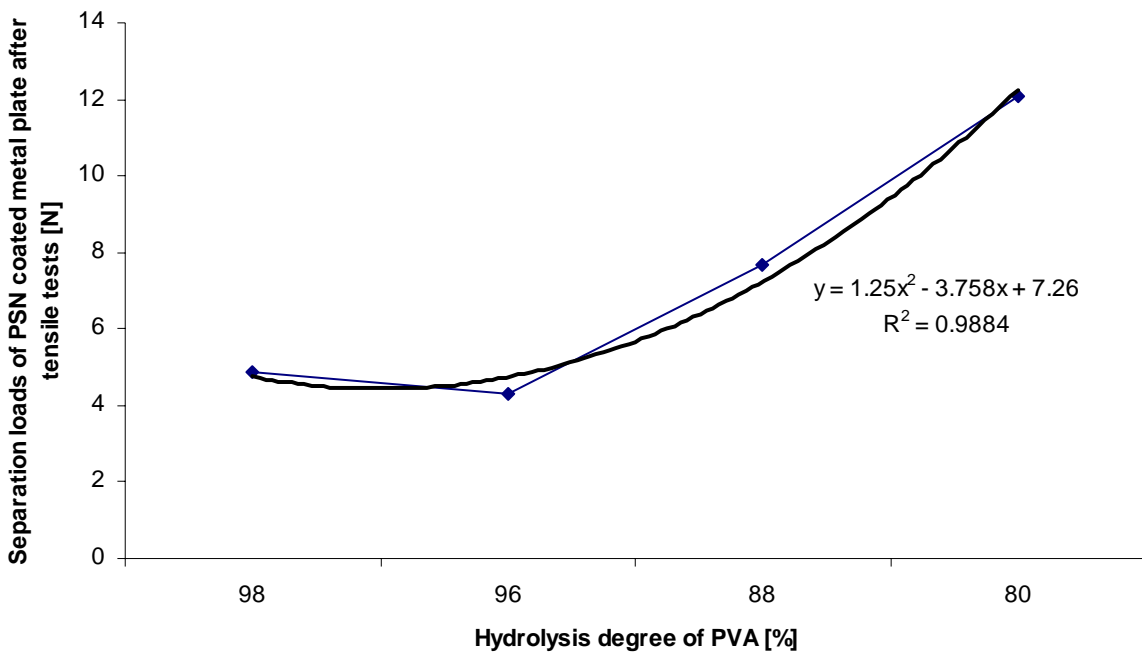
Figure 3.15: Separation loads between PSN solutions coated metal plates vs. HD of PVA.

The preparation processes of VSN and PVSN coated metal plates are the same as for PSN solutions. The storage condition is also identically, i.e. storage in a drying oven at 45 °C and for 3 days. The measured separation loads of VSN or PVSN coated metal plates by tensile tests are listed in Table 3.10. The separation loads increase with increasing PVP concentrations in PVSN solutions. In other word, the application of PVP in the solutions

increases strongly the adhesions between coated metal plates. After drying of metal plates coated with PVSN and VSN solutions, the films between the plates can easily absorb water from the environment and behave as the glue due to the hygroscopic properties of PVP. It can be imagined that granules coated with VSN or PVSN solutions have a stronger caking behavior on the production line. The plot of separation loads of PVSN or VSN coated metal plates as a function of PVP concentration is shown in Figure 3.16.

Table 3.10: Separation loads of VSN and PVSN coated metal plates after stored at 45 °C for 3 day by tensile tests.

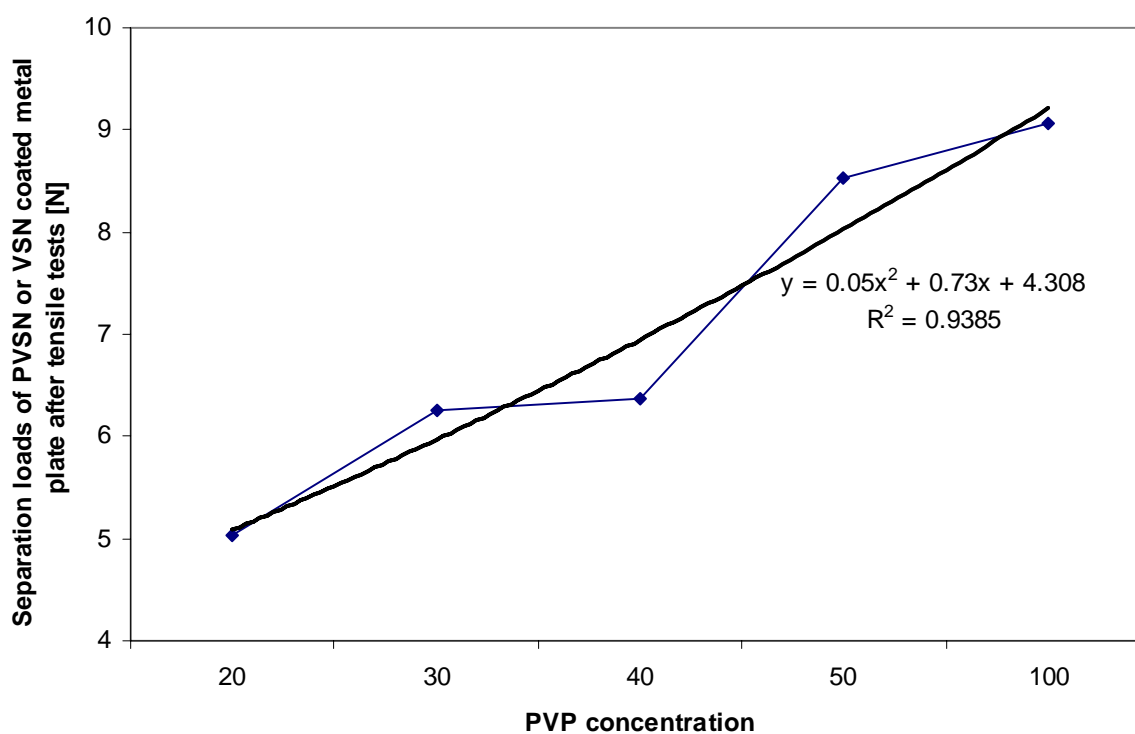| Solution coated on the metal plate	Separation loads [N]
P98-PVP-T8-NI (80:20)	5.04 ± 0.67
P98-PVP-T8-NI (70:30)	6.26 ± 1.59
P98-PVP-T8-NI (60:40)	6.36 ± 2.27
P98-PVP-T8-NI (50:50)	8.52 ± 2.1
PVP-T8-NI (0:100)	9.06 ± 1.02

Figure 3.16: Separation loads of VSN (PVSN) coated metal plates vs. PVP concentration.

3.4 Conclusions

The anti-caking effects of surface active anti-caking agents are investigated and the results are discussed in this chapter. Various anti-caking solutions are coated on the fertilizer granules.

The surface of uncoated urea granules and PSN solution coated granules are observed using ESEM indicating that anti-caking solutions are homogenously coated on the granules. The needle-like crystals of NI are uniformly dispersed on the granule surface. KFT is carried out to measure water contents of uncoated urea granules and PSN solution coated granules. After 2 days storage at the room condition (room temperature and room relative humidity), the initial water contents of T8-anti-caking solution coated granules are 100 ppm smaller than that of F8-anti-caking coated granules. The smaller initial water contents result in a smaller caking tendency.[17] These PSN coated granules are stored in DPS and MPS at two different conditions in order to obtain caked granules for measuring the destroying loads of de-caking by tensile tests. After they are caked together, two mechanical tests in the lab scale, i.e. tensile tests and free falling lump tests are designed and carried out to measure the destroying loads of de-caking of granules and the weight of still caked granules after falling of caked granule lump followed by a calculation of anti-caking ratio. After 5 days storage in the climate chamber (3 days at the elevated temperature and relative humidity for dissolving the surface of granules and another two days at the room temperature and relative humidity for drying, i.e. re-crystallization), two granules are caked in DPS. The smallest destroying loads are measured when T8-anti-caking solution is coated on the granules indicating that the lowest amount of water absorption from the atmosphere during storage and smallest crystal bridges are formed between the granules. However, F8-anti-caking solution coated granules have the highest destroying loads for the de-caking of the caked double-granules. The influence of different hydrolysis degrees of PVA used in the anti-caking solution on the caking of granules is discussed. Due to the stronger hydrophobic property and lower solubility, smaller destroying loads of de-caking are measured when higher hydrolysis degrees of PVA were used for the preparation of the anti-caking solutions. The images obtained by light microscopy visualize the crystal bridge between coated granules after storage at high relative humidity. The bridges between T8-anti-caking solution coated granules are smaller than that of F8-anti-caking solution coated granules, thus a weaker de-caking force (destroying loads) is measured by tensile tests. A smoother and larger area of fracture surface is observed on F8-anti-caking solution coated granules using ESEM. It is believed that herein the crystals dissolved and re-crystallized more strongly during the caking experiments leading to the hardening of the salt bridge. The results of free falling lump tests agree with those of tensile tests, i.e. granules coated with T2- and T8-anti-caking solution do not cake after they were stored at 25 °C and 85 % relative humidity in the climate chamber. When the temperature of storage increased to 40 °C, the anti-caking ratios of T8-anti-caking solution coated granules are in the range of 75 % - 85 %. VSN and PVSN solutions coated granules are also tested by modified mechanical

tests. The anti-caking effects are not improved significantly compared with those of granules coated with PSN solutions, although various ratios of concentrations of PVP in PVA solutions are prepared.

Tensile tests are carried out to measure the separation loads (adhesion) between the anti-caking solution coated metal plates to investigate the caking of coated granules on metal parts of the production line. With increase of the hydrolysis degree of PVA used in the coating solution, the separation loads between PSN solution coated metal plates becomes smaller since the adhesion of dried PVA solution to smooth surfaces (e.g. metal foil and glass) improves with the lower degrees of hydrolysis.[42] When VSN or PVSN were coated on metal plates, with increase of PVP concentration in the solution, separation loads markedly increases due to the hygroscopic properties of PVP indicating a strong caking of PVSN or VSN coated granules to metal parts of the production line.

Chapter 4

Investigation of blends of iron oxide nanoparticles and block copolymers

4.1   Introduction

Langmuir-Blodgett (LB) technique, layer-by-layer (LBL) deposition, and self-assembly have been used for preparation of mono- and multilayers of polymers.[112,113,114] The LB technique is most suitable to transfer non-ionic amphiphilic polymers from the air/water interface to solid substrates. Amphiphilic block copolymers are usually composed of mutually immiscible blocks. They are known to form self-assembled nanostructures of various morphologies in the presence of selective solvents and surfaces.[115,116] Numerous reports deal with the behavior of amphiphilic block copolymers at the air/water interface by measuring surface pressure versus mean molecular area (π-mmA) isotherms e.g. for poly(ethylene oxide) (PEO)-based amphiphilic block copolymers.[117,118,119,120] In general, during the compression of monolayers of block copolymers containing PEO as hydrophilic block, the Langmuir isotherms show an intermediate plateau region at π-values of approximately 10 mN/m corresponding to the dissolution of the PEO block from the water surface into the subphase known as pancake to brush transition.[121,122,123,124] This plateau region is more pronounced for block copolymers having large PEO contents. The π-mmA isotherms of poly(isobutylene) (PIB)-based amphiphiles have an extended plateau at approximately 41 mN/m corresponding to the multilayer formation,[125] the so-called roll-over collapse.[126] Additionally, after transferring monolayers from the water surface to silicon substrates, a finger-like morphology of PEO crystals is observed by using atomic force microscopy (AFM). They are formed due to the conformational difference between the PEO chains adsorbed on the silicon surface and the chains that are not adsorbed.[127,128,129] This morphology can only be observed if the film is sufficiently thick or after significant supercooling to overcome the nucleation barrier.[130] Amphiphilic block copolymers on the solid substrates are of considerable scientific interest and have potential applications.[131] In the recent decade, magnetic nanoparticles became important due to various applications in the fields of catalysis, optics, bio-sensing materials, and magnetic resonance imaging.[132,133,134,135,136,137,138] Many of these applications require iron oxide nanoparticles (Fe_2O_3-NPs) to possess good chemical and physical stability and uniform sizes. As a result of anisotropic dipolar attraction, the pristine Fe_2O_3-NPs tend to aggregate into large clusters and thus lose specific properties associated with single-domain

nanostructures. Using polymers or surfactants as ligands or stabilizing agents not only prevents the agglomeration of the nanoparticles for obtaining chemical and mechanical stabilities but also induces various functionalities caused by the polymeric shell such as biocompatibility and molecular recognition.[87,88,89] Several reports have described magnetic nanoparticles with long chain fatty acids as organic shells in LB films;[139,140] e.g. magnetite and cobalt-ferrite nanoparticles were coated with oleic acid shells.[141] A precisely controlled thickness and homogeneity of monolayers of nanoparticles are obtained.[142] Additionally, a hierarchical structure has been observed when polystyrene coated cadmium sulfide nanoparticles are mixed with PEO-*b*-PS copolymers after transfer to solid supports.[143,144] Groenewolt et al. and Brezesinski et al. have reported that self-assembled highly ordered materials, such as iron oxide mesoporous films, were obtained using PEO-*b*-PIB block copolymer templates.[78,79]

The present study deals with the phase behavior of monolayers formed by amphiphilic block copolymers of PEO-*b*-PIB and its mixtures with hydrophobically modified Fe_2O_3-NPs at the air/water interface determined by the measuring of Langmuir isotherms. The resulting morphologies of the LB films after transfer to silicon substrates are investigated by atomic force microscopy (AFM). Both PEO and PIB phases of the block copolymers are observed, and the behavior of nanoparticles mixed with the copolymer is discussed.

4.2   Experimental section

4.2.1   Materials

Diblock copolymers of PEO-*b*-PIB used in this study were synthesized and characterized as reported elsewhere.[145,146] The general structure is given in Chart 4.1a. The detailed molecular characteristics can be seen in the Table 4.1. Iron oxide nanoparticles were prepared via exchange reactions.[147] The structure and dimensions of Fe_2O_3-NPs are given in Chart 4.1b. The core of iron oxide nanoparticles with a diameter of 100 Å was coated with a shell of oleic acid ligands. There were approximately 880 oleic acid ligands on the surface of one nanoparticle. The molar mass of the capped nanoparticle was 1.814×10^6 g/mol. In addition to neat copolymer and nanoparticle solutions, also mixtures of Fe_2O_3-NPs with PEO_{97}-*b*-PIB_{37} (FeNPEB) were prepared. The ratio of particle number to polymer chain number between Fe_2O_3-NPs and PEO_{97}-*b*-PIB_{37} was 1 to 100.

Chart 4.1: (a) Molecular structure of PEO-*b*-PIB diblock copolymer. (b) Structure of iron
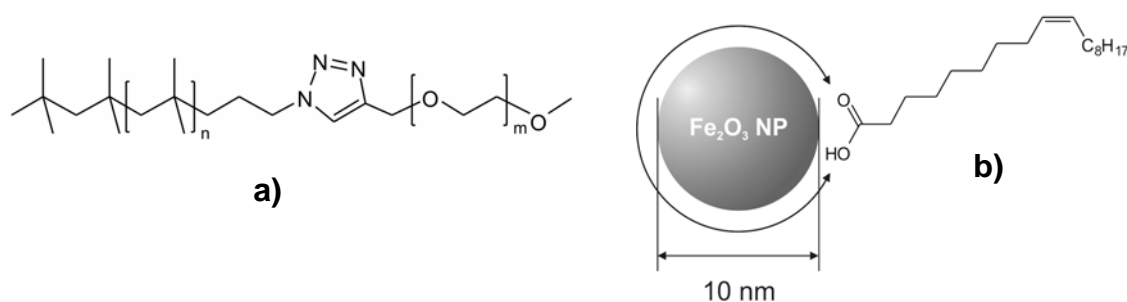
oxide nanoparticles (Fe_2O_3-NPs).

a)

b)

10 nm

Table 4.1: Molecular characteristics of the block copolymers.

Copolymer	DP_{PEO}	DP_{PIB}	PD	M_n (g/mol)
PEO_{97}-b-PIB_{37}	97	37	1.1	6 400
PEO_{19}-b-PIB_{130}	19	130	1.1	8 200

Degree of polymerization (DP) of the respective block determined by ^{1}H NMR spectroscopy. Number average molar mass M_n and polydispersity (PD) were determined by GPC using polystyrene standards.

4.2.2 Surface pressure measurements

The surface pressure isotherms of PEO-b-PIB copolymers and NPs at the air/water interface, i.e. the plots of surface pressure (π) versus the mean molecular area (mmA), were measured with a Langmuir trough system (KSV, Helsinki) equipped with two moving barriers and a microroughened platinum Wilhelmy plate. The maximum available surface area of the Langmuir trough was 76800 mm^2. For subphase, water was purified using a Purelab option system (ELGA Ltd., Celle, Germany) equipped with an organic removal cartridge (conductance <0.06 µS/cm). The purity of the bare water surface was checked before each measurement by a maximum compression ($\pi < 0.15$ mN/m). The temperature of the water subphase was maintained at 23 °C by using a circulating water bath system. Predetermined amounts of the solution of the block copolymers (or the mixture with nanoparticles) in chloroform (HPLC grade) (5 mg/ml) were spread evenly on the subphase in 3 µl by using a digital microsyringe (Hamilton). The compression at a constant rate of 5 mm/min was started after 20 min to ensure the full evaporation of solvent and uniform diffusion of molecules on water. To obtain complete isotherms, each measurement was repeated with increasing amount of copolymer solution leading to different initial pressures and thus different parts of isotherm were recorded. After combining the data into one plot, the parts fit together within the experimental error (see supporting information). The experimental setup was placed in a sealed box for the minimization of dust particles and a constant humidity.

4.2.3 Langmuir-Blodgett deposition

Silicon wafers were used for the deposition of monolayers. They were cut into 25 × 15 mm substrates, and cleaned with double distilled water and CO_2 dry snow jet. After this treatment a clean hydrophilic SiO_2 surface was obtained. For LB film preparation, cleaned substrates were submersed into water before compression. After the desired surface pressure was reached, the monolayer was allowed to stabilize for 20 min. Then, the monolayers were transferred onto the substrates at constant pressure by a vertical uptake through the film at a constant rate of 5 mm/min. Multilayer films were obtained by dip coating using silicon substrates. Ten layers were deposited on the substrate by moving it vertically from and into the water subphase with 20 min interval for films stabilization. The transferred films were allowed to dry in a desiccator at room temperature for 24 h.

4.2.4 Atomic force microscopy

In order to investigate the LB film morphologies an atomic force microscope (NanoWizard, JPK Instruments, Berlin) operated in tapping-mode with silicon cantilevers was used. The cantilevers (Arrow, NanoWorld, Neuchâtel) had a resonance frequency of ~ 285 kHz and a force constant of ~ 42 N/m.

4.3   Results and discussion

4.3.1   Surface pressure-mean molecular area isotherms

Figure 4.1a shows the compression isotherm of PEO_{97}-b-PIB_{37}. This isotherm is similar to the isotherms of PEO-based amphiphilic diblock copolymers with a relatively small length of the hydrophobic block compared to the PEO block.[117,118,119,120] At low surface pressures, a typical liquid-expanded monolayer is observed, where the hydrophobic PIB segments anchor the polymer chain to the surface, while the PEO adopts a flattened conformation at the air/water interface due to its affinity to the water (pancake). The first significant increase of the surface pressure is observed at mmA of approximately 3100 $Å^2$. This corresponds to an area of 32 $Å^2$ per EO monomer unit, which coincides with the reported value for PEO homopolymers.[148] During further compression, a plateau is observed up to an mmA value of approximately 330 $Å^2$. In the plateau range, the surface pressure increases only slightly upon compression from 9

to 12 mN/m. This reflects the typical behavior of anchored PEO chains at the air/water interface. The end of this transition is determined by the size of the hydrophobic block. Further compression leads to a sharp increase of the surface pressure until film collapse at surface pressure of ~ 50 mN/m and mmA of ~ 100 Å^2.

Due to the hydrophobicity of PIB it can be assumed that PIB chains try to orient perpendicular on the water surface to reduce contact area with water and PEO chains. Using the molar mass of the PIB block of 2072 g/mol, the Avogadro number, and the bulk density of PIB of 0.96 g/cm,[149] the volume of one PIB block can be calculated (i.e. 3583 Å³). Thus the average thickness of the hydrophobic layer formed by PIB blocks at the water surface can be calculated for the end of the plateau region where all PEO chains are stretched into the water subphase. The further increase of surface pressure is then governed by the reorientation of PIB blocks. Since PIB chains at room temperature are far above T_g and thus they are highly flexible and sensitive to compression on the water surface, so that the density of PIB may change with different mmA values due to orientation effects slightly (less than 10%). Dividing the volume of one PIB block by the mmA of 330 Å^2 yields an average thickness of the hydrophobic layer of ~ 10 Å. It should be stressed again, that the PIB layer is not necessarily homogeneous, but an averaged overall thickness is calculated. The average thickness of the layer at collapse calculated by the same procedure is ~ 30 Å.
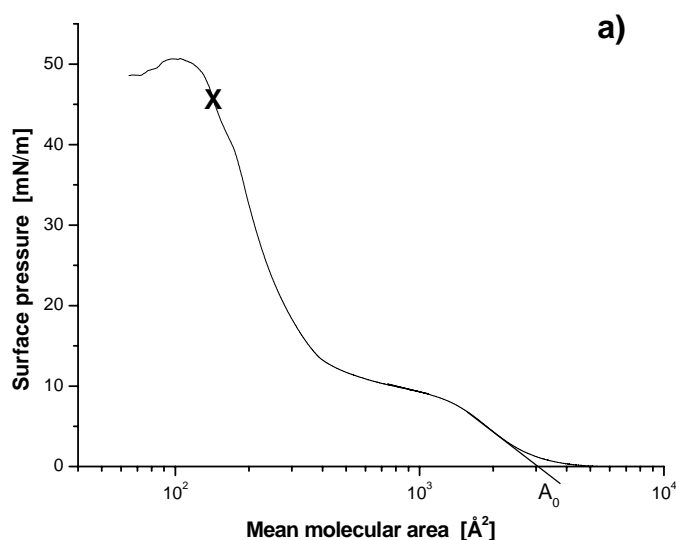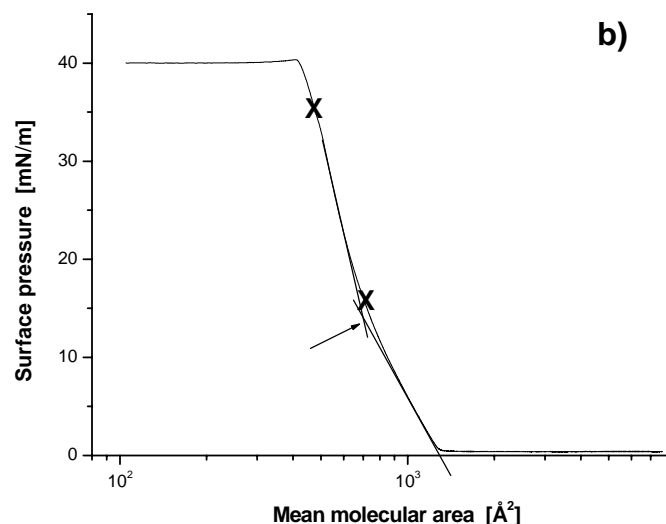
Figure 4.1: (a) π-mmA isotherm of PEO$_{97}$-b-PIB$_{37}$. The plateau is observed at $\sim$ 10 mN/m. The intersection of the tangent and x-axis gives a value of 3100 Å^2. (b) π-mmA isotherm of PEO$_{19}$-b-PIB$_{130}$. The roll-over collapse plateau is observed at $\sim$ 41 mN/m. Above the inflection point (see arrow), the surface pressure increases sharply. Monolayers are transferred to silicon substrates at surface pressures indicated by **X**.

Figure 4.1b shows the isotherm of the more hydrophobic block copolymer PEO$_{19}$-b-PIB$_{130}$ having a higher PIB content compared to the previously discussed block copolymer. The mmA of the first steep increase of the surface pressure is approximately 1200 Å^2. This mmA value is obtained by extrapolating the steepest part of the isotherm to the zero surface pressure. Dividing this area by the volume of PIB units obtained by the same procedure as discussed above, once again an average PIB layer thickness of $\sim$ 10 Å is obtained. Therefore, it can be assumed that the arrangement of PIB blocks coming into contact at the air/water interface is similar in both block copolymers. Due to the very high PIB content, the typical PEO related phase transition at a surface pressure of approximately 10 mN/m completely disappeared. There is an inflection point of the Langmuir isotherm at 13.5 mN/m and 700 Å^2, above which the surface pressure increases sharply. This corresponds to an average layer thickness of $\sim$ 17 Å.

The film collapse starts at an mmA value of $\sim$ 415 Å^2, which corresponds to an average layer thickness of $\sim$ 30 Å. It appears as a single plateau with a quite constant surface pressure of $\sim$ 41 mN·m^{-1}. For similar hydrophobic block copolymers this behavior has previously been explained as multi-layer formation upon compression.[125] The multi-layer formation is the result of the so called roll-over collapse.[126] In order to get more information on the film morphology, AFM images of both block copolymers transferred at different surface pressures

will be shown and discussed below. Of course, it has to be mentioned that the morphology of the Langmuir films on the water surface is not necessarily identical with the morphology of the transferred films on solid supports.

Figure 4.2 shows the π-mmA isotherms of Fe_2O_3-NPs, FeNPEB, and for comparison the isotherm of PEO_{97}-b-PIB_{37} is added. The first increase of the surface pressure with decreasing mmA in the isotherm of Fe_2O_3-NPs is observed at 20470 $Å^2$. This can be considered as a gas to liquid transition. Before the sharp increase in surface pressure the soft hydrophobic oleic acid ligands (shell) surrounding the Fe_2O_3 core float on the subphase preventing precipitation and aggregation of iron oxide into the water subphase (see scheme in Figure 4.2).[150] The area of 20470 $Å^2$ can be related to the surface covering of spherical particles with a radius of 80 Å (radius of 50 Å of the nanoparticle core and a thickness of 30 Å of the shell of extended oleic acid). The value of 30 Å of the shell thickness reflects the oleic acid chains capped on the core of the nanoparticle and located at air/water interface. When the nanoparticles are mixed with PEO_{97}-b-PIB_{37}, the isotherm is similar to that of the pure block copolymer since the main contribution of surface covering comes from the block copolymer. The isotherm of FeNPEB shown in Figure 4.2 has two plateaus at ~ 8 and 41 mN/m corresponding to the pancake to brush transition of the PEO block and the collapse of the monolayer, respectively. The mmA of the mixture is related to area which is occupied by each individual (i.e. nanoparticles and polymer chains), which corresponds nearly to the area per polymer chain (deviation is only 1% due to the mixing ratio), which is also used for the pure polymer isotherm. Compared to the isotherm of neat PEO_{97}-b-PIB_{37}, the isotherm of the mixture has a shift of ~ 400 $Å^2$ to higher mmA values for surface pressures below 10 mN/m. This indicates an attractive interaction between the hydrophobic shell of nanoparticles and the hydrophobic block of the copolymer, leading to a rearrangement of the copolymer on the water surface and also to a reduction of the surface pressure at the plateau. Between 10 and 40 mN/m the isotherm has a shift of 150 to 200 $Å^2$ to higher mmA values, which corresponds to a simple additive contribution of the nanoparticles. At pressures above 40 mN/m this deviation vanishes, probably due to the arrangement of the nanoparticles on the top of the PIB phase.
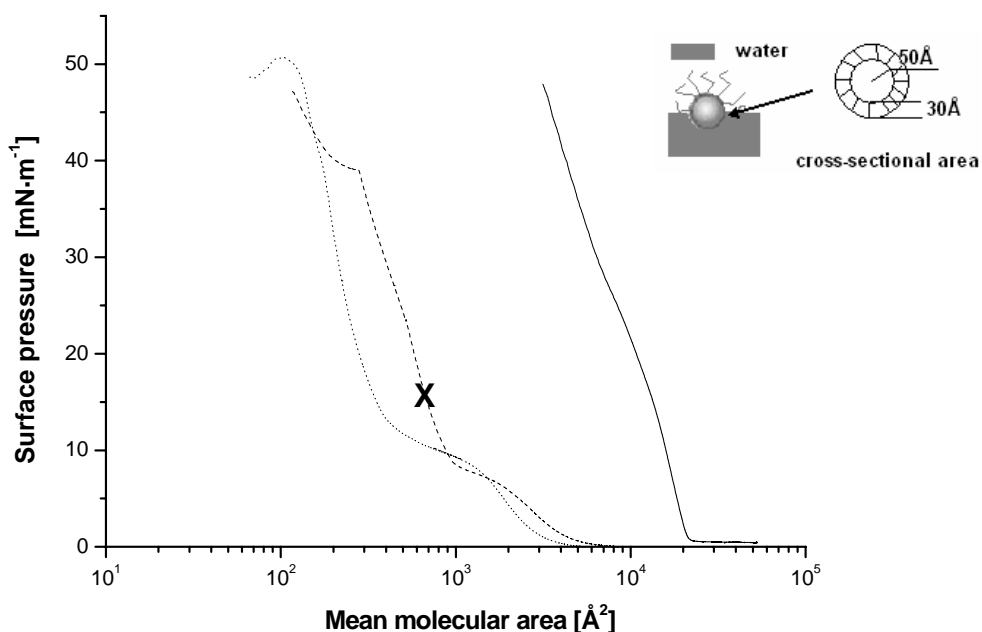
Figure 4.2: π-mmA isotherm of Fe_2O_3-NPs (solid line) and the mixture of Fe_2O_3-NPs with PEO_{97}-b-PIB_{37} (FeNPEB, dashed line). The isotherm of PEO_{97}-b-PIB_{37} is shown for comparison (dotted line). The scheme shows the behavior of nanoparticles on the water surface. The monolayer of FeNPEB is transferred to the silicon substrate at the surface pressure indicated by **X**.

4.3.2   Morphology of the Langmuir-Blodgett films

Monolayers of PEO_{97}-b-PIB_{37} and PEO_{19}-b-PIB_{130} were transferred onto silicon substrates by the LB technique. The transfer ratio is equal to the area of monolayer removed from the air/water interface divided by that of the substrate. In our experiments the transfer ratios are between 0.8 and 1.5 (note that a transfer ratio larger than 1 is frequently observed for polymers).[151] Figures 3a and b show the AFM image of PEO_{97}-b-PIB_{37} transferred at 45 mN/m (equivalent to an mmA of 145 $Å^2$; indicated by **X** in Figure 4.1a) and the respective height profile. The dominant morphology is the so called finger-like structure typical for crystallized PEO monolayers.[117,118,119] These finger-like crystals are formed due to the conformational difference between the PEO chains adsorbed on the silicon wafer surface and the chains that are not adsorbed during deposition. After water evaporation, crystallization of PEO starts. The morphology can only be observed if the film is sufficiently thick. Furthermore, small bright spots are seen and the corresponding height profile is given in Figure 4.3b. The bright spots can be assigned to mesomorphic chain structures of PIB as will be discussed in detail below. The term mesomorphic describes the early stage of

crystallization. During this stage the mobility of the PIB chains is large and spontaneous domain growth can occur. This phase is less ordered than the crystal phase.[152] The height of bright spots of ~ 90 Å corresponds to an extended chain ordering of all 37 PIB units having a perpendicular orientation to the subphase. From the height of the domains and the number of PIB units in the block copolymer it follows that one PIB unit has the length of ~ 2.4 Å. This length is similar to a PIB monomer unit length arranged in a 8_3 helix or in the all-trans conformation.[153,154] The apparent volume of PIB in the spots is much smaller than the total amount of PIB in PEO_{97}-b-PIB_{37}, therefore also a thin layer of PIB should cover the PEO part (finger-like morphology) which has an average height of approximately 110 Å (holes in the PEO phase). The corresponding phase image of the LB film of PEO_{97}-b-PIB_{37} is shown in the Figure 4.3c. The mesomorphic phase of PIB is marked by two arrows. In tapping mode AFM, the bright regions are caused by hard phases and on the contrary soft phases appear dark. Thus the mesomorphic phase of PIB (spots) has a similar hardness as PEO crystals. Details on the assignment of the PIB phase are discussed below.
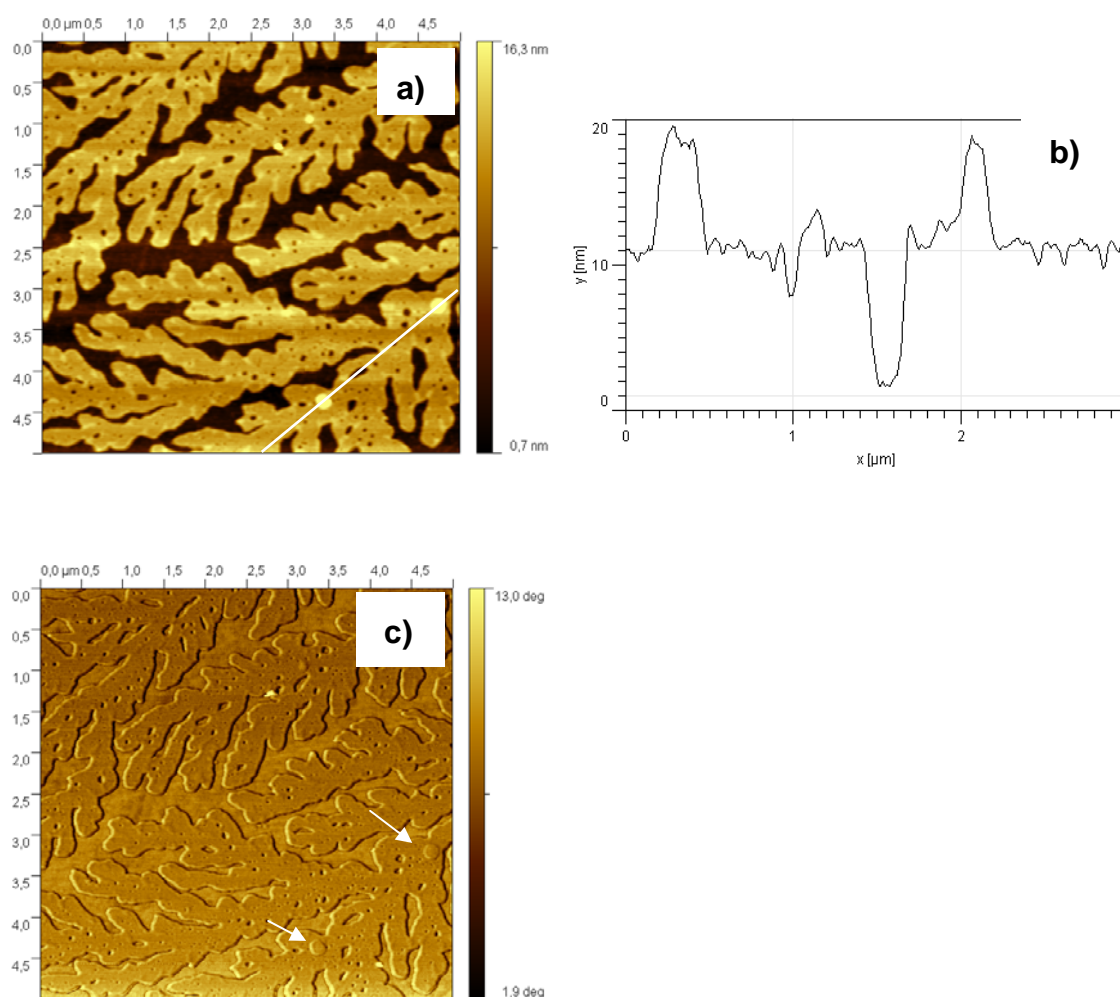

Figure 4.3: (a) AFM image of the PEO_{97}-b-PIB_{37} block copolymer transferred at the surface

pressure of 45 mN/m. (b) Height profile taken along the line in (a). (c) Phase image of (a).

Figure 4.4a and b show the AFM image and the height profile of PEO_{19}-b-PIB_{130} transferred at 15 mN/m (see Figure 4.1b). A rather disordered phase with some bright spots in between can be seen. The height of the bright spots reaches 105 Å and that of the surrounding phase $\sim$ 30 Å. The spots can again be assigned to the early stage of the formation of the mesomorphic PIB phase and the surrounding patches can be assigned to less ordered PIB and short PEO blocks. The surface pressure at transfer is chosen near to the phase transition indicated by the change of the slope of the isotherm shown in Figure 4.1b. Similar transitions in Langmuir isotherms can be observed for typical low molar mass amphiphiles as stearic acid or perfluorododecanoic acid.[155,156] In these cases it is the liquid condensed to solid phase transition. But a transition from some preordering to a higher order seems not to be likely for the block copolymer under discussion since the transition occurs at a relatively small surface pressure of 13.5 mN/m. For PEO_{19}-b-PIB_{130} it can be assumed that a uniform amorphous film or domain structures of PIB (dewetting as discussed for poly(ethylene oxide)-$block$-polystyrene copolymers[157,158]) are formed at the air/water interface prior to the phase transition at low surface pressures. Upon compression, the amorphous PIB monolayer can start locally to form mesomorphic PIB domains, i.e. some parallel arrangement of PIB chains perpendicular to the water surface can occur. Thus the bright spots mentioned above indicate a nucleation event. It cannot be judged unambiguously if this happened already on the water surface or after film transfer. This would require additional experiments on the Langmuir trough as GI-WAXS or infrared reflection absorption spectroscopy (IRRAS).[159,160] These mesomorphic structures have been detected in thin PIB films collected from the water surface and studied by wide angle X-ray scattering.[161] Santangelo et al. have reported that the entanglement molar mass of PIB is $\sim$ 9 400 g/mol, which is much larger than the molar mass of PIB blocks used in our experiments.[162] This fact might also contribute to the parallel alignment of PIB chains in the mesomorphic phase upon compression on the water surface. Additionally, the very low glass transition temperature of PIB ($\sim$ -70 °C)[163] yields a high chain mobility and allows for the conformational rearrangement of the polymer, especially for the PIB blocks having a molar mass below the entanglement molar mass. A complex behavior can be expected when the molar mass of the flexible hydrophobic block in Langmuir films is above the entanglement molar mass as discussed for poly(isoprene-b-methyl methacrylate).[164] However, the finger-like patterns for PEO crystals are not observed. This demonstrates that the PIB content in PEO_{19}-b-PIB_{130} is large enough to suppress the crystallization of PEO as discussed for bulk crystallization of block copolymers.[165] This phenomenon was also

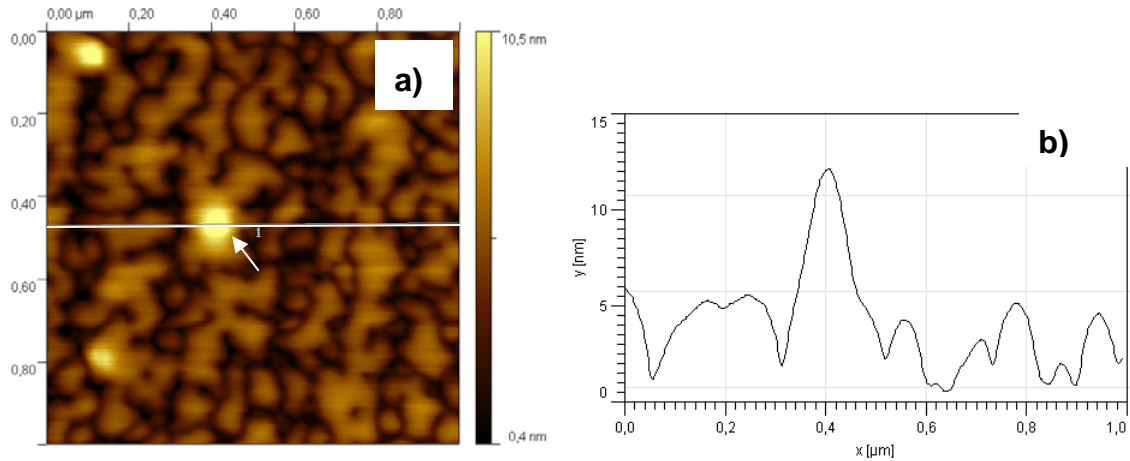observed in LB films of block copolymers of PEO and poly(ß-caprolactone) by Joncheray.[166]

Figure 4.4: (a) AFM image of the PEO$_{19}$-b-PIB$_{130}$ block copolymer transferred at the surface pressure of 15 mN/m. (b) Height profile taken along the line in a).

When PEO$_{19}$-b-PIB$_{130}$ was transferred at 35 mN/m, larger and more ordered extended mesomorphic domains of PIB are observed and the amorphous regions disappeared completely as can be seen in Figure 4.5a. Furthermore, between the spots no soft material can be detected. In order to prove, if the disintegration of the uniform film occurred already on the water surface, relaxation experiments have been performed. Relaxation experiments of PEO$_{19}$-b-PIB$_{130}$ are done by moving the barriers on the Langmuir trough in order to keep the surface pressure constant at 35 mN/m for 30 min. During this time the mmA values change only slightly from 478 to 440 Å^2. The Avrami equation (Equation 4.1) is applied to fit the plot of mmA as a function of time as shown below:[167]

$$\frac{A_0 - A}{A_0 - A_\infty} = 1 - \exp[-K_x (t - t_i)^n] \tag{4.1}$$

Where A_0 is the initial monolayer area, A is the monolayer at the time t, A_∞ the monolayer area for large times, t_i the induction time (equals 0 in the fit), and the exponent n is a characteristic quantity. n is the so-called Avrami exponent. Typically Avrami exponents above 1.5 describe crystallization phenomena whereas lower values can be attributed to relaxation processes. The exponent obtained by the fit is n=0.5. Thus there is no indication that crystallization of PEO$_{19}$-b-PIB$_{130}$ occurred already on the water surface. Furthermore, it has been known that film collapse or slow phase transitions of polymers like crystallization can occur on the water surface, leading to a decrease of e.g. 50% in mmA,[168] when the surface pressure is kept constant. On the other hand, the compression of a polymer monolayer is very often not in equilibrium. Also in compression isotherms of phospholipids and surfactants first order phase

transitions occur, that do not show a constant plateau region (which would be predicted by theory). Thus the decrease of 8% of mmA of our measurements is typically for relaxation phenomena. This means that a stable film is formed on the Langmuir trough during compression but is destroyed during or after the transfer. The amount of material, occupied by the columnar structures, agrees within several percent with the expected amount. 3D AFM images of PEO_{19}-b-PIB_{130} are shown in Figure 4.5b. A columnar morphology with different heights, but each column with a flat surface, is observed (see Figure 4.5b and c). From the height profile taken along the line in Figure 4.5a, different discrete height values of approximately 100 and 300 Å can be observed. Also other columns with a well defined height of 150 Å have been observed at different locations of the sample, but most of the columns have a uniform height of 100 Å. No other heights have been detected, indicating that the columns are formed by well-ordered PIB chains. It can be seen in Figure 4.5d that these columns are not exactly cylindrical, i.e. their cross-section is not always a perfect circle. This is another indication that a mesomorphic phase or crystallization phenomena are involved in contrast to simple dewetting phenomena. For flexible chains the dewetting should result in simple sessile droplets which obviously do not appear. As discussed in the literature, the length of monomeric PIB units arranged in a 8_3 helix is 2.33 Å.[153,154] In PEO_{19}-b-PIB_{130} the height of 130 PIB monomeric units is thus 300 Å, which is related to the highest columns observed by AFM (see Figures 4.5a-c). Therefore, it can be assumed that the PIB chains are totally extended without any folding to form mesomorphic domains with a height of 300 Å. Furthermore, the other heights of the columns observed at around 100 and 150 Å, respectively; indicate PIB chain folding (see Figure 4.6). As already mentioned it has been known that PIB forms a phase with mesomorphic chain arrangement in thin films on the water surface.[161] This phase can be considered as mesomorphic having already some Bragg reflections but not yet the order of completely crystallized PIB. Obviously during compression of the block copolymer at the air/water interface, a strain acts on the both blocks. The PEO block forms a brush reaching into the water subphase. Locally, also the PIB block can form extended chain structures (either in a helix or all-trans) in the mesomorphic phase by repulsive interactions to water and the PEO block. Additionally the films compression results in a strain acting on the PIB blocks. Since PIB is a flexible polymer, for the change of the random coil conformation into an extended-chain conformation it is necessary that the conformational relaxation time is sufficiently small compared to the time where the block copolymer is exposed to the strain.[169] Altogether it seems to be a reasonable scenario that PIB chains undergo some orientation at the air water/interface upon compression of the Langmuir films. This is in agreement with the fact that lamellar liquid crystals of surfactants with short

PIB chains in bulk as well as in water have been reported.[170]

Liquori and Tanaka et al. have reported the crystal structure of PIB obtained on oriented fibers.[153,154] The length of a PIB monomer unit is 2.33 Å. The orthorhombic unit cell has dimensions of a = 6.88 Å, b = 11.91 Å and c (fiber axis) = 18.60 Å. It contains two polymer chains each consisting of eight monomeric units in the c-direction.[153] Assuming crystallization of PIB (or a mesomorphic state), the cross-sectional area of a vertically oriented PIB chain is half of 6.88×11.91 Å^2 which is equal to approximately 40 Å^2. For further calculations, the dimension of the crystalline order is used to describe the characteristic length scales of PIB units, although the dimensions of the extended chain (all-trans) structure are slightly larger. Another evidence for the formation of a mesomorphic PIB phase on the silicon substrate is shown in Figure 4.5e, which is the corresponding 3D image of the PEO$_{19}$-b-PIB$_{130}$ monolayer after storing for 4 weeks at room temperature. The morphology changed from columns to droplets. It implies that the PIB domains melted and coalescence occurred with the formation of larger domains on the silicon substrate. The droplets reach a height of 930 Å. Krishnamurthy and McIntyre reported a half-life time of 22 days for mesomorphic domains obtained in thin PIB films.[161]

e)

93 nm

0 nm

y: 20 μm

x: 20 μm
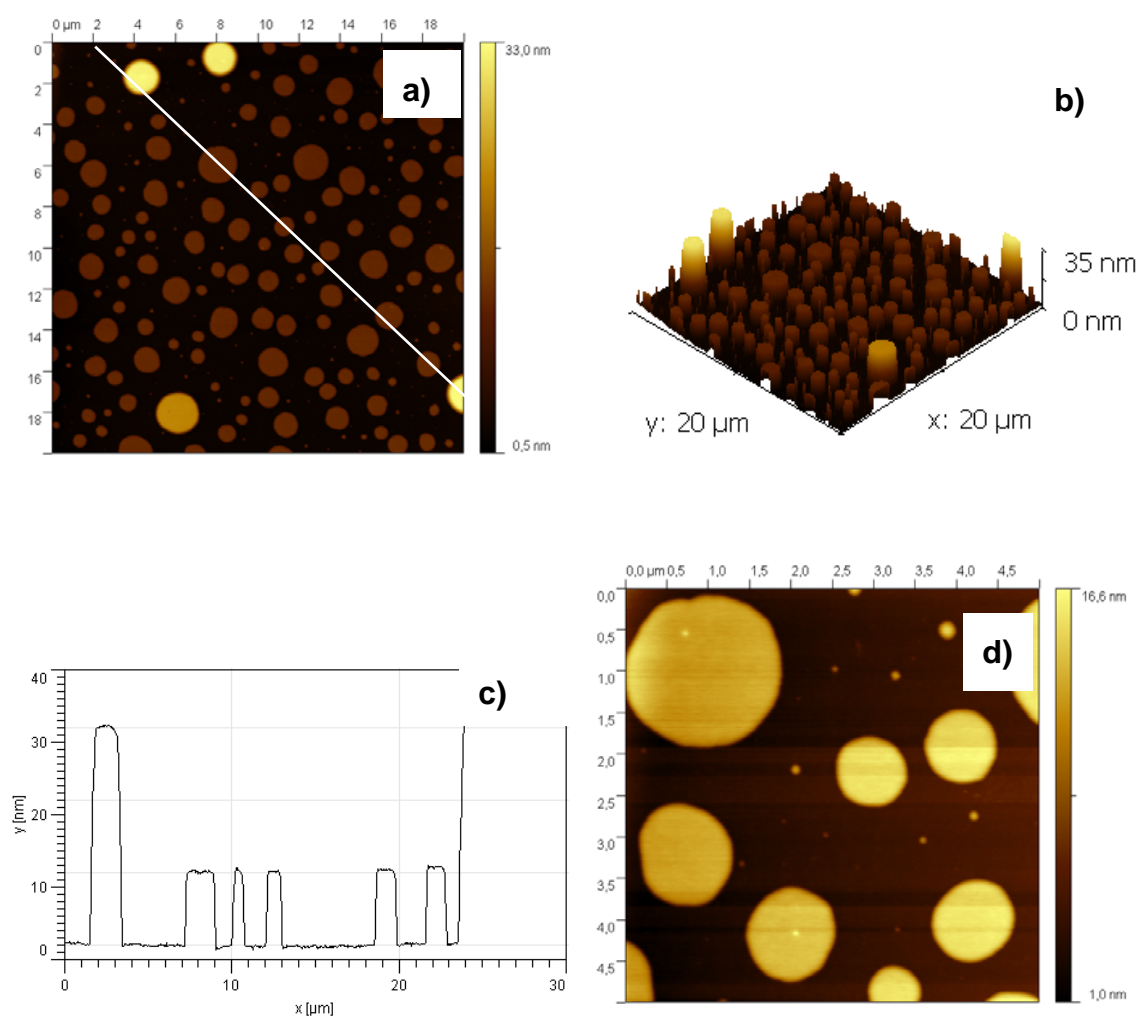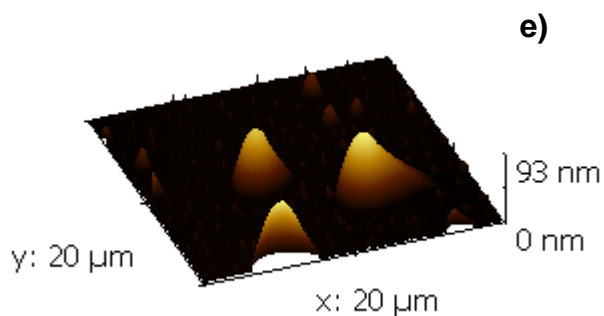
Figure 4.5: (a) AFM image of the PEO$_{19}$-*b*-PIB$_{130}$ block copolymer transferred at the surface pressure of 35 mN/m. (b) Corresponding 3D image of PEO$_{19}$-*b*-PIB$_{130}$. (c) Height profile taken along the line in (a). (d) AFM image of PEO$_{19}$-*b*-PIB$_{130}$ taken at another LB film area. (e) 3D image of PEO$_{19}$-*b*-PIB$_{130}$ LB film after storing for 4 weeks at room temperature.

Figure 4.6 illustrates schematically the behavior of PEO$_{19}$-*b*-PIB$_{130}$ on the solid support assuming polymer chains close to crystalline (mesomorphic) packing. The PEO chains are uniformly adsorbed on the silicon wafer surface. The extended chains with the length of 300 Å consist of 130 PIB units. The smallest columns have a height of 100 Å which is an indication for two chain folds. Analogous considerations with one chain fold lead to a height of approximately 150 Å.

PIB unit cell

18.60 Å

2.33 Å

300 Å

150 Å

100 Å

Figure 6: Schematic representation of the structure of PEO$_{19}$-*b*-PIB$_{130}$ copolymer after transfer at 35 mN/m. The 8$_3$ helix and the PIB unit cell are also shown in the upper left part of the figure.[154]

Assuming a length of 2.33 Å per PIB monomer unit, approximately 8-9 units are necessary for a total Langmuir film thickness of 20 Å and ~ 13 units are necessary for 30 Å. In this range, the water surface is covered with PEO_{19}-b-PIB_{130} on the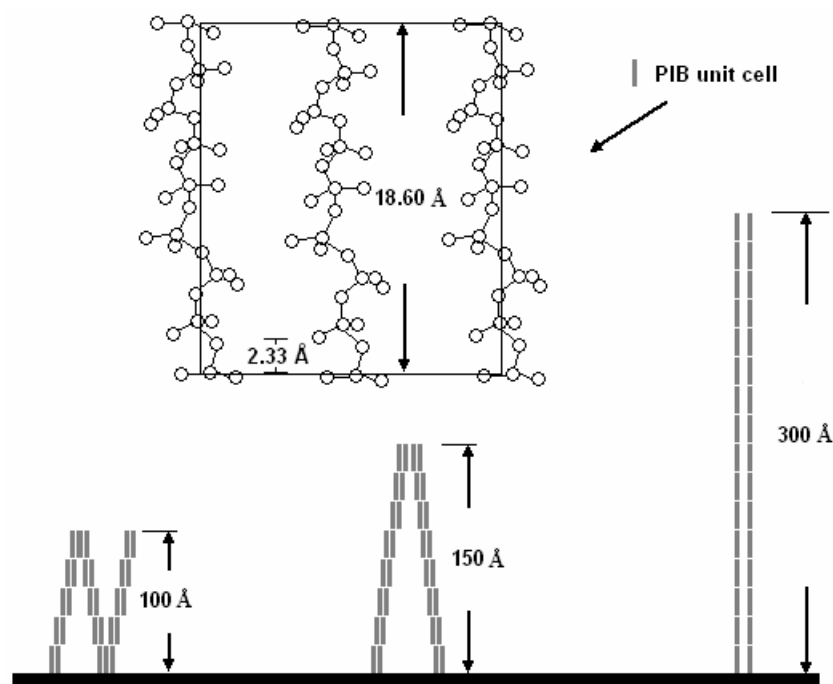 Langmuir trough at surface pressures of 15 mN/m and above. Films with an average thickness of 20 Å (surface pressure of 15 mN/m) are transferred to the solid substrate showing the locally formed mesomorphic phases with a disordered surrounding (Figure 4.4a). But if a film with an average thickness of 30 Å (surface pressure of 35 mN/m) or above is transferred, the PIB reorganizes completely to the columnar mesomorphic phase. The PIB chains now form a solid-like arrangement. This can be considered as the large-scale formation of the PIB mesomorphic phase. It can only be the result of the film transfer process since there is no polymer between the columns shown in Figure 4.5a detectable by AFM scratching experiment. If this structure would be formed at the air/water interface, in relaxation experiments an Avrami like behavior with exponents larger than one would be expected in addition to a large compressibility.[167] But only a slight relaxation (Avrami exponent ~ 0.5) with an mmA decrease less than 10 % is observed. It can be assumed that the formation of the columns is supported by repulsive interactions caused by the much larger surface energy of the SiO_2 surface (several hundred mN/m) compared to water.[171] Thus the film transfer is in conjunction with an increase of the repulsive interactions between the hydrophobic PIB blocks and the subphase. This supports obviously the parallel arrangement of PIB chains in the mesomorphic phase.

Figure 4.7a and b show the AFM height and phase images of the multilayer of PEO_{19}-b-PIB_{130} transferred at 35 mN/m. Ten layers were deposited on the hydrophilic silicon substrate using the dip coating technique. A complete coverage of the block polymer on the silicon wafer was observed in Figure 4.7b. The image shows also columns that are formed by several steps. It indicates that once the columns are formed they nucleate the next column with a smaller diameter on top (around three layers). This is again a strong indication for the formation of a mesomorphic phase. These multi-step columns reach heights of ~ 300 to 500 Å. This is an agreement with previous experimental findings that only two or three top layers form mesomorphic structures in multilayer PIB films deposited from the water surface on silicon substrates.[161] The AFM images also indicate that the material used for column formation is dragged away from the surrounding of the LB film. The surrounding does not show any structuring which might be taken as an indication that the Langmuir film on the water surface was a smooth film of PIB with an extended brush region of PEO in the water subphase.
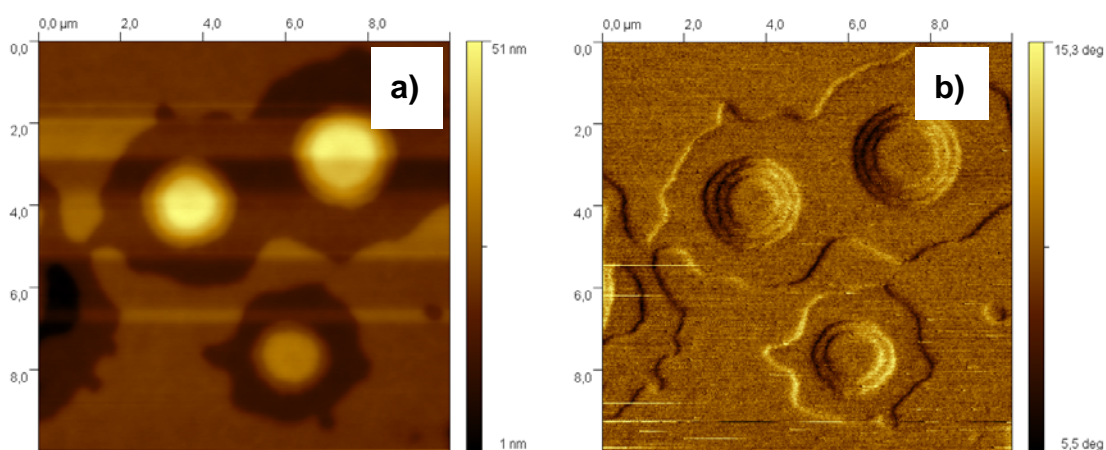
Figure 4.7: (a) AFM image of PEO$_{19}$-b-PIB$_{130}$ multilayer transferred at 35 mN/m. (b) Phase image of (a).

Figure 4.8a shows the AFM image of a layer of Fe$_2$O$_3$-NPs mixed with PEO$_{97}$-b-PIB$_{37}$ (FeNPEB) and transferred to silicon at a surface pressure of 15 mN/m. Many bright spots on top of the finger-like PEO crystals are observed. The finger-like structures have previously been explained as PEO crystals. Note that the surface pressure at transfer is only 15 mN/m compared to 45 mN/m used in order to obtain the morphology shown in Figure 4.3a. However, the bright spots on top of the PEO crystals can be caused by the PIB block and nanoparticles. A magnification is shown in Figure 4.8b which is taken within the square drawn in Figure 4.8a. Figure 4.8c shows its corresponding 3D image. Its corresponding phase image (Figure 4.8d) indicates very clear that Fe$_2$O$_3$-NPs are located on top of the PIB phases. The nanoparticles on top of the PIB phase form clusters of several nanoparticles. It is reasonable that the hydrophobic oleic acid shells of the nanoparticles have an affinity to the hydrophobic PIB domains. So a hierarchical ordering can be assumed with PEO crystals on the silicon wafer, with PIB phases on top of these crystals and finally the nanoparticles arranged on top of the PIB domains due to attractive hydrophobic interactions. Similar results have been obtained also by carrying out the transfer at higher surface pressure (35 mN/m). Thus several ordering phenomena contribute to the final morphology schematically drawn in Figure 4.9. The compression isotherms reveal that after spreading the mixture and evaporation of the chloroform, block copolymer molecules and nanoparticles float on the water surface. Due to hydrophobic attractive forces, PIB blocks and oleic acid ligands interact. At pressures below 40 mN/m the nanoparticles contribute significantly to the surface covering (see Figure 4.2), but with further compression, the nanoparticles are squeezed out of the layer to the top of the PIB phase and finally the hierarchical structure is formed.
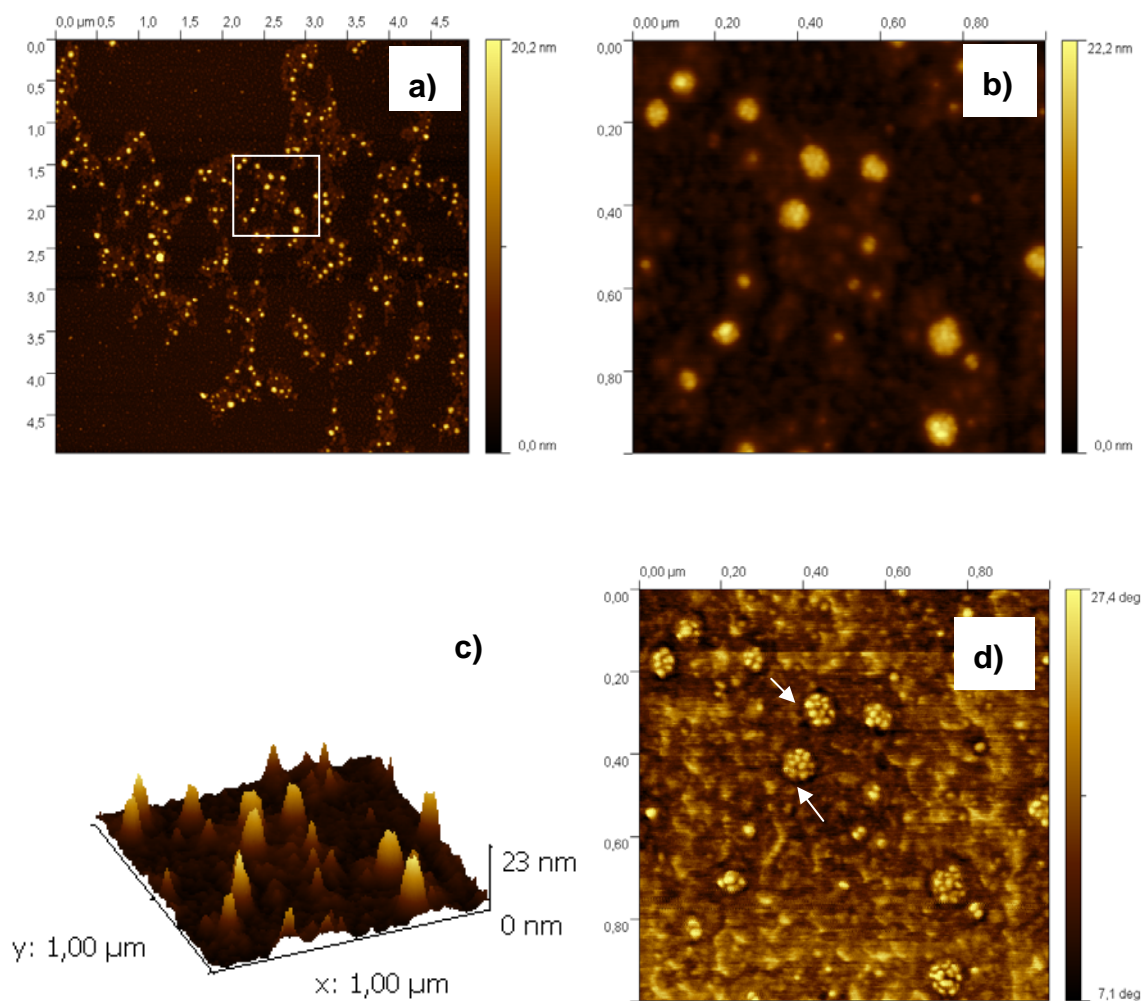
Figure 4.8: (a) AFM image of FeNPEB transferred at 15 mN/m. (b) AFM image of the magnification of the region marked with a square in (a). (c) Corresponding 3D image of (b). (d) Phase image of (b) with nanoparticles indicated by arrows.
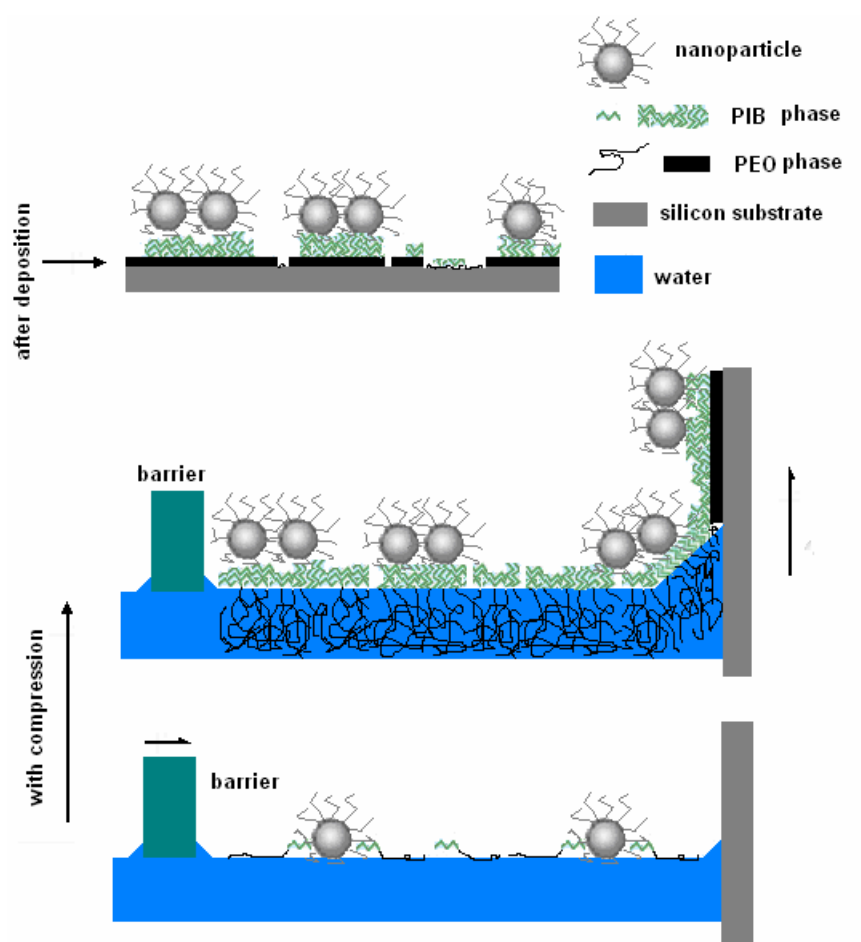
Figure 4.9: Schematic representation of PEO_{97}-b-PIB_{37} block copolymer mixed with Fe_2O_3-NPs (FeNPEB) on the water surface and the silicon substrate.

4.4   Conclusions

Amphiphilic block copolymers of poly(ethylene)-*block*-poly(isobutylene) and their mixture with iron oxide nanoparticles were studied by using Langmuir isotherms on the water surface and atomic force microscopy after transfer to solid supports. The Langmuir isotherm of PEO_{97}-b-PIB_{37} shows a plateau at 10 mN/m, which corresponds to the dissolution of PEO blocks into water subphase. The isotherm of neat nanoparticles shows a gas-liquid transition. From the calculation of the mmA value of the transition, the Fe_2O_3 core is supported by extended oleic acid chains at the air/water interface. The isotherm of a mixture of nanoparticles with PEO_{97}-b-PIB_{37} shows only the plateau of PEO entering into the water subphase and the collapse of the monolayer.

The AFM image of LB films of PEO_{97}-b-PIB_{37} shows both finger-like morphology of PEO crystals and separate PIB phases after transfer from the water surface at a surface pressure of 45 mN/m. The height of the PIB domains of ~ 90 Å indicates that PIB chains are oriented perpendicular to the surface on top of PEO crystals. The AFM image of PEO_{19}-b-PIB_{130}

shows a rather disordered phase with some bright spots in between when transferred at 15 mN/m. Only PIB columns with discrete heights of 100 Å, 150 Å, and 300 Å, respectively, can be seen after the transfer at 35 mN/m. This can be assigned to a mesomorphic arrangement of PIB chains in columns having no chain folds (300 Å), one chain fold (150 Å) and two chain folds (100 Å). In contrast to other morphologies discussed in literature, this unique feature of PEO-*b*-PIB is the result of the high mobility of PIB chains and their ability to adopt a helical conformation. In order to study the exact arrangement of PIB chains (i.e. mesomorphic phase or crystal and helix or all-trans conformation) during compression on the Langmuir trough and in the LB films it will be necessary to carry out GI-WAXS and IRRAS measurements.[159,160] After the transfer to silicon the nanoparticles are located on top of the PIB phases of the block copolymer as a result of hydrophobic interactions between PIB and the alkyl groups of the oleic acid ligands of the Fe_2O_3 core (see Figure 4.9).

Chapter 5

Investigation of silica nanoparticles formation at the air/water interface

5.1   Introduction

Silica nanoparticles can be prepared by the so-called Stöber process by adding tetraethylorthosilicate to alkaline mixtures of alcohols (usually ethanol or methanol) with water.[172] The mechanism involving the two steps of hydrolysis and polycondensation has been summarized by Klein and by van Blaaderen et al. yielding narrowly distributed silica nanoparticles.[173,174] Basically, two different models for the generation of monodisperse silica particles have been proposed, one involving a nucleation and a (rate-limiting) particle growth by subsequent monomer-addition, the other model proposes particle growth via controlled aggregation of small nanometer-sized subparticles. More recently, this process has been used in the presence of low molar mass surfactants or amphiphilic block copolymers.[175,176,177,178] The idea is that the ordered surfactant (polymer) phases in aqueous solutions can be used as template and after calcination at elevated temperatures ordered silica materials are obtained again with several potential applications as e.g. catalysts supports, photonic thin films or monoliths for HPLC.[179,180,181] Furthermore, TEOS and its derivates with one covalently bound phospholipid are used to form a silica shell at the outside of polymersomes or liposomes (cerasomes).[182,183,184,185] Additionally, Langmuir compression isotherms of hydrophobically modified TEOS (having e.g. one octadecyl substituent) or modified TMOS (tetratmethylorthosilicate) have been measured, but a possible chemical reaction and the morphology development have not been studied.[186,187] Thus, it seems to be a reasonable concept to study the in situ silica nanoparticle formation from TEOS in the presence of amphiphiles at the air/water interface. The Langmuir technique can be used to spread mixtures of TEOS and the phospholipid 1,2-dipalmitoyl-sn-glycero-3-phosphocholine in chloroform onto the air/water interface. Then DPPC forms a stable monolayer templating the silica nanoparticles. The resulting morphologies are studied by atomic force microscopy (AFM) after transferring the films from the water surface onto silicon substrates by dip-coating.

5.2   Experimental section

5.2.1 Materials

Tetraethylorthosilicate (GC grade) was purchased from Fluka and used as received. The phospholipid 1,2-dipalmitoyl-*sn*-glycero-3-phosphocholine (DPPC) was obtained from Avanti Polar Lipids (Alabaster, AL) and used without further purification. The chemical structure of TEOS and DPPC are shown in Chart 5.1a and b.
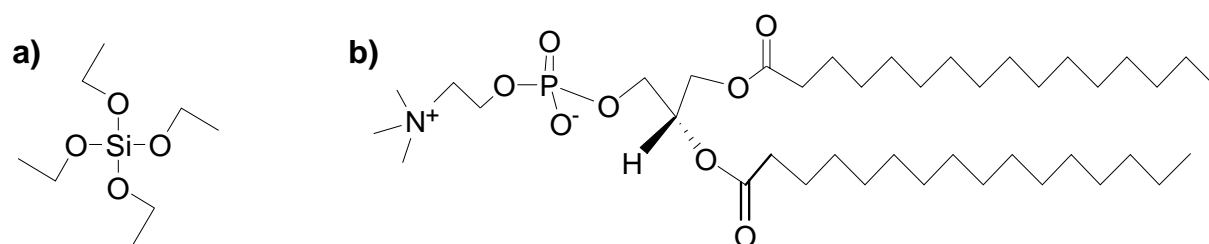
Chart 5.1: Chemical structure of (a) TEOS and (b) DPPC.

TEOS/DPPC mixtures were dissolved in chloroform (HPLC grade). Chloroform was used since it was a good solvent for both molecules. Mixtures of TEOS/DPPC were prepared with two different molar ratios. TEOS/DPPC (15:1 mol/mol) was obtained by adding 2.85 µL TEOS to 1 mL DPPC/chloroform solution (0.868 mM). When 9.6 µL TEOS was added to 1 mL DPPC/chloroform solution (0.868 mM), TEOS/DPPC (50:1 mol/mol) was obtained. When 0.4 mL TEOS and 0.26 mg DPPC were added in 1.6 mL chloroform, a molar ratio of TEOS/DPPC of 5000:1 was obtained. After placing droplets of the mixture solution on the water surface, the droplets are self-propelled and they move across the Langmuir trough. This effect is predominantly caused by the evaporation of chloroform. Finally TEOS tends to accumulate at the Teflon walls of the Langmuir trough and minor parts form domains on the water surface. The compositions and concentrations of the sample solutions are shown in Table 5.1.

Table 5.1: Composition and concentration of sample solutions.

TEOS : DPPC [mol:mol]	Concentration of TEOS [mM]	Concentration of DPPC [mM]	Volume of spreaded solution [µL]
15 : 1	13	0.868	61
50 : 1	43	0.868	61

The subphase was prepared by adding a defined amount of ammonia solution (1 µL) to double distilled water (~1 L) to change the pH value of the subphase to 9. Unlike the classical Stöber approach,[172] the addition of alcohols to the subphase is avoided since they may disturb the DPPC layer. This modified method was already described and used by Hubert et al. for modification of liposomes with TEOS.[188]

5.2.2 Time-dependent surface pressure measurements

Surface pressure measurements were carried using a Langmuir trough (KSV, Helsinki) keeping the surface area constant at 150 cm^2 which resulted in plots of π versus time. The temperature of the water subphase was maintained at 20 °C using a circulating water bath system. 61 µL solutions of TEOS and DPPC in chloroform were spread onto the water surface by using a microsyringe (Hamilton). The experimental data were recorded after 10 min to ensure the full evaporation of chloroform and uniform diffusion of molecules on the water surface. The experimental setup was placed in a Plexiglas hood in order to keep a constant humidity and minimize the dust particles.

5.2.3 Surface film deposition

The dip-coating technique was performed to transfer the films from the water surface onto the hydrophilic silicon substrates. The surface area of the trough was kept constant at 150 cm^2 by fixing two barriers. 61 µL mixture of TEOS/DPPC was spread on the water surface. Silicon substrates were cut into 25 mm × 15 mm and cleaned with double distilled water and CO_2 dry snow jet. After this treatment a clean hydrophilic SiO_2 surface was obtained. For dip-coating, the silicon wafers were submersed into the water subphase before spreading the sample solution. After ~21 h of reaction time at the air/water interface for each measurement, the films were transferred onto the substrates by vertical uptake through the films using a constant rate of 1 mm/min. The transferred films were allowed to dry in a desiccator at the room temperature for 48 h. After that, the morphology of the surface films were detected by AFM (equipment details see 4.2.4)

5.3 Results and discussion

5.3.1 Surface pressure versus time measurements

TEOS/DPPC 15:1 (mol/mol) and TEOS/DPPC 50:1 (mol/mol) are dissolved in chloroform. These solutions are spread onto the water surface of a Langmuir trough. Fig. 5.1 shows time-dependent surface pressure (π) measurements which are started after 10 min in order to allow the chloroform to evaporate. After spreading of TEOS/DPPC 15:1 the surface pressure reaches an initial value of ~26.2 mN/m indicating a homogenous DPPC layer at the air/water interface. The surface pressure decreases only slightly to ~24.4 mN/m after a reaction time of ~21 h. During this reaction time, the surface pressure shows some fluctuations obviously related to the hydrolysis of TEOS and silica particle formation on the water surface. During the polycondensation process the hydrophobic TEOS molecules are converted to hydrophilic silica particles via intermediate amphiphilic silanols. These processes lead to a decrease of the surface area required by the final silica particles compared to the initial TEOS molecules. Furthermore, the π-mean molecular area (mmA) isotherm of DPPC measured at 20 °C has been reported by McConlogue et al.[189] Using this isotherm and the DPPC concentration used in our experiments, an mmA value of 48 Å^2 with a π-value of ~42 mN/m would be obtained. (The calculation details: In the precursor solution of TEOS/DPPC 15:1, under the assumption that only the DPPC was spread on the water surface the mmA of DPPC can be calculated: $(0.868 \times 10^{-3}$ mol/L) $\times$ $(61 \times 10^{-6}$ L) = 53×10^{-9} mol; $(53 \times 10^{-9}$ mol) $\times$ (6.022×10^{23})= 318×10^{14} (the number of DPPC molecules on the water surface); 150 cm^2 / (318×10^{14})= 48 Å^2 (mmA of DPPC)). This value is far larger than the initial surface pressure of ~26.2 mN/m after spreading of TEOS/DPPC 15:1. Thus, it can be assumed that parts of DPPC do not cover the water surface but remains as inverse micelles or dispersed single molecules in the hydrophobic excess of TEOS and will finally be used to stabilize the silica particles. Assuming a homogeneous TEOS layer on the water/DPPC surface, an average layer thickness of ~11.7 nm is obtained (The calculation details: Under the assumption that pure TEOS was spread on the water surface, the thickness of the surface film can be calculated using the molar concentration of 13×10^{-3} mol/L (0.868×10^{-3} mol/L $\times$ 15), the spread volume of 61×10^{-6} L, the density of TEOS and the surface area of the trough: $(13 \times 10^{-3}$ mol/L) $\times$ $(61 \times 10^{-6}$ L) = 793×10^{-9} mol; $(793 \times 10^{-9}$ mol) $\times 208$ g/mol = 164944×10^{-9} g (the mass of the spread TEOS); $(164944 \times 10^{-9}$ g) / 0.94 g/cm^3 = 175472×10^{-9} cm^3 (the volume of spread TEOS); $(175472 \times 10^{-9}$ cm^3) / 150 cm^2 = 117 Å (the thickness of TEOS on the water surface if it is completely spread)). It should be mentioned that the amount of ethanol formed after complete conversion would be ~3.2 μM. This is negligible with respect to the surface pressure since a Langmuir trough with 1250 mL water is used (additionally ethanol has a higher vapor pressure compared to water). The surface pressure versus time of TEOS/DPPC 50:1 at the air/water interface is also shown in Fig. 5.1. The initial surface pressure reaches the value of

~29.4 mN/m followed by a decrease to ~28 mN/m after 21 h reaction time. The higher initial π-value compared with that of TEOS/DPPC 15:1 can be attributed to the larger amount of TEOS spread on the water surface since the amount of DPPC is fixed for both mixtures. In order to obtain more information of the morphology, AFM images are taken from transferred films obtained by dip-coating with the transfer rate of 1 mm/min using hydrophilic silicon substrates.
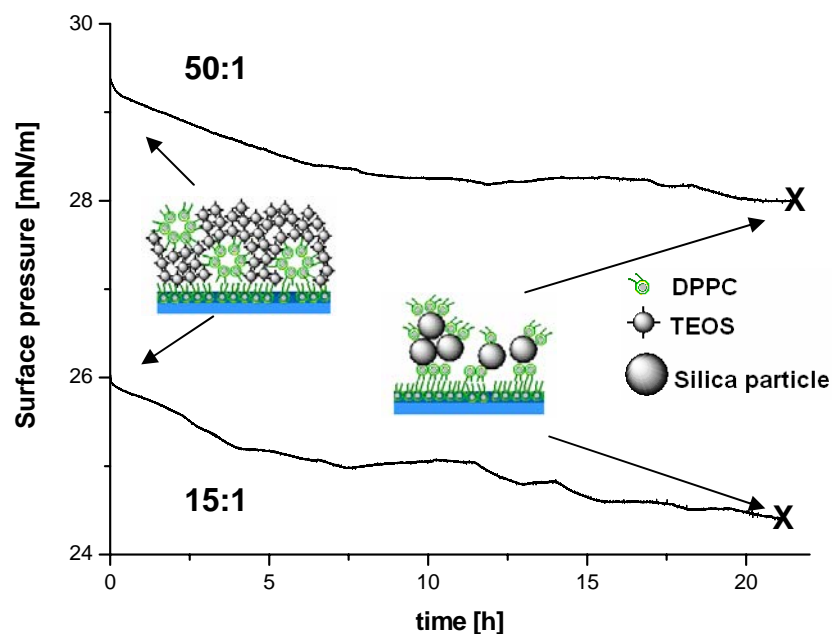
Figure 5.1: Time-dependent surface pressure measurements of two different TEOS/DPPC mixtures (50:1 and 15:1) after spreading on the water surface. Surface films are transferred at the surface pressure indicated by **X**.

5.3.2   AFM study

The AFM image of the mixture of TEOS/DPPC 15:1 after ~21h reaction time and transfer is shown in Fig. 5.2a. Nanoparticles (indicated by arrows) embedded in a DPPC environment can be detected. Furthermore, larger nanoparticle aggregates having a height of ~6 to 8 nm and a diameter of ~ 50 nm can be seen (Fig. 5.2b). In this experiment 0.8 µM silica can be generated on the water surface if TEOS is completely converted. Assuming a uniform silica film, this would result in a thickness of 1.22 nm (The calculation details: The chemical reaction can be summarized as below:

$$Si(OC_2H_5)_4 + 2\ H_2O \rightarrow 4\ C_2H_5OH + SiO_2 \tag{5.1}$$

793×10^{-9} mol SiO_2 is generated from the precursor solution of TEOS/DPPC (15:1 mol/mol) after complete conversion. (793×10^{-9} mol) $\times$ 60 g/mol = 48×10^{-6} g (the mass of silica generated); 48×10^{-6} g / 2.6 g/cm^3 = 18.5×10^{-6} cm^3 (the volume of generated silica); 18.5×10^{-6} cm^3 / 150 cm^2 = 12.2 Å (the thickness of a proposed homogeneous silica film on the water surface)). The AFM images do not show a uniform silica film, but single and aggregated particles with heights between 1 and 10 nm. Thus, from a rough estimation it can be assumed that all (or most) of the formed silica remains at the air/water interface. Fig. 5.2c shows the AFM image of the mixture of TEOS/DPPC 50:1 after ~21 h reaction time and transfer. Interconnected silica agglomerates embedded in a DPPC environment are visible. The respective phase image of a magnified region is shown in Fig. 5.2d. The height of the agglomerates is ~10 to 12 nm with a diameter of ~80 nm. The agglomeration is obviously caused by the larger TEOS concentration in the precursor solution. Not only the total coverage of DPPC on the substrate, but also dark areas surrounding the agglomerates can be observed clearly. In tapping mode AFM, the bright regions are caused by hard phases and, on the contrary, soft phases appear dark. Thus, the dark phase surrounding the silica particles can be assigned to DPPC molecules. Also on top of the agglomerates DPPC domains can be observed (see arrows). Roiter et al. have reported that nanoparticles having a diameter larger than 22 nm can be completely enveloped by DMPC (dimyristoylphosphatidylcholine).[190] Fig. 5.2e-h show transferred mixtures of TEOS and DPPC with a very large excess of TEOS. A Langmuir isotherm is not obtained since TEOS does not spread homogeneously on the water surface. However, in areas where silica is formed, large clusters similar to mesoporous silica gels are formed,[191] detecting single particles in the 3D image of Fig. 5.2h. The phase contrast image in Fig. 5.2g shows DPPC domains (see arrows) in the liquid condensed state (similarities with 'triskelions').[192]
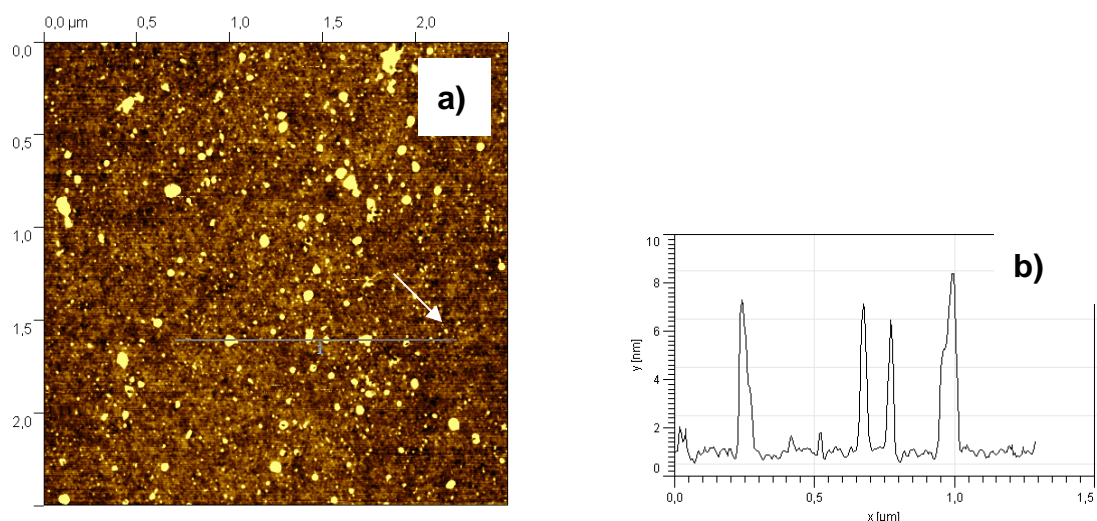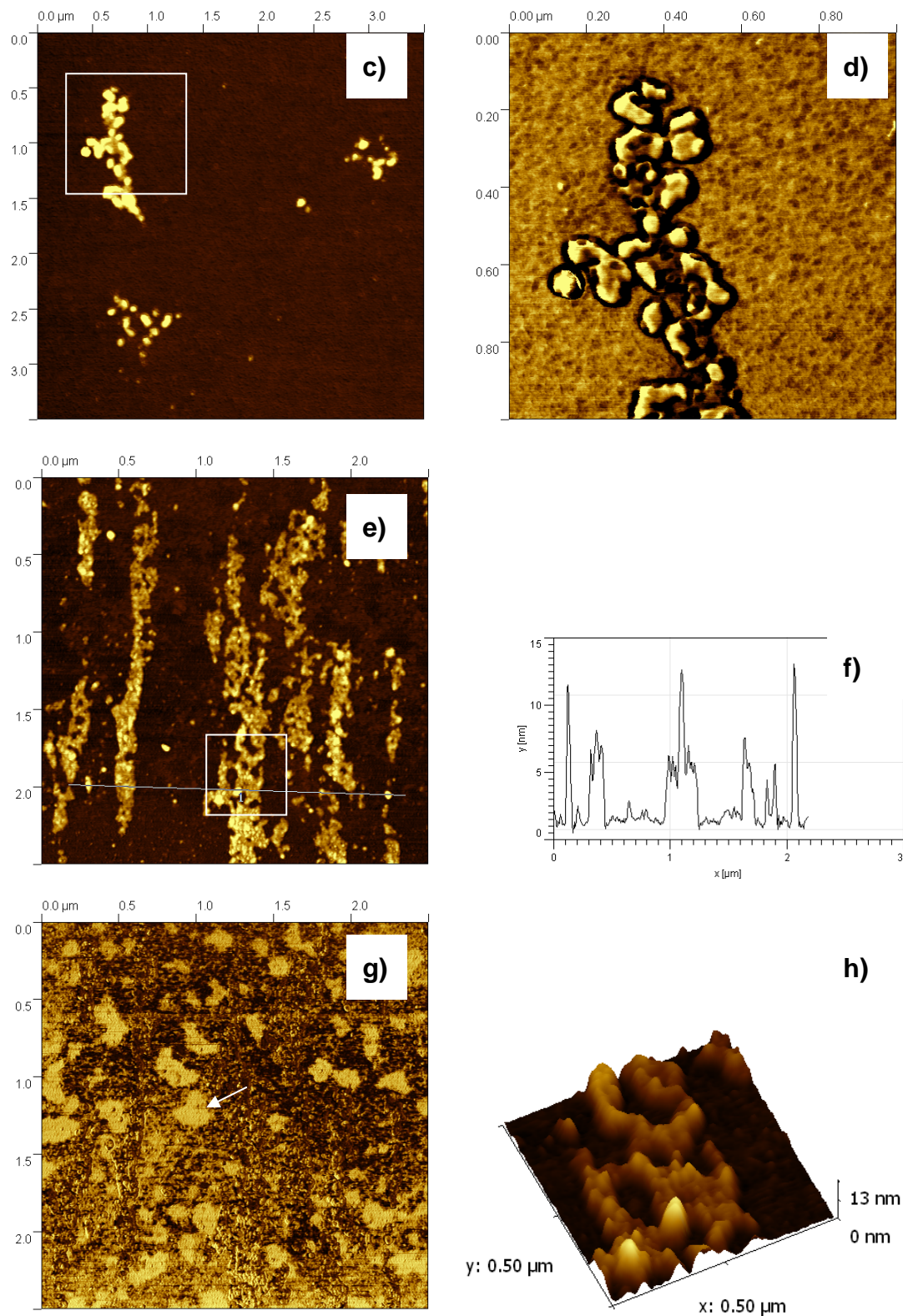
Figure 2: (a) AFM image of the mixture of silica/DPPC (from TEOS /DPPC 15:1 mol/mol) after transfer to silicon wafer. (b) Height profile taken along the line in (a). (c) AFM image of the mixture of silica/DPPC (from TEOS /DPPC 50:1 mol/mol) after transfer to silicon wafer. (d) Phase image of the magnified region marked with a square in (c). (e) AFM image of the mixture of silica/DPPC (from TEOS /DPPC 5000:1 mol/mol) after transfer to silicon wafer.

(f) Height profile taken along the line in (e). (g) Phase image of (e). (h) 3D image of the magnified region marked with a square in (e).

5.4   Conclusions

In conclusions, for the first time TEOS/DPPC mixtures are studied at the air/water interface. These first studies prove the possibility to create *in situ* silica nanoparticles and domains of nanoparticles using the polycondensation process of TEOS. Moreover, the simultaneous observation of aggregates and small particles indicate that the Stöber process may follow the route of nm-size subparticle aggregation. Further studies should aim to achieve ordered nanoparticles arrays as well as obtaining a deeper insight into the mechanism of particle formation (see Chapter 6).

Chapter 6

Summary and perspectives

Fertilizers in the broadest sense are products that improve the levels of available plant nutrients and/or the chemical and physical properties of soil, thereby directly or indirectly enhancing plant growth, yield, and quality. However, most of fertilizers have the tendency to form lumps or agglomerates during storage and transportation. Between the time of production and the final application, fertilizers must be stored, either in package or in bags, vary from one month to a year or more. The caked fertilizers not only result in the loss of nutrition and energy due to de-agglomeration process, but are fertilized difficultly by the fertilizer drill. Therefore, a quality fertilizer should be as free flow, dust free, and non-hygroscopic as possible. The main reasons for fertilizer caking are solid bridge (crystal bridge) formation between granules due to they were dissolved and re-crystallized (phase contact) during storage, as well as molecule attractive force which results from the pressure (adhesion contact) on the fertilizer granules. Nowadays, the popular and effective method to avoid the caking is to coat an anti-caking agent on the fertilizer surface. The anti-caking agents are divided into surface active type and non-surface active type.

In this study, surface active anti-caking solutions were investigated and their effects on the urea granules were measured. The solutions used in this work mainly include a surface active agent (surfactant), a water soluble polymer and a nitrification inhibitor. CMC values of surfactants were measured at 10, 25 and 40 °C with the aid of surface tension measurements. PE6, PE8, and F8 had the CMC values in the scale of 10^{-7} mol/L. T series product and F9 had the CMCs in the scale of 10^{-6} mol/L. Depending on the chemical structure of T series products (they have the same hydrophilic block), their CMC values decreased with the increase of carbon atoms of hydrophobic chain. The temperature-dependent CMC measurements were done to obtain the thermodynamic properties of surfactants. T8 had the smallest change of CMC values under different temperatures reflecting its most stable surface activity. Surface tensions of PS and PSN solutions were measured at 10, 25 and 40 °C using the Wilhelmy plate method. The T2- and T8-anti-ckaing solutions had the lowest values of surface tension, i.e. ~29 mN/m at 40 °C, ~32 mN/m at 25 °C, ~35 mN/m at 10 °C. On the contrary, the F8-anti-caking solution had the highest surface tension. Furthermore, surface tensions of F8-, B3-, PE6- and PE8-anti-caking solutions increased when NI were added into solutions. It is reason that the hydrogen bonds were formed between NI and water. The dehydration of hydrophilic part of surfactant and with water happened leading to the

micellization of surfactants. Thus, surface activities of surfactants lowered. Viscosities and densities of PS and PSN solutions were measured at 25 °C and 40 °C. Although the viscosities and densities of various surfactants were quite different, only 1 % concentrations of surfactants prepared in solutions did not influence the viscosity and density values of PS and PSN solutions.

After obtaining some physical chemistry properties of anti-caking solutions, they were coated on the urea granules and anti-caking effects of coating solutions were investigated. Solutions were coated on the granules at the room temperature using a shake machine and dried at 40 °C in the drying oven. After two days storage, Karl Fischer Titration was carried out on coated granules after two days storage at the room condition to measure the initial water content. Granules coated with T8-anti-caking solution had the lowest water content, which led to the smallest tendency of caking. On the contrast, granules coated with F8-anti-caking solution had largest water content. The smaller water contents, the less caking tendency. These anti-caking solution coated granules were stored in DPS and MPS at two conditions, 25 °C, 85 % relative humidity for 3 days and 40 °C, 75 % relative humidity for 3 days. After that, both conditions changed into 25 °C, 30 % for another 2 days to dry granules. While granules were caked together in DPC and MPS, mechanical tests, i.e. tensile tests and free falling lump tests were done to measure the destroying loads for de-caking of two caked granules and weight of still caked granule after falling followed by the calculation of anti-caking ratio, respectively. Caked double-granules from DPS were measured using tensile tests. T8-anti-caking coated granules had the smallest destroying loads for de-caking the caked double-granules. However, F8-anti-caking solution coated granules had the highest destroying loads of breaking caked double-granules. Various technical PVA as candidates were prepared in anti-caking solutions and coated on the granules. From tensile tests of double-granules after coating and caking, with increase of hydrolysis degree of PVA used in the solution, a smaller destroying load (better anti-caking effect) was measured. It is the reason that a higher HD PVA has a lower solubility and more difficult soluble in water. Results of free falling lump tests of multi-granules after coating and caking confirmed that the coating solution prepared by higher HD PVA and T8 had a better anti-caking ability. VSN and PVSN solutions were also coated on granules. By the mechanical test, their anti-caking effects were not improved compared with PSN solutions used as coating agents. Furthermore, the varieties of concentrations of PVP used in PVSN solution did not induce the difference of destroying loads for de-caking PVSN coated double-granules by tensile tests. Light microscopy uncovered that the crystal bridge between T8-anti-caking solution coated granules was smaller than that of F8-anti-caking solution coated granules indicating a better anti-

caking effect of T8-anti-caking solution. Moreover, the surface morphology of uncoated urea granules and PSN coated granules were observed using ESEM. It is clear that anti-caking solutions were homogenously coated on the granules. The dried anti-caking agent can be observed and they dispersed uniformly on the granules surface. The needle-like crystals of NI could be seen on the granule surface. After tensile tests of caked double granules, the surface of fracture areas were observed using ESEM. Some pore structures were observed on the fracture area of T8-anti-caking solution coated granules after caking and tensile tests. A smoother and bigger fracture area of was observed on F8-anti-caking coated granules. It is believed that their crystals dissolved and re-crystallized more significantly during caking experiments. This smooth fracture area resulted from the dissolving of surface urea crystals and diffusing of dissolved surface parts into pores and hardening by their re-crystallization.

During the manufacture of fertilizer granules, the granules not only agglomerated each other, but caked on the production line. This can be attributed to either the coating solutions caked with production line after drying or granules re-crystallized on the production line. Tensile test was used to determine the caking between solutions coated metal plates, which is the same material as the production line. Various anti-caking solutions were placed on the metal plates, then after 3 days at 45 °C drying in the oven, two plates can be caked together. Depending on separation loads for separating the solution coated metal plates by tensile tests, with increase of hydrolysis degree of PVA used in the anti-caking solution, the adhesion (separation loads) between PSN coated plates became smaller in that adhesion of dried PVA solutions to smooth surfaces (metal foil and glass) improves with the lower degrees of hydrolysis. When VSN or PVSN were coated on plates, with increase of PVP concentration used in the solution, adhesions (separation loads) between plates were raised. Due to the hygroscopic property of PVP, after drying of PVSN and VSN solutions coated metal plates, they were easy to absorb the water from atmosphere leading to a stronger caking between solution coated plates. It can be assumed that in the industry production, granules coated with PVP solutions should be avoided in coating solution.

In term of all measurements in this study, PSN solution prepared by PVA with high hydrolysis degree and the surfactant of T8 was strongly recommended to be used in the anti-caking solution.

In the recent decade, magnetic nanoparticles are of considerable scientific interest due to their various applications. Many of these applications require nanoparticles to possess good chemical and physical stability and uniform size. The aggregation of nanoparticles coming from anisotropic dipolar attraction hinders their application and development. The smart method to prevent the aggregation of nanoparticles is to use the polymers or surfactants as

ligands or stabilizing agent. In this study, amphiphilic block copolymers of poly(ethylene)-*block*-poly(isobutylene) and their mixture with iron oxide nanoparticles were studied using Langmuir isotherms on the water surface and atomic force microscopy after transfer onto solid supports. The Langmuir isotherm of PEO_{97}-*b*-PIB_{37} shoeds a plateau at 10 mN/m corresponding to the dissolution of PEO blocks into water subphase, which was absent for the more hydrophobic block polymer of PEO_{19}-*b*-PIB_{130} and collapse at the surface pressure of 50 mN/m and mmA value of ~100 $Å^2$. The Langmuir isotherm of PEO_{19}-*b*-PIB_{130} showed the extensive plateau at the surface pressure of 40 mN/m reflecting the multilayer formation, the so-called roll over mechanism. The isotherm of neat nanoparticles showed a gas-liquid transition at the mmA value of 20470 $Å^2$. Using the mmA value of this transition, the Fe_2O_3 core supported by extended oleic acid chains at the air/water interface can be assumed. The isotherm of a mixture of nanoparticles with PEO_{97}-*b*-PIB_{37} showed only the plateau of PEO entering into the water subphase and the collapse of the monolayer.

The AFM image of LB films of PEO_{97}-*b*-PIB_{37} showed both finger-like morphology of PEO crystals and separate PIB phases after transfer from the water surface at a surface pressure of 45 mN/m. The height of the PIB domains of ~90 Å indicated that PIB chains were oriented perpendicular to the surface on top of PEO crystals. The AFM image of PEO_{19}-*b*-PIB_{130} showed a rather disordered phase with some bright spots in between when transferred at 15 mN/m. Only PIB columns with discrete heights of 100, 150 and 300 Å, respectively, can be seen after the monolayer was transferred at the surface pressure of 35 mN/m. This can be assigned to a mesomorphic arrangement of PIB chains in columns having no chain folds (300 Å), one chain fold (150 Å) and two chain folds (100 Å). In contrast to other morphologies discussed in literature, this unique feature of PEO-*b*-PIB was the result of the high mobility of PIB chains and their ability to adopt a helical conformation. After the transfer of surface film of the mixture of iron oxide nanoparticles with PEO_{97}-*b*-PIB_{37} onto the silicon substrate the nanoparticles were located on top of the PIB phases of the block copolymer as a result of hydrophobic interactions between PIB and the alkyl groups of the oleic acid ligands of the Fe_2O_3 core.

The silica nanoparticles can be prepared by the sol-gel process of TEOS using the template of a DPPC Langmuir film. After spreading of the mixture of TEOS/DPPC (in chloroform) on the water surface of a Langmuir trough, an initial increase of the surface pressure to ~26 to 29 mN/m followed by a decrease of ~2 mN/m within 21 h reaction time can be observed indicating the initial spreading of the TEOS/DPPC films on the water surface and the followed polycodensation process of hydrolyzed TEOS to silica domains. This was a result of total covering of the water surface by a film of silica with DPPC. Surface films of

silica/DPPC mixture were transferred from the air/water interface to silicon wafers by dip-coating. The morphologies of silica nanoparticles and the structure of liquid condensed DPPC were observed using tapping mode AFM. This is for the first time the formation of small size (1 to 10 nm) silica nanoparticles at the air/water interface using DPPC Langmuir film as the template. This study will be continued to achieve ordered nanoparticles arrays at the air/water interface as well as obtaining a deeper insight into the mechanism of particle formation (see future perspectives).

Future perspectives

Silica nanoparticles formation using sol-gel process is of an interest since 1960's by Stöber et al. Until now, most of silica nanoparticles were prepared using the Stöber process only in the water bulk followed by the deposition onto the silicon substrate for the applications, e.g. semiconductor manufacture, optoelectronic device and catalyst, etc. Furthermore, coating of TEOS onto silicon substrate using the plasma enhanced chemical vapor deposition for obtaining the silica films has been reported. These methods require either the exceed amount precursor solution in the water bulk or the very low processing pressure (few milli-Torr.) leading to a higher cost for preparation. The silica nanoparticles film formed on the water surface using TEOS precursor solution can both significantly decrease the amount of raw material used, and more convenient processing procedure and condition. As described in Chapter 5, the agglomerates of silica nanoparticles can be observed when higher concentration of TEOS was use in the precursor solution. Therefore, the aim of next step is to obtain the high ordered silica arrays and total coverage of silica film on the silicon substrate by adjusting the concentration of TEOS in the precursor solution or using different amphiphilic block copolymers (surfactants) as template. Furthermore, besides the dip-coating, layer-by-layer (LBL) can be used in order to a multilayer of silica particles on the substrate. After deposition of silica on the substrate, it can be calcinated at an elevated temperature, e.g. 550 °C for obtaining mesoporous structure and removing the polymer template.

Very importantly, IRRAS is able to monitor the reaction of TEOS precursor solution on the water surface at the molecular level. This is for the first time the surface chemistry instrument monitor an organic synthesis at the air/water interface. Some of IRRAS results from the time-dependence experiment of neat TEOS on the water surface have been obtained. The stretching of the Si-O-Si band at the frequency of 1072 cm^{-1} is detected indicating the formation of silica at the air/water interface. The decrease of the intensity of OH vibration at ~3500 cm^{-1} reflecting the polycondensation of hydrolyzed TEOS to silica nanoparticles.

Literature

1. Scherer, H.W.; Mengel, K. *Ullmann's Agrochemicals: Fertilizers* Wiley-Vch, **2007**.

2. Krase, N.W.; Gaddy, V.L. *Ind. Eng. Chem.* **1922**, *14*, 611-615.

3. Meessen, J.H.; Petersen, H. *Ullmann's Encyclopedia of Industrial Chemistry* VCH Weinheim, **1996**, *27*, 333-365.

4. Nelson, D.W.; Huber, D. *Nitrification Inhibitors for Corn Production* National Corn Handbook, **1992**, *55*.

5. Pratt, C.J.; Noyes, R. *Ureaform in Nitrogen Fertilizer Chemical Process* Noyes Development Corp, **1965**, 232-234.

6. Memgel, K. *Ernährung und Stoffwechsel der Pflanze* VEB Gustav Fischer Verlag, **1968**, 287-289.

7. Scheffer, B. *Gas Wasserfach: Wasser/Abwasser* **1994**, *135*, 15-19.

8. Schweiger, P. *Wege zur Minimierung des Nitratproblems* Proceedings, Stabilisierte Stickstoffdünger – ein Beitrag zur Verminderung des Nitratproblems, 15.-16. 10. **1991**, BASF Aktiengesellschaft, Limburgerhof/SKW Trostberg AG, **1991**, 59-69.

9. Sturm, H.; Buchner, A.; Zerulla, W. *Gezielterdüngen. Integriert, Wirtschaftlich, Umweltgerecht* Verlags Union Agrar., DLG-Verlags-GmbH, **1994,** 90-95.

10. Bronson, K.F.; Mosier, A.R. *Biol. Fertil. Soils* **1994**, *17*, 263-268.

11. Bronson, K.F.; Mosier, A.R. *Effect of Nitrogen Fertilizer and Nitrification Inhibitors on Methane and Nitrous Oxide in Irrigate Corn* Biochemistry of Global Change, Radiatively Active Trace Gases, Chapman & Hall **1993**.

12. Bronson, K.F.; Mosier, A.R.; Bishnoi, S.R. *Soil Sci. Soc. Am. J.* **1992**, *56*, 161-165.

13. Trenkel, M.E. *Controlled-Release and Stabilized Fertilizes in Agriculture* (FAO) IFA, **1997**.

14. Zacherl, B.; Amberger, A. *Fert. Res.* **1990**, *22*, 37-44.

15. Chickos, J.S.; Acree, W.E. *J. Phys. Chem. Ref. Data* **2002,** *31*, 537-698.

16. Rutland, D.W. *Fert. Res.* **1991**, *30*, 99-114.

17. Wahl, M.; Kirsch, R.; Bröckel, U.; Trapp, S.; Bottlinger, M. *Chem. Eng. Technol.* **2006**, *29*, 674-678.

18. Thompson, D.C. *Fertilizer Caking and Its Prevention* Proceedings, The Fertilizer Society, **1972**, *125*.

19. Kurshinnikov, I.N.; Chelikidi, G.F. *Methods of Eliminating the Caking of Fertilizer* Proceedings of the Soviet – Swedish Symposium on the Beneficiation of Phosphate Rock, **1978**, 180-186.

20. Rosenblom, J.; Zettervall, S. *Anti-caking Treatments of Granular Inorganic Salts Such as Phosphate Based Complex Fertilizer and Ammonium Nitrate* Proceedings of the Soviet – Swedish Symposium on the Beneficiation of Phosphate Rock, **1978**, 158-179.

21. Van Hijfte, W.H.P. *The coating of Straight Nitrogen Fertilizers* Proceeding of the 31st Annual Meeting of the Fertilizer Industry Round Table, **1981**, 181-187.

22. Walker, G.M.; Magee, T.R.A.; Holland, C.R.; Ahmad, M.N. *Ind. Eng. Chem. Res.* **1998,** *37*, 435-438.

23. Xu, J.; Shi, L.H.; Ye, M.L. *Chin. Chem. Lett.* **1997**, *8*, 1003-1004.

24. Goddard, E.D.; Philips, T.S.; Hannan, R.B. *J. Soc. Cosmetic Chem.* **1975**, *26*, 461-475.

25. Adams, J.R.; Merz, A.R. *Ind. Ing. Chem.* **1929**, *21*, 305-307.

26. Cisneros-Zevallos, L.; Krochta, J.M. *J. Food Sci.* **2003**, *68*, 503-510.

27. Jungerman, E. *Cationic Surfactants* Marcel Dekker, **1970**.

28. Rubingh, N.; Holland, P.M. *Cationic Surfactants – Physical Chemistry* Marcel Dekker, **1991**.

29. Schick, M.J. *Non-ionic Surfactant* Marcel Dekker, **1966**.

30. Schick, M.J. Non-ionic Surfactants: Physical Chemistry Marcel Dekker, **1987**.

31. Schoenfeldt, N. *Surface Active Ethylene Oxide Adducts* Pergamon Press, **1970**.

32. Tadros, T.F. *The Surfactants* Academic Press, **1984**.

33. Holmberg, K.; Jonsson, B.; Kronberg, B.; Lindman, B. *Surfactants and Polymers in Aqueous Solution* John Wiley & Sons, **2003**.

34. Lindman, B.; Wennerström, H. Micelles *Zopics in Current Chemistry* Springer-Verlag, **1980**.

35. Hartley, G.S. *Aqueous Solutions of Paraffin Chain Salts* Hermann and Cie, **1936**.

36. Rosen, M.J. *Surfactants and Interfacial Phenomena* John Wiley & Sons, **1992**.

37. Birdi, K.S. *Handbook of Surface and Colloid Chemistry* CRC Press Boca Raton, **1997**.

38. Evans, D.F., Wennerström, H. *The Colloidal Domain. Where Physics, Chemistry Biology and Technology Meet* Wiley-VCH, **1999**.

39. Tanford, C. The Hydrophobic Effect. Formation of Micelles and Biological Membranes Wiley, **1980**.

40. Shinoda, K. Principles of Solution and Solubility Marcel Dekker, **1974**.

41. Hay, J.M.; Lyon, D. *Nature* **1967**, *216*, 790-791.

42. Finch, C.A. *Polyvinyl alcohol-Development* John Wiley & Sons, **1992**.

43. Toyoshima, K. *General Properties of Polyvinyl alcohol in relation to its Applications*

John Wiley, **1973**.

44. Ŝtern, P.; Prokopová, E.; Quadrat, O. A. *Colloid Polym. Sci.* **1992**, *270*, 1066-1068.

45. Prokopová, E.; Ŝtern, P.; Quadrat, O.A. *Colloid Polym. Sci.* **1985**, *263*, 899-904.

46. Yu, Y-H.; Lin, C-Y.; Yeh, J-M.; Lin, W-H. *Polymer* **2003**, *44*, 3553-3560.

47. Yang, W.P.; Shyu, S.S.; Lee, E-S.; Chao, A-C. *Mater. Chem. Phys.* **1996**, *45*, 108-113.

48. Peppas, N.A.; Merrill, E.W. *J. Appl. Polym. Sci.* **1976**, *20*, 1457-1465.

49. Holland, B.J.; Hay, J.N. *Polymer* 2001, *42*, 6775-6773.

50. Hassan C.M.; Peppas, N.A. *Macromolecules* **2000**, *33*, 2472-2479.

51. Garnaik, B.; Thombre, S.M. *J. Appl. Polym. Sci.* **1999**, *72*, 123-133.

52. Gilman, J.W.; Kashiwagi, T.; VanderHart, D.L. *Polym. Mater. Sci. Eng.* **1994**, *71*, 28-29.

53. Guan, C.; Chen, D.; Tang, W.; Liu, C. *J. Appl. Polym. Sci.* **2005**, *97*, 1875-1879.

54. Minatti, E.; Norwood, D.P.; Reed, W.F. *Macromolecules* **1998**, *31*, 2966-2971.

55. El Gamal, S.; Borie, N.; Hammouda, Y. *Pharmazeutische Industrie* **1978**, *40*, 1373-1376.

56. Konno, H.; Taylor, L.S. *Pharm. Res.* **2008**, *25*, 969-978.

57. Warburton, S.A. PCT WO 2007-US20651 20070925 Int. Appl. **2008**, 56pp.

58. Philip, J.; Prakash, G.G.; Jaykumar, T.; Kalyanasundaram, P.; Mondain-Monval, O.; Raj, B. *Langmuir* **2002**, *18*, 4625-4631.

59. Fundin, J.; Brown, W. *Macromolecules* **1994**, *27*, 5024-5031.

60. Gandhi, H.; Mody, S.; George, A.; Jain, N.; Badhadur, P. *Tenside, Surfactants, Detergents* **2002**, *39*, 8-14.

61. Lysenko, E.A.; Bronich, T.K.; Slonkina, E.V.; Eisenberg, A.; Kabanov, V.A.; Kabanov, A.V. *Macromolecules* **2002**, *35*, 6351-6361.

62. Gasbarrone, P.; La Mesa, C. *Colloid Polym. Sci.* **2001**, *279*, 1192-1199.

63. Buzea, C.; Pacheco, I.I.; Robbie, K. *Biointerphases* **2007**, *2*, MR17-MR69.

64. Ataie, A.; Nikkhah-Moshaie, R. *Adv. Mater. Res.* **2008**, *55-57*, 569-572.

65. Uchida, M.; Terashima, M.; Cunningham, C.H.; Suzuki, Y.; Willits, D.A.; Willis, A.F.; Yang, P.C.; Tsao, P.S.; McConnell, M.V.; Young, M.J.; Douglas, T. *Magn. Reson. Med.* **2008**, *60*, 1073-1081.

66. Anthony, S.P.; Cho, W.J.; Lee, J.I.; Kim, J.K. *J. Mater. Chem.* **2009**, *19*, 280-285.

67. Hoang, V.V.; Odagaki, T.; Engel, M. *Appl. Surf. Sci.* **2008**, *254*, 7531-7534.

68. Tongcher, O.; Sigel, R.; Landfester, K. *Langmuir* **2006**, *22*, 4504-4511.

69. Milewski, P.D.; Lichtenwalner, D.J.; Mehta, P.; Kingon, A.I.; Zhang, D.; Kolbas, R.M. *J. Electron. Mater.* **1994**, *23*, 57-62.

70. Roduner, E. *Chem. Soc. Rev.* **2006**, *35*, 583-592.

71. Kouwenhoven, L.P.; Austing, D.G.; Tarucha, S. *Rep. Prog. Phys.* **2001**, *64*, 701-736.

72. Wang, J.F.; Gudiksen, M.S.; Duan, X.F.; Cui, Y.; Lieber, C.M. *Science* **2001**, *293*, 1455-1457.

73. Hu, J.; Li, L.; Yang, W.; Manna, L.; Wang, L.; Alivisatos, A.P. *Science* **2001**, *292*, 2060-2063.

74. Friedman R.S.; McAlpine M.C.; Ricketts D.S.; Ham D.; Lieber C.M. *Nature* **2005**, *434*, 1085.

75. Niemeyer, C.M. *Angew. Chem. Int. Ed.* **2001**, *40*, 4128-4158.

76. Borm P.J.A.; Robbins D.; Haubold S.; Kuhlbusch T.; Fissan H.; Donaldson K.; Schins, R.; Stone V.; Kreyling W.; Lademann, J.; Krutmann J.; Warheit D.; Oberdorster, E. *Part. fibre toxicol.* **2006**, *3*, 11.

77. Teja, A.S.; Koh, P. *Prog. Cryst. Growth Charact. Mater.* **2009**, *55*, 22-45.

78. Groenewolt, M.; Brezesinski, T.; Schlaad, H.; Antonietti, M.; Groh, P.W.; Ivan, B. *Adv. Mater.* **2005**, *17*, 1158-1162.

79. Brezesinski, T.; Groenewolt, M.; Antonietti, M.; Smarsly, B. *Angew. Chem. Int. Ed.* **2006**, *45*, 781-784.

80. Kallay, N.; Zalac, S. *J. Colloid Interface Sci.* **2002**, *253*, 70-76.

81. Brønsted, J.N. *Z. Physik. Chem.* **1922**, *102*, 169.

82. Christiansen, J.A. *Z. Physik. Chem.* **1924**, *113*, 35.

83. Farrell, D.; Cheng, Y.; Ding, Y.; Yamamuro, S.; Sanchez-Hanke, C.; Kao, C.; Majetich, S.A. *J. Magn. Magn. Mater.* **2004**, *282*, 1-5.

84. Spagnoli, D.; Banfield, J.F.; Parker, S.C. J. Phys. Chem. C 2008, 112, 14731-14736.

85. Lattuada, M.; Hatton, T.A. *Langmuir* **2007**, *23*, 2158-2168.

86. Chen, Y.; Cho, J.; Young, A.; Taton, T.A. *Langmuir* **2007**, *23*, 7491-7497.

87. Foerster, S.; Antonietti, M. *Adv. Mater.* **1998**, *10*, 195-217.

88. Fortina, P.; Kricka, L.J.; Surrey, S.; Grodzinski, P. *Trends Biotechnol.* **2005**, *23*, 168-173.

89. Willner, I.; Katz, E. *Angew. Chem. Int. Ed.* **2003**, *42*, 4576-4588.

90. Dinarvand, R.; Moghadam, S.H.; Sheikhi, A.; Atyabi, F. *J. Microencapsulation* **2005**, *22*, 139-151.

91. Umbreit, J.N.; Strominger, J.L. *Proc. Nat. Acad. Sci.* **1973**, *70*, 2997-3001.

92. Elworthy, P.H.; Macfarlane, C.B. *Solubilization by Surface Active Agents* Chapman & Hall, **1968**.

93. Istraelachvili, J. *Intermolecular and Surface Forces, with Special Applications to Colloid and Biological Systems* Academic Press, **1985**.

94. Flynn, D.J.; Kutay, S.M.; Hawrylak, B.E.; Kennedy, C.A.; Alexander, E.V.; Howard, J.A.; Marangoni, D.G. *Colloid Polym. Sci.* **2002**, *280*, 848-856.

95. Tadros, T.F. *Applied Surfactants, Principles and Applications* Wiley-VCH, **2005**.

96. Malik, W.U.; Jhamb, O. P. Kolloid Zeitschrift & Zeitschrift fuer Polymere **1970**, *242*, 1209-1211.

97. Zourab, Sh.M. *Alexandria Engineering Journal* **1996**, *35*, D85-D91.

98. Griffiths; P.C.; Roe, J.A.; Jenkins, R.L.; Reeve, J.; Cheung, A.Y.F. *Langmuir* **2000**, *16*, 9983-9990.

99. Bales, B. L.; Ranganathan, R.; Griffiths, P.C. *J. Phys. Chem. B* **2001**, *105*, 7465-7473.

100. Griffiths, P.C.; Cheung, A.Y.F.; Farley, C.; Fallis, I.A.; Howe, A.M.; Pitt, A.R.; Heenan, R.K.; King, S.M. ; Grillo, I. *Langmuir* **2004**, *20*, 7313-7322.

101. Tao, J.; Shivkumar, S. *Mater. Lett.* 2007, 61, 2325-2328.

102. Wahl, M.; Kirsch, R.; Broeckel, U.; Trapp, S.; Bottlinger, M. *Chem. Ing. Tech.* **2006**, *78*, 743-746.

103. Lafci, A.; Gürüz, K.; Yücel, H. *Fert. Res.* **1988**, *18*, 63-70.

104. Bröckel, U.; Wahl, M.; Kirsch, R.; Feise, H.J. *Chem. Eng. Technol.* **2006**, *29*, 691-695.

105. Walker, G.M.; Magee, T.R.A.; Holland, C.R.; Ahmad, M.N.; Fox, N.; Moffatt, N.A. *Nutr. Cycling Agroecosyst.* **1997**, *48*, 231-234.

106. Röck, M.; Ostendorf, M.; Schwedes, J. *Chem. Eng. Technol.* **2006**, *29*, 679-685.

107. Weigl, B.; Pengiran, Y.; Feise, H.J.; Röck, M.; Janssen, R. *Chem. Eng. Technol.* **2006**, *29*, 686-690.

108. Wang, Y.; Besant, R.W.; Evitts, R.W.; Dolovich, A.T. *Part. Part. Syst. Charact.* **2006**, *23*, 399-407.

109. Van Lamoen, F.L.J.; Borsten, H. *Anal. Chem.* **1955**, *27*, 1638-1639.

110. Rumpf, H. *Chem. Ing. Tech.* **1970**, *42*, 538-540.

111. Chibowski, S.; Paszkiewicz, M.; Wisniewska, M. *Adsorpt. Sci. Technol.* **2002**, *20*, 573-582**.**

112. Mamedov, A.A.; Kotov, N.A. *Langmuir* **2000**, *16*, 5530-5533.

113. Rodriguez-Parada, J.M.; Kaku, M.; Sogah, D.Y. *Macromolecules* **1994**, *27*, 1571-1577.
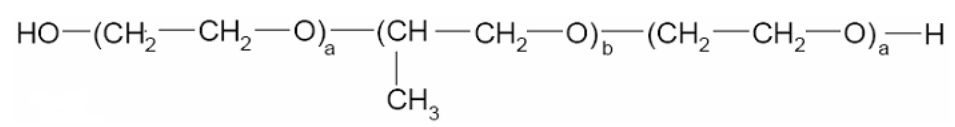
114.   Maenosono, S.; Okubo, T.; Yamaguchi, Y. *J. Nanopart. Res.* **2003**, *5*, 5-15.

115.   Xu, R.; Winnik, M.A.; Hallett, F.R.; Riess, G.; Croucher, M.D. *Macromolecules* **1991**, *24*, 87-93.

116.   Tuzar, Z.; Kratochvil, P. *Adv. Colloid Interface Sci.* **1976**, *6*, 201-232.

117.   Goncalves da Silva, A.M.; Filipe, E.J.M.; d'Oliveira, J.M.R.; Martinho, J.M.G. *Langmuir.* **1996**, *12*, 6547-6553.

118.   Sauer, B.B.; Yu, H.; Tien, C.F.; Hager, D.F. *Macromolecules* **1987**, *20*, 393-400.

119.   Faure, M.C.; Bassereau, P.; Lee, L.T.; Menelle, A.; Lheveder, C. *Macromolecules* **1999**, *32*, 8538-8550.

120.   Hussain, H.; Kerth, A.; Blume, A.; Kressler, J. *J. Phys. Chem. B* **2004**, *108*, 9962-9969.

121.   Gragson, D.E.; Jensen, J.M.; Baker, S.M. *Langmuir* **1999**, *15*, 6127-6131.

122.   Cheyne, R.B.; Moffitt, M. G. *Langmuir* **2005**, *21*, 5453-5460.

123.   Baker, S.M.; Leach, K.A.; Devereaux, C.E.; Gragson, D.E. *Macromolecules* **2000**, *33*, 5432-5436.

124.   Busse, K.; Peetla, C.; Kressler, J. *Langmuir* **2007**, *23*, 6975-6982.

125.   Reynolds, P.A.; McGillivray, D.J.; Gilbert, E.P.; Holt, S.A.; Henderson, M.J.; White, J.W. *Langmuir.* **2003**, *19*, 752-761.

126.   Schroeter, J.A. ; Plehnert, R. ; Tschierske, C.; Katholy, S.; Janietz, D.; Penacorada, F.; Brehmer, L. *Langmuir* **1997**, *13*, 796-800.

127.   Reiter, G.; Sommer, J.U. *J. Chem. Phys.* **2000**, *112*, 4376-4383.

128.   Sommer, J.U.; Reiter, G. *J. Chem. Phys.* **2000**, *112*, 4384-4393.

129.   Reiter, G. *J. Polym. Sci.* **2003**, *41*, 1869-1877.

130.   Reiter, G.; Castelein, C.; Sommer, J.U.; Rottele, A.; Thurn-Albrecht, T. *Phys. Rev. Lett.* **2001**, *87*, 226101.

131.   Koutsos, V.; van der Vegte, E.W.; Pelletier, E.; Stamouli, A.; Hadziioannou, G. *Macromolecules* **1997**, *30*, 4719-4726.

132.   Narayanan, R.; El-Sayed, M.A. *J. Phys. Chem. B* **2005**, *109*, 12663-12676.

133.   Barnes, W.L.; Dereux, A.; Ebbesen, T.W. *Nature* **2003**, *424*, 824-830.

134.   Elghanian, R.; Storhoff, J.J.; Mucic, R.C.; Letsinger, R.L.; Mirkin, C.A. *Science* **1997**, *277*, 1078-1081.

135.   Cerruti, M.G.; Sauthier, M.; Leonard, D.; Liu, D.; Duscher, G.; Feldheim, D.L.; Franzen, S. *Anal. Chem.* **2006**, *78*, 3282-3288.

136.   Stoermer, R.L.; Cederquist, K.B.; McFarland, S.K.; Sha, M.Y.; Penn, S.G.; Keating,

C.D. *J. Am. Chem. Soc.* **2006**, *128*, 16892-16903.

137. Wilson, J.L.; Poddar, P.; Frey, N.A.; Srikanth, H.; Mohomed, K.; Harmon, J.P.; Kotha, S.; Wachsmuth, J. *J. Appl. Phys.* **2004**, *95*, 1439-1443.

138. Odenbach, S. *Colloids Surf. A* **2003**, *217*, 171-178.

139. Lee, D.K.; Kang, Y.S. *Colloids Surf. A* **2005**, *257-258*, 237-241.

140. Meldrum, F.C.; Kotov, N.A.; Fendler, J.H. *Langmuir* **1994**, *10*, 2035-2040.

141. Fried, T.; Shemer, G.; Markovich, G. *Adv. Mater.* **2001**, *13*, 1158-1161.

142. Sun, S.; Murray, C.B.; Weller, D.; Folks, L.; Moser, A. *Science* **2000**, *287*, 1989-1992.

143. Cheyne, R.B.; Moffitt, M.G. *Langmuir* **2005**, *21*, 10297-10300.

144. Cheyne, R.B.; Moffitt, M.G. *Macromolecules* **2007**, *40*, 2046-2057.

145. Sachsenhofer, R.; Binder, W.H. *Polym. Prep.* **2008**, *49*, 193-194.

146. Binder, W.H.; Sachsenhofer, R. *Macromol. Rapid Commun.* **2008**, *29*, 1097-1103.

147. Binder, W.H.; Weinstabl, H.; Sachsenhofer, R. J. Nanomater. 2008, vol. 2008, Article ID 383020, 10 pages, 2008. doi:10.1155/2008/383020.

148. Barentin, C; Muller, P.; Joanny, J.F. *Macromoluecules* **1998**, *31*, 2198-2211.

149. Brandrup, J.; Immerqut, E.H.; Grulke, E.A. *Polymer Handbook 4th Ed.* Wiley-Interscience, New York, **2003**.

150. Lee, D.K.; Kim, Y.H.; Kim, C.W.; Cha, H.G.; Kang, Y.S. *J. Phys. Chem. B* **2007**, *111*, 9288-9293.

151. Yashchenok, A.M.; Gorin, D.A.; Pankin, K.E.; Lomova, M.V.; Shtykov, S.N.; Klimov, B.N.; Kurochkina, G.I.; Grachev, M.K. *Semiconductors* **2007**, *41*, 684-688.

152. Strobl, G. *The Physics of Polymers*, Springer, Berlin, **2007**.

153. Liquori, A.M. *Acta Cryst.* **1955**, *8*, 345-347.

154. Tanaka, T.; Chatani, Y.; Tadokoro, H. *J. Polym. Sci. Polym. Phys. Ed.* **1974**, *12*, 515-531.

155. Lindén, M.; Rosenholm, J.B. *Langmuir* **1995**, *11*, 4499-4504.

156. Rontu, N.; Vaida, V. *J. Phys. Chem. C* **2007**, *111*, 9975-9980.

157. Cheyne, R.B.; Moffitt, M. G. *Langmuir* **2006**, *22*, 8387-8396.

158. Deschênes, L.; Bousmina, M.; Ritcey, A.M. *Langmuir* **2008**, *24*, 3699-3708.

159. Fradin, C.; Luzet, D.; Braslau, A.; Alba, M.; Muller, F.; Daillant, J.; Petit, J.M.; Rieutord, F. *Langmuir* **1998**, *14*, 7327-7330.

160. Amado, E.; Kerth, A.; Blume, A.; Kressler, J. *Langmuir* **2008**, *24*, 10041-10053.

161. Krishnamurthy, K.; McIntyre, D. *J. Polym. Sci. Part B: Polym. Lett.* **1972**, *10*, 647-652.

162. Santangelo, P.G.; Roland, C.M.; Puskas, J.E. *Macromolecules* **1999**, *32*, 1972-1977.

163. Han, J.; Gee, R.H.; Boyd, R.H. *Macromoleucles* **1994**, *27*, 7781-7784.

164. Lopes, S.I.C.; Gonalves da Silva, A.M.P.S.; Brogueira, P.; Piarra, S.; Martinho, J.M.G. *Langmuir* **2007**, *23*, 9310-9319.

165. Peetla, C.; Graf, K.; Kressler, J. *Colloid Polym. Sci.* **2006**, *285*, 27-37.

166. Joncheray, T.J.; Denoncourt, K.M.; Meier, M.A.R.; Schubert, U.S.; Duran, R.S. *Langmuir* **2007**, *23*, 2423-2429.

167. Vollhardt, D.; Retter, U.; Siegel, S. *Thin Solid Films* **1991**, *199*, 189-199.

168. Wang, L.F.; Kuo, J.F.; Chen, C.Y. *Mat. Chem. Phys.* **1995,** *40*, 197-201.

169. Lemstra, P.J.; Bastiaansen, C.W.M.; Meijer, H.E.H. *Angew. Makromol. Chem.* **1986**, *145/146*, 343-358.

170. Friberg, S.E.; Moaddel, T.; Chattopadhyay, A.K. *Liquid Crystals* **1994**, *16*, 453-459.

171. Shchipalov, Y.K. *Glass and Ceramics* **2000**, *57*, 374-377.

172. Stöber, W.; Fink, A.; Bohn, E. *J. Colloid Interface Sci.* **1968**, *26*, 62-69.

173. Klein, L.C. *Ann. Rev. Mater. Sci.* **1985**, *15*, 227-248.

174. van Blaaderen, A.; van Geest, J.; Vrij, A. *J. Colloid Interface Sci.* **1992**, *154*, 481-501.

175. Lu, Y.; Ganguli, R.; Drewien, C.A.; Anderson, M.T.; Brinker, C.J.; Gong, W.; Guo, Y.; Soyez, H.; Dunn, B.; Huang, M.H.; Zink, J.I. *Nature* **1997**, *389*, 364-368.

176. Yamaguchi, A.; Uejo, F.; Yoda, T.; Uchida, T.; Tanamura, Y.; Yamashita, T.; Teramae, N. *Nat. Mater.* **2004**, *3*, 337-341.

177. Yang, H.; Coombs, N.; Sokolov, I.; Ozin, G.A. *Nature* **1996**, *381*, 589-592.

178. Shi, Q.; Wang, J.; Wyrsta, M.D.; Stucky, G.D. *J. Am. Chem. Soc.* **2005**, 127, 10154-10155.

179. Smått, J.-H.; Schunk, S.; Lindén, M. *Chem. Mater.* **2003**, *15*, 2354-2361.

180. Kang, C.; Kim, E.; Baek, H.; Hwang, K.; Kwak, D.; Kang, Y.; Thomas, E.L. *J. Am. Chem. Soc.* **2009**, *131*, 7538-7539.

181. Wang, X.; Bozhilov, K.N.; Feng, P. *Chem. Mater.* **2006**, *18*, 6373-6381.

182. Matsui, K.; Sando, S.; Sera, T.; Aoyama, Y.; Sasaki, Y.; Komatsu, T.; Terashima, T.; Kikuchi, J. *J. Am. Chem. Soc.* **2006**, *128*, 3114-3115.

183. Hubert, D.H.W.; Jung, M.; German, A.L. *Adv. Mater.* **2000**, *12*, 1291-1293.

184. Binder, W. H.; Sachsenhofer, R.; *Macromol. Chem. Phys.* **2008**, *29*, 1097-1103.

185. Binder, W. H.; Sachsenhofer, R.; Farnik, D.; Blaas, D. *Phys. Chem. Chem. Phys.* **2007**, *9*, 6435-6441.

186. Lindén, M.; Rosenholm, J.B. *Langmuir* **2000**, *16*, 7331-7336.

187.   Ariga, K.; Okahata, Y. *J. Am. Chem. Soc.* **1989**, *111*, 5618.

188.   Hubert, D.H.W.; Jung, M.; Frederik, P.M.; Bomans, P.H.H.; Meuldijk, J.; German, A.L. *Adv. Mater.* **2000**, *12*, 1286-1290.

189.   McConlogue, C.W.; Vanderlick, T.K. *Langmuir* **1997**, *13*, 7158-7164.

190.   Roiter, Y.; Ornatska, M.; Rammohan, A.R.; Balakrishnan, J.; Heine, D.R.; Minko, S. *Langmuir* **2009**, *25*, 6287-6299.

191.   Pauly, T.R.; Liu, Y.; Pinnavaia, T.J.; Billinge, S.J.L.; Rieker, T.P. *J. Am. Chem. Soc.* **1999**, *121*, 8835-8842.

192.   Aroti, A.; Leontidis, E.; Maltseva, E.; Brezesinski, G. *J. Phys. Chem. B* **2004**, *108*, 15238-15245.

Appendix

1. **Chemical structures of surfactants**

a)   Tween 20

$$H-(O-CH_2-CH_2)_x-O \qquad O-(CH_2-CH_2-O)_w-H$$

$$H-(O-CH_2-CH_2)_y-O-CH$$

$$CH_3-(CH_2)_{10}-C-(O-CH_2-CH_2)_z-O-CH_2 \qquad w+x+y+z=20$$

$$O$$

b)   Tween 40

$$H-(O-CH_2-CH_2)_x-O \qquad O-(CH_2-CH_2-O)_w-H$$

$$H-(O-CH_2-CH_2)_y-O-CH$$

$$H_{31}C_{15}-C-(O-CH_2-CH_2)_z-O-CH_2 \qquad w+x+y+z=20$$

$$O$$

c)   Tween 60

$$H-(O-CH_2-CH_2)_x-O \qquad O-(CH_2-CH_2-O)_w-H$$

$$H-(O-CH_2-CH_2)_y-O-CH$$

$$H_{35}C_{17}-C-(O-CH_2-CH_2)_z-O-CH_2 \qquad w+x+y+z=20$$

$$O$$

d)   Tween 80

$$H-(O-CH_2-CH_2)_x-O \qquad O-(CH_2-CH_2-O)_w-H$$

$$H-(O-CH_2-CH_2)_y-O-CH$$

$$H_{33}C_{17}-C-(O-CH_2-CH_2)_z-O-CH_2 \qquad w+x+y+z=20$$

$$O$$

e)   Brij 35

$$C_{12}H_{25}-(O-CH_2-CH_2)_{23}-HO$$

f)   Pluronic

$$HO-(CH_2-CH_2-O)_a-(CH-CH_2-O)_b-(CH_2-CH_2-O)_a-H$$
$$\quad\quad\quad\quad\quad\quad\quad\quad\quad\quad\quad |$$
$$\quad\quad\quad\quad\quad\quad\quad\quad\quad CH_3$$

Resume

Personal Details

Surname, First name	Li, Hangsheng
Date and place of birth	Oct. 18th, 1981 in Shanghai, China
Nationality	Chinese

Education and employments

Oct. 2006 – Present	Ph.D. studying in institute of physical chemistry of polymer, Martin Luther University Halle-Wittenberg, Germany
2004 – 2006	Master of applied polymer science, Martin Luther University Halle-Wittenberg, Germany
2000 – 2004	Bachelor of applied physics, Shanghai Teachers University, China

Statement and Affirmation

I, Hangsheng Li, hereby declare that I have done this Ph. D thesis by myself. I also certify that to the best of my knowledge any help received in preparing this work, and all sources used, have been acknowledged in this thesis.

Hereby I affirm that I wrote the present thesis without any inadmissible help by a third party and without any other means than indicated. This thesis has not been presented to any examination board in this or a similar form, neither in Germany nor in any other country.

I have written this dissertation at Martin Luther University Halle-Wittenberg under the scientific supervision of Prof. Dr. Jörg Kressler.

There have been no prior attempts to obtain a Ph.D. at any university.

Li, Hangsheng